UNIVERSITY OF CALIFORNIA,
IRVINE

Acoustic Microstreaming for Blood Separation and Disease Diagnosis in Microfluidic Devices

DISSERTATION

submitted in partial satisfaction of the requirements
for the degree of

DOCTOR OF PHILOSOPHY

in Biomedical Engineering

by

Neha Garg

Dissertation Committee:
Dr. Abraham P. Lee, Chair
Dr. Jered B. Haun
Dr. Edward L. Nelson

2019

DEDICATION

To

my parents, sisters, husband and friends

for all their support and love

TABLE OF CONTENTS

LIST OF FIGURES

LIST OF TABLES

ACKNOWLEDGMENTS

I would like to thank and express the deepest appreciation to my advisor and committee chair, Prof. Abraham P. Lee, for giving me an opportunity to come to UCI (thousands of miles away from my home) and work in his lab. He always encouraged me and enabled me to think outside the box. Without his guidance and persistent help, this dissertation would not have been possible. I would like to thank Prof. Jered Haun and Prof. Edward L. Nelson, for being on my committee and for all insightful discussions.

Each one of my projects is the result of multiple collaborations and for that, I want to thank Center for Advanced Design and Manufacturing of Integrated Microfluidics (CADMIM) and Dr. Gisela Lin for introducing me and exposing me to incredible opportunities. I especially want to thank Dr. Ian Papautsky and Dr. Nivedita Nivedita for guiding me and shaping my PhD. Without that collaboration, the article "A High Throughput Microfluidic Platform for Size-Selective Enrichment of Cell Populations in Tissue and Blood Samples. *Analyst*, 2017, 142, 2558-2569" and subsequently the journal front cover would not have been possible. Following that, I want to extend my acknowledgements to Dr. Trisha M. Westerhof for mentoring me and driving my project. She was always there for me whenever I needed general insight or advise me during experiments. Along those lines, I want to thank Vick Liu and Dr. Robin Liu for asking me tough questions and collaborating with me. Without Dr. Westerhof, Dr. Liu, Dr. Nelson and Vick, my paper on "Whole-Blood Sorting, Enrichment and *in situ* Immunolabeling of Cellular Subsets Using Acoustic Microstreaming. *Microsystems & Nanoengineering*, 2018, 4, 17085" would not have been possible. Further, I would like to thank Dr. David Camerini, Dr. Arlo Randall, Dr. Xiaowu Liang, Andy, Jozelyn and whole Antigen Discovery Inc. for helping me develop a point-of-care technology for infectious diseases and achieve my goal of improving healthcare in resource limited settings. Without their support and guidance, my article and journal front cover on "Rapid Immunodiagnostics of Multiple Viral Infections in an Acoustic Microstreaming Device with Serum and Saliva Samples. *Lab on a Chip*, 2019, 19, 1524-1533" would not have been possible. Therefore, I acknowledge The Royal Society of Chemistry for providing permissions to incorporate the copyright material in my dissertation. Last but not least, I want to thank Dr. David Yang, Dr. Dirk Heckel and Erin Taylor at Beckman Coulter Inc. for pushing me to "think big" and helping me in sample analysis.

My sincerest gratitude to all the members of the BioMiNT Lab. I would like to thank Dr. Wei-Feng Feng (Willy) and Dr. Xiaolin Wang for training me in cleanroom. I would like to thank Dr. Derek Vallejo and Dr. G. K. Kurup for being such wonderful mentors. I especially want to thank Paul Yoo for working with me tirelessly on understanding and solving the physics of acoustic microstreaming. I want to thank Mohammad Aghaamoo for helping and working with me on extending the device's capability towards gene therapy. I want to thank Dr. David Lai (GlaxoSmithKline) and Dr. Stefano Begolo (Aline Inc.) for providing me the opportunity to experience industry culture and learn new techniques. I would also like to acknowledge Schlumberger Foundation Fellowship for providing me the financial support during my PhD.

Finally, I want to thank my sisters, my husband, Dr. Ankit Agrawal, my family and my friends (Vaibhav Pandey, Tanmay Ghonge, Bhoomika Mathur and everybody else) for continued support. I want to especially thank my sisters Dr. Priyanka Garg and Mrs. Meenakshi Garg for always helping me in making career related choices and motivating me to achieve the impossible. None of the achievements would have been possible without the constant support and struggle of my parents (Mr. Vishnu Dutt Garg and Mrs. Saroj Garg) and I cannot thank them enough for always being there with me.

CURRICULUM VITAE

Neha Garg

Education

2009-2014 Bachelor of Technology (B. Tech) & Master of Technology (M. Tech)
Biotechnology and Biochemical Engineering
Minor in Chemical Engineering
Indian Institute of Technology (IIT) Kharagpur, India

2014-2019 M. S. + Ph.D. in Biomedical Engineering
University of California, Irvine, CA, USA

Honors and Scholarship

2015-2019 Recipient of Schlumberger Foundation Fellowship; amounted to $50,000/year

Work Experience

May 2018 – September 2018 Summer Intern in Product and Process Engineering
GlaxoSmithKline, PA

June 2017 – September 2017 Summer Intern in Microfluidic Fabrication
Aline Inc., CA

Peer-Reviewed Journal Publications

N. Garg, D. Boyle, A. Randall, A. Teng, J. Pablo, X. Liang, D. Camerini, A. Lee, 'Rapid Point-of-Care Detection of Multiple Viral Infections using Acoustic Microstreaming', *Lab on Chip*, 19 (2019), 1524-1533 (Featured as journal front cover).

N. Garg, T. Westerhof, V. Liu, R. Liu, E. Nelson, A. Lee, 'Highly Efficient Trapping and Separation of Whole Blood Components Using Acoustic Microstreaming', *Microsystems and Nanoengineer*ing *(Nature Publishing Group),* 4 (2018), 17085

N. Nivedita*, **N. Garg***, I. Papautsky, A. Lee, 'Integrated Microfluidic Platform for Selective Isolation and Enrichment of Particles', *Analyst 142* (2017), 2558-2569 (Featured as journal front cover)

N. Garg*, D. Boyle*, D. Vallejo* and Abraham Lee. 'Integrated On-Chip Microfluidic Immunoassay for Rapid Biomarker Detection', *Procedia Engineering 159* (2016) 53 – 57

Peer-Reviewed Conference Publications

N. Garg, D. Boyle, T. Westerhof, E. Nelson, and A. Lee. 'Isolation and Enrichment of Rare Circulating Tumor Cells from Whole Blood', *Acoustofluidics*, San Diego, 2017

N. Garg, D. Boyle, D. Vallejo and A. Lee. 'Integrated On-Chip Microfluidic Immunoassay for Rapid Biomarker Detection', *Humanitarian Technology Conference*, Boston, 2016

N. Garg, T. Westerhof, E. Nelson, A. Lee. 'Size Sorting and *In Situ* Labeling of Whole Blood Using Acoustic Microstreaming, *Micro*TAS, Savannah, USA, 2017

N. Garg and A. Lee. 'Highly Efficient Trapping of Rare Cells from Whole Blood Using Acoustic Microstreaming', *MicroTAS*, Dublin, Ireland, 2016

N. Nivedita, **N. Garg**, P. Mukherjee, W. Fang, A. Lee and I. Papautsky. 'Integrated Microfluidic System for Rare Cell Separation and Enrichment', *MicroTAS*, Gyeongju, Korea, 2015

ABSTRACT OF THE DISSERTATION

Acoustic Microstreaming for Blood Separation and Disease Diagnosis in Microfluidic Devices

By

Neha Garg

Doctor of Philosophy in Biomedical Engineering

University of California, Irvine, 2019

Dr. Abraham P. Lee, Chair

Numerous applications in biology and medicine requires efficient and reliable separation of cellular or sub-cellular components from blood for disease diagnosis, genetic analysis, drug screening, and therapeutics. However, analyzing undiluted whole human blood is challenging due to its complex composition of hematopoietic cellular populations, plasma and sub-cellular components such as nucleic acids, metabolites, and proteins. In addition, current state-of-art for blood fractionation relies on multi-step density-based centrifugation or flow cytometry which are manual, time-consuming and unable to process whole blood. In this dissertation, we aim to demonstrate a multi-functional, low-cost microfluidic acoustic streaming platform to enrich and characterize cellular components from whole blood and utilize blood's sub-cellular components for simultaneous detection of multiple infections.

First, we present Lateral Cavity Acoustic Transducers (LCATs) that enables (1) the sorting of undiluted donor whole blood into its cellular subsets (platelets, RBCs, and WBCs), (2) the enrichment and retrieval of breast cancer cells (MCF-7) spiked in donor whole blood

at rare cell relevant concentrations (10/ml), and (3) on-chip immunofluorescent labeling for the detection of specific target cellular populations by their known marker expression patterns. Our approach thus demonstrates a compact system that integrates upstream sample processing with downstream separation/enrichment, to carry out multi-parametric cell analysis for blood-based diagnosis and liquid biopsy blood sampling.

Second, we integrated a passive (spiral inertial microfluidic device) and an active device (LCAT) for high-throughput separation, enrichment and release of specific target cellular population (such as larger side-population (SP) of DU-145 cells from tissue biopsy or larger monocytic cell population from blood sample). After optimization with particles spiked in blood, this platform removed >90% of the smaller cells, such as RBCs in a blood sample or smaller cancer cells in a heterogeneous cell line, and provided 44,000x enrichment from remaining sample within 5 minutes of device operation.

Third, since whole blood comprises not only cellular subsets, but also sub-cellular components, we utilized the antibodies in both blood serum and saliva for the multiplexed screening of HIV, HPV and HSV within 17.5 minutes. We integrated this acoustic microstreaming platform with a protein microarray and verified reactivity of patient antibodies with HIV, HPV and HSV antigens. This integrated microfluidic protein array platform is the basis of a potent strategy to delay progression of primary infection, reduce the risk of co-infections and prevent onward transmission of infections by point-of-care detection of multiple pathogens.

INTRODUCTION

Cancer

Cancer is one of the major causes of death worldwide and can be cured if diagnosed and treated early. It is a dynamic and gene-altering disease which causes oncogenes and tumor suppressor genes to undergo mutations.[1] During tumor formation, these oncogenes mimic normal growth signaling cascade and render cancer cells self-sufficient while, the tumor suppressor genes acquire resistance to programmed cell death, apoptosis, to thrive and divide indefinitely.[2] Cancer cells evade anti-growth signals and become immortal by acquiring limitless replicative potential.[2] After angiogenesis (formation of new blood vessels), they invade adjacent tissues and other distant sites to better access space and nutrients leading to metastasis.

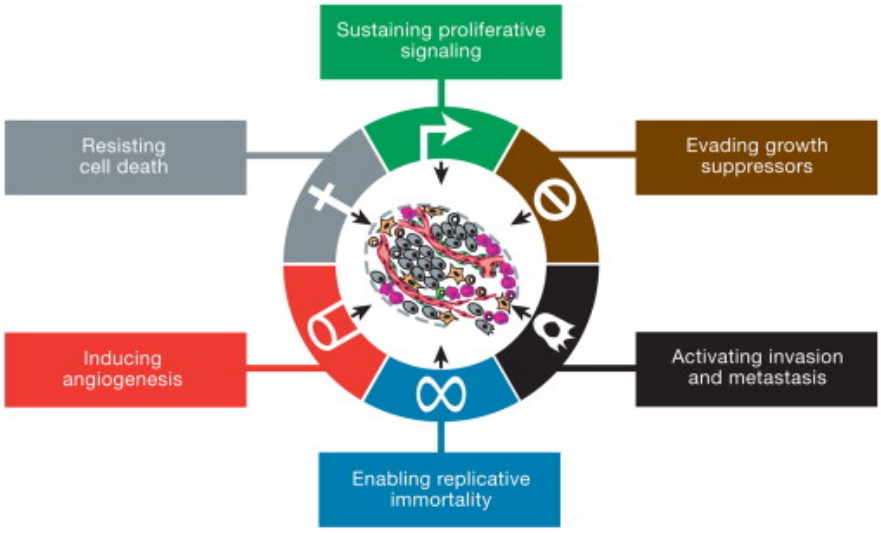

Figure 1: Schematic representation of the six hallmarks of cancer. Reprinted with permission from reference number 2. Copyright © 2011 Elsevier.

Current cancer treatments include the invasive tissue biopsy and minimally invasive biopsies.[3] Other cancer treatments include radiation therapy to kill cancer cells and shrink tumors,[4] chemotherapy to kill the cancer cells using drugs,[5] immunotherapy to help immune system fight cancer,[6] hormone therapy to slow or prevent the recurrence,[7] and stem cell transplant to restore blood forming stem cells especially for leukemia and lymphoma. Non-invasive techniques are becoming more prevalent over invasive and minimally invasive techniques due to the side-effects, chances of recurrence, patient discomfort, cost-effectiveness and for the purpose of continuously identifying and monitoring cancer.

Cancer cells bear biomarkers that can be used to determine disease progression and patient prognosis. Detection of biomarkers like circulating tumor cells (CTCs), nucleic acids and exosomes in peripheral blood has been gaining popularity as an alternative to invasive biopsies. "Liquid biopsy" is a non-invasive way to test patient's blood for identifying CTCs and cell free circulating tumor deoxyribonucleic acid (ctDNA) released by primary tumor and metastatic sites, and has potential for early cancer prognosis. Apart from providing accurate information about cancer progression and intensity real-time, they are effective in gauging the body's response to the chosen treatment method and allow for situation specific responses.[8] Utilization of CTCs as a marker in liquid biopsy is especially useful when there is not enough tissue or it is hard to reach, but it presents some inherent challenges. First, CTCs occur at very low numbers (1-10cells/mL of blood) in the presence of billions of hematopoietic cells which makes their isolation extremely difficult.[9] Second, CTC genesis involves a morphogenetic process termed as epithelial to mesenchymal transition (EMT) which enables a polarized epithelial cell to go through biochemical changes and become mesenchymal, leading to improved migratory capacity, invasiveness and highly elevated

extracellular matrix (ECM) component production.[10] Basement membrane then destructs and causes the mesenchymal CTC to escape the epithelial layer it was formed.[11] Therefore, owing to rarity of CTCs and heterogeneity with respect to biomarker expression, any CTC detection system should be sensitive enough to detect complete population of these small numbers of cells. Hence, for isolation of CTCs as means of their use as prognostic biomarkers and achieve accurate cancer cell detection rapidly, there is an urgent need of sorting devices which can combine high throughput with high selectivity and high isolation efficiency.

HIV-HPV-HSV

The human immunodeficiency virus (HIV), human papilloma virus (HPV) and herpes simplex virus (HSV) can all be transmitted sexually as well as vertically.[12–14] HPV and HSV can also be transmitted by more casual contact.[13,14] HIV infects vital cells in the human immune system including CD4+ helper T-cells, dendritic cells and macrophages. HIV infection causes a decline in number of CD4+ T-cells, leading to the loss of humoral and cell-mediated immunity and development of the acquired immunodeficiency syndrome (AIDS).[15] Infection by HPV is limited to the basal cells (deepest layer of epidermis) of stratified epithelium through micro-abrasions which can result in warts or mucosal flat lesions.[16] Some types of HPV, including HPV-16 and 18, may also induce pre-cancerous lesions, and constitute the primary risk factor for cervical cancer in females and head and neck cancer in males.[17] Herpes simplex virus types one and two (HSV-1, HSV-2) can be transmitted sexually or by direct contact with the body fluid or lesions of an infected individual.[18] HSV infects epithelial cells in mucosal tissue which can result in cold sores or blisters. It is further transported along sensory nerves to the nerve cell bodies, where HSV can reside lifelong. Both HSV-1 and HSV-2, in immunocompromised people such as those with HIV, can have

severe symptoms and more frequent outbreaks.[19] In addition, genital lesions caused by HSV-2 increase the risk of acquiring a new HIV infection by approximately three-fold.[20] With such a high prevalence and co-infection capability of these viral infections, early, rapid and low-cost diagnosis is desirable.

Microfluidics

Microfluidics is the science and technology of systems that process or manipulate small (10^{-9} to 10^{-18} liters) amounts of fluid, using channels with tens to hundreds of micrometer dimensions.[21] It is a multi-disciplinary field that has led to the revolution in rapid sensing and detection of chemical and biological samples. The use of low sample volumes, shorter assay time due to high surface-to-volume ratio, capability to multiplex and significantly low-cost rendered microfluidics in various applications such as biomedical diagnostics, drug screening or emulsification.[22] Recently, there is a great interest in determining populations of specific cell types such as circulating tumor cells for cancer diagnosis or deformability of red blood cells to determine the presence of sickle cell anemia. In addition, target proteins and other biomolecules such as antibodies, circulating tumor DNA or exosomes are also of great interest to determine the presence of any infectious agents or for cancer prognosis.

Acoustic Microstreaming

Acoustic streaming is a phenomenon of steady flow generation or circulation near an orifice traversed by sound or due to vibrating elements such as solid cylinders or spheres, and gas bubbles.[23] It was the first time when Rayleigh *et al.* analyzed the acoustic streaming at a large scale induced by sound waves propagating between parallel plates or a Kundt's

tube and is often called as Rayleigh streaming.[24] A special type of acoustic microstreaming based on gas and liquid was studied for the first time by Nyborg *et al.* in 1956.[25] He observed in the first arrangement that sonic irradiation caused little motion of the liquid after the air was excluded from the cell. However, when the small pockets of air bubbles were introduced, ordered vortical motions were observed nearby after lowering the sound pressure and slowing down the motion. It was then he introduced bubble associated acoustic streaming to have associated with mixing of cell contents, viscous stresses on boundaries and impacts on small objects trapped temporarily in the flow. Further, in one of the arrangements, he described the use of a tapered cone to build up the pressure amplitude and observed an energetic streaming motion when a bubble is placed or formed near the source. In this arrangement, he utilized the radius of a resonant bubble at a frequency *f* (cps) as

$$2\pi af = \sqrt{(\frac{3\gamma P}{\rho})}$$

Where, a is the bubble radius, γ is the ratio of specific heats for the gas, *P* is the hydrostatic pressure and ρ is the density of the fluid and concluded that the most rapid motion will occur if bubble radius and resonant frequency are correlated by the above equation. In the final arrangement, he achieved higher amplitude sound fields and encountered interesting phenomenon on mechanics of bubble growth when a liquid contains dissolved gas but no visible bubbles. After the sonic actuation, he observed tiny bubbles appearing and growing on the upper surface of the liquid film near the vibrating source. He attributed the bubble motion to the Bjerkness forces and obtained a steady value $<F_x>$ as:

$$< F_x >= -\frac{b}{4}\frac{\partial(p^2)}{\partial x}\cos\alpha$$

Where, p_x is the pressure amplitude assuming the variation only in one direction (x). Hence, for bubbles well below resonant sizes, cosα = -1 and the steady force is directed towards increasing pressure amplitude. He observed that small bubbles reach the center of the tip, where the pressure amplitude is maximum. As they grow to resonant size, they will radiate a higher amplitude scattered field of their own which will attract small bubbles towards itself. After becoming larger than resonant size, the bubble is repelled and rests where the pressure amplitude is minimum (cosα = 1). He studied acoustic streaming motions induced by the vibrating tips with this arrangement to achieve circulatory motion of small particles as shown in Fig. 2 He observed greatest speeds at points near the tip which decrease with distance. He finally concluded that near the rigid surface of the acoustic source, an acoustic boundary layer exists, where the particle velocities rise quickly from zero to free-field values given by standard non-viscous standard acoustics theory and that the streaming from vibrating bubbles at resonance is attributed to viscous stresses.[25]

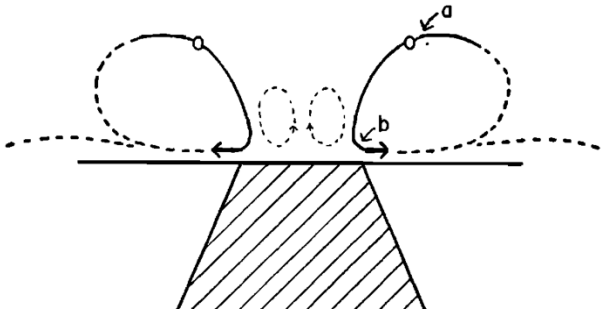

Figure 2: Acoustic streaming pattern near the vibrating tip with maximum velocity and acceleration just outside the periphery of the tip. Reprinted with permission from reference number 25. Copyright © 1956 AIP Publishing.

After 1956, Elder *et al.* continued the work of Kolb and Nyborg *et al.* and made significant contribution for bubbles or cavities undergoing volume resonance, also called as cavitation microstreaming in 1958.[26] He utilized a dilute suspension of aluminum dust and

made his experimental observation of acoustic streaming as a function of driver amplitude near a vibrating air bubble (just smaller than the resonant size) situated at the bottom of a vessel filled with viscous liquid. He found that the damping ratio (pressure amplitude of the incident wave, P_0/pressure amplitude of the scattered wave, P_s) for small viscosities is less than the damping constant of a free bubble of same volume, compressed by the same amount due to a bubble located on a rigid boundary being a better scatterer. He further attributed this excess damping to viscous drag in the acoustic boundary layer, where the tangential component of the acoustic particle velocity drops to zero.

He observed streaming fields near excited bubbles and generalized four modes of streaming as a response to different amplitude and viscosity of the fluid as shown in Fig.3. The first regime is observed with the addition of a detergent in a solution of low viscosity and associated with the presence of an acoustic boundary layer on the bubble surface. The second regime was specifically important and was apparent for wide range of amplitudes and viscosities. He plotted the vorticity for various positions (x and y) and attributed the crossover from clockwise vortex to counter-clockwise for positive x at $y=2.3\delta_{ac}$ to the presence of the phase in the first order streaming velocity solution. Third regime was specifically for liquids of low viscosities at sufficiently large amplitudes and was not observed at higher viscosities. The mechanism for this regime was not described but was attributed to the mobility of free cavitation bubbles. Fourth regime occurred only in least viscous solutions at very high amplitudes seemed similar to second with the absence of lower vortex ring owing to the proximity of turbulent bubble surface hindering the steady state condition and rapid speed of the tracer particles becoming difficult to follow. Finally, he concluded that the occurrence of different types of streaming was associated with the

presence of first order effects and it is necessary to specify the surface condition of the bubble in order to accurately predict the streaming type.[26]

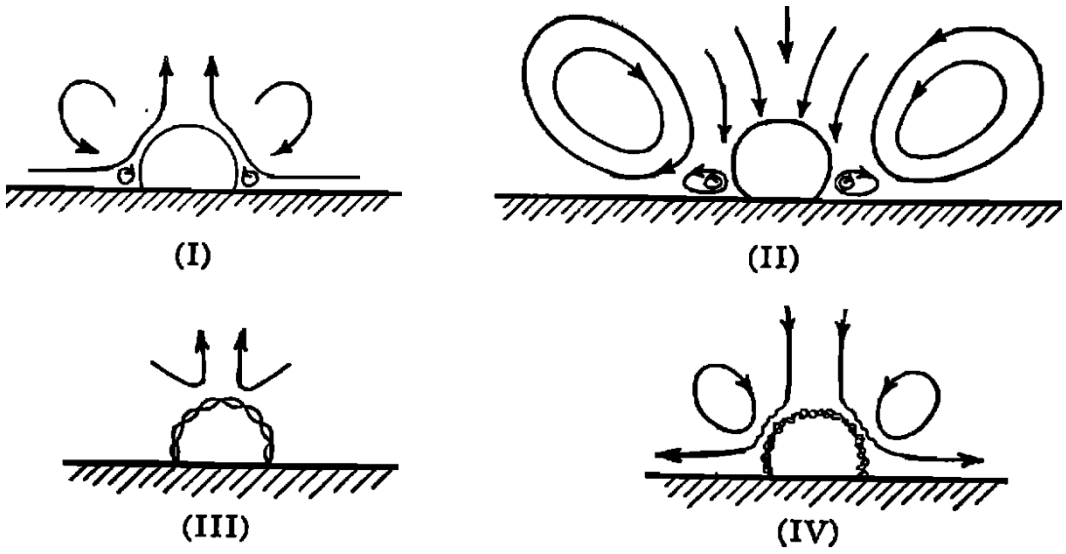

Figure 3: Four regimes of streaming. Reprinted with permission from reference number 26. Copyright © 1958 AIP Publishing.

It was in early 60's that theoretical developments took place in the field of oscillatory unsteady boundary layers formed on solid bodies such as spheres or cylinders present in fluctuating external flow of small amplitude by Stuart *el al*.[27] Although the liquid-solid microstreaming phenomenon are not utilized here, we understood its importance in clarifying the cavitation microstreaming boundary layer fundamentals. The general laminar boundary layer governing equation for a curved surface (surface curvature is neglected, or curvature is large) is given by:

$$\frac{\partial u}{\partial t} + u\frac{\partial u}{\partial x} - w\frac{\partial u}{\partial z} = \frac{\partial U}{\partial t} + U\frac{\partial U}{\partial x} + \nu\frac{\partial^2 u}{\partial x^2} \tag{1}$$

$$\frac{\partial^2 \psi}{\partial z\,\partial t} + \frac{\partial \psi}{\partial z}\frac{\partial^2 \psi}{\partial x\,\partial z} - \frac{\partial \psi}{\partial x}\frac{\partial^2 \psi}{\partial z^2} = \frac{\partial U}{\partial t} + U\frac{\partial U}{\partial x} + \nu\frac{\partial^3 \psi}{\partial z^3} \tag{2}$$

Where, $u = \frac{\partial \psi}{\partial z}$, $w = -\frac{\partial \psi}{\partial x}$ are the corresponding velocity components. *U (x, t)* is the external-flow velocity (outside the boundary layer) defined as:

$$U(x,t) = \frac{1}{2} U_0 (x) (e^{i\omega t} + e^{-i\omega t}) \quad (3)$$

U_0 is the steady potential fluid flow at the solid surface and the oscillatory boundary layer thickness as mentioned previously is $\delta = (\nu/\omega)^{1/2}$. Dimensionless variables V, ξ, η and τ were introduced to simplify the equation where,

$$U(x,t) = U_\infty V(\xi,t), z = \eta (2\nu/\omega)^{1/2}, \psi = (2\nu/\omega)^{1/2} U_\infty \chi(\xi,\eta,t),$$

$$x = \xi d, t = \tau/\omega, U_0(x) = U_\infty V_0(\xi), \alpha = U_\infty/\omega d$$

With U_∞ as the characteristic speed of the solid surface and *d* as the characteristic length, the generalized equation then becomes:

$$\omega U_\infty \frac{\partial^2 \chi}{\partial \eta \partial \tau} + \frac{{U_\infty}^2}{d} \frac{\partial \chi}{\partial \eta} \frac{\partial^2 \chi}{\partial \eta \partial \xi} - \frac{{U_\infty}^2}{d} \frac{\partial \chi}{\partial \xi} \frac{\partial^2 \chi}{\partial \eta^2} = \omega U_\infty \frac{\partial V}{\partial \tau} + \frac{{U_\infty}^2 V}{d} \frac{\partial V}{\partial \xi} + \frac{\omega}{2} U_\infty \frac{\partial^3 \chi}{\partial \eta^3} \quad (4)$$

$$\frac{\partial^2 \chi}{\partial \eta \partial \tau} - \frac{1}{2} \frac{\partial^3 \chi}{\partial \eta^3} - \frac{\partial V}{\partial \tau} = \alpha \left(- \frac{\partial \chi}{\partial \eta} \frac{\partial^2 \chi}{\partial \eta \partial \xi} + \frac{\partial \chi}{\partial \xi} \frac{\partial^2 \chi}{\partial \eta^2} + V \frac{\partial V}{\partial \xi}\right) \quad (5)$$

The above boundary layer equation is valid for small α, where RHS can be neglected and a solution of χ can be developed in the form of power series expansion as shown below:

$$\chi = \frac{1}{2} V_0(\xi)\left[\chi_0(\eta) e^{i\tau} + \widetilde{\chi_0}(\eta) e^{-i\tau}\right] + \alpha \left[\chi_s(\xi,\eta) + \frac{1}{2}\left(\chi_2 e^{2i\tau} + \widetilde{\chi_2} e^{-2i\tau}\right)\right] + O(\alpha^2) \quad (6)$$

Where, χ_0 is the first order oscillatory stream function, χ_s is the steady second order stream function and χ_2 is the second order unsteady oscillatory stream function inside the boundary layer. Solving for χ_0 by substituting the solution independent of α in LHS of above equation, with the following initial and boundary conditions:

$$\chi_0(\eta) = \frac{\partial \chi_0}{\partial \eta} = 0, at\ \eta = 0$$

$$\frac{\partial\,\chi_0}{\partial\eta} \to 1, as\ \eta \to \infty$$

$$\frac{i}{2}\,V_0\left[\frac{\partial\chi_0}{\partial\eta}\,e^{i\tau} - \frac{\partial\widetilde{\chi_0}}{\partial\eta}\,e^{-i\tau}\right] - \frac{V_0}{4}\left[\frac{\partial^3\chi_0}{\partial\eta^3}\,e^{i\tau} + \frac{\partial^3\widetilde{\chi_0}}{\partial\eta^3}\,e^{-i\tau}\right] - \frac{iV_0}{2}\left[e^{i\tau} - e^{-i\tau}\right] = 0 \qquad (7)$$

Bringing the coefficients of $e^{i\tau}$ and $e^{-i\tau}$ together and equating the individual terms to zero:

$$\frac{\partial^3\chi_0}{\partial\eta^3} - 2i\frac{\partial\chi_0}{\partial\eta} + 2i = 0 \qquad (8)$$

Hence, $\chi_0 = \eta + \frac{C_1}{2}\,(1-i)e^{(1+i)\eta} - c_2\frac{(1-i)}{2}\,e^{-(1+i)\eta} + c_3$ (9)

Inserting the boundary conditions to solve constants c_1, c_2, and c_3, we get

$$\chi_0 = \eta - \frac{1}{2}\,(1-i)[1 - e^{-(1+i)\eta}] \qquad (10)$$

Substituting the higher order terms of α from equation 6 to equation 5, we get:

$$-\frac{\alpha}{2}\,\frac{\partial^3\chi_s}{\partial\eta^3} = \frac{\alpha}{4}\,V_0\frac{\partial V_0}{\partial\xi}\left[\frac{\partial\chi_0}{\partial\eta}\,e^{i\tau} + \frac{\partial\widetilde{\chi_0}}{\partial\eta}\,e^{-i\tau}\right]^2 + \frac{\alpha}{4}\,V_0\frac{\partial V_0}{\partial\xi}\left[\chi_0 e^{i\tau} + \widetilde{\chi_0}e^{-i\tau}\right]\left[\frac{\partial^2\chi_0}{\partial\eta^2}\,e^{i\tau} + \frac{\partial^2\widetilde{\chi_0}}{\partial\eta^2}\,e^{-i\tau}\right] +$$

$$\frac{\alpha}{4}\,V_0\frac{\partial V_0}{\partial\xi}[e^{i\tau} + e^{-i\tau}\,]^2 \qquad (12)$$

Since there is no time dependence on LHS, we get:

$$\frac{\partial^3\chi_s}{\partial\eta^3} = V_0\frac{\partial V_0}{\partial\xi}\left[\frac{\partial\chi_0}{\partial\eta}\,\frac{\partial\widetilde{\chi_0}}{\partial\eta} - \frac{1}{2}\,\chi_0\frac{\partial^2\chi_0}{\partial\eta^2} - \frac{1}{2}\,\widetilde{\chi_0}\,\frac{\partial^2\widetilde{\chi_0}}{\partial\eta^2} - 1\right] \qquad (13)$$

Due to the third order differential equation, the solution should be of the form: $\chi_s = A + B\eta + C\eta^2$. The boundary condition for obtaining χ_s are as follows:

$$\chi_s\,(\eta) = \frac{\partial\chi_s}{\partial\eta} = 0, at\ \eta = 0$$

$$\frac{\partial\,\chi_s}{\partial\eta} \to finite, as\ \eta \to \infty$$

With χ_0 available as a function of η, and $\widetilde{\chi_0}$ as a complex conjugate, we get,

$$\frac{\partial^3\chi_s}{\partial\eta^3} + V_0\frac{\partial V_0}{\partial\xi}\left[\frac{1}{2}e^{-(1+i)\eta}\{(1+i)\eta - i + 2\} + \frac{1}{2}e^{-(1-i)\eta}\{(1-i)\eta + i + 2\} - e^{-2\eta}\right] = 0 \qquad (14)$$

$$\frac{\partial^3 \chi_s}{\partial \eta^3} = V_0 \frac{\partial V_0}{\partial \xi} \left[e^{-2\eta} - e^{-\eta}(\eta + 2)\cos\eta - e^{-\eta}\sin\eta \ (\eta - 1)\right] \quad (15)$$

Where, $e^{-(1+i)\eta} = e^{-\eta}(\cos\eta - i\sin\eta)$ and $e^{-(1-i)\eta} = e^{-\eta}(\cos\eta + i\sin\eta)$. Integrating three times yields:

$$\chi_s = V_0 \frac{\partial V_0}{\partial \xi} \left[-\frac{1}{8}e^{-2\eta} - e^{-\eta}(\cos\eta + \sin\eta) + \frac{1}{4}e^{-\eta}(-\cos\eta + \sin\eta) - \frac{1}{4}e^{-\eta}(\cos\eta + \sin\eta + 2\eta\sin\eta) + c_1\eta^2 + c_2\eta + c_3\right] \quad (16)$$

The boundary condition generates, c_1, c_2, and c_3 as 0, -3/4 and 13/8, finally giving:

$$\chi_s = V_0 \frac{\partial V_0}{\partial \xi} \left[\frac{13}{8} - \frac{3}{4}\eta - \frac{1}{8}e^{-2\eta} - \frac{3}{2}e^{-\eta}\cos\eta - e^{-\eta}(\sin\eta) - \frac{1}{2}e^{-\eta}(\eta\sin\eta)\right] \quad (17)$$

Now, the steady velocity u_s is defined as: $u_s = \alpha \frac{\partial \psi_s}{\partial \eta}\frac{\partial \eta}{\partial z}$, where:

$$\frac{\partial \psi_s}{\partial \eta} = U_\infty \sqrt{\frac{2\nu}{\omega}} \frac{\partial \chi_s}{\partial \eta} \quad (18)$$

$$u_s = \alpha U_\infty \sqrt{\frac{2\nu}{\omega}} V_0 \frac{\partial V_0}{\partial \xi}\left(-\frac{3}{4}\right) = \left(-\frac{3}{4\omega}\right) U_0 U'_0 \quad (19)$$

This steady flow velocity, u_s is non-zero at the edge of the boundary layer. Stuart *et al.* argued the importance of Reynolds number, $R_s = \frac{{U_\infty}^2}{\omega\nu}$ in determining the decay of u_s with distance from the wall. For small R_s, he mentioned that the flow outside the thin boundary layer is governed by linearized Navier-Stokes equation of slow motion. Stuart *et al*[27]*.* and Riley *et al.*[28] both determined the presence of outer boundary layer, especially at large R_s and is driven by the above velocity equation.

Following the streaming patterns near a spherical drop or a bubble, Riley *et al.*[29] in 1992 considered steady streaming about a circular cylinder when plane sound waves are incident upon it from orthogonal directions to determine the steady streaming velocity

which drives the outside Stokes boundary layer. With ψ as the stream function, the flow around the cylinder is given by the Navier-Stokes Equation in two-dimensions:

$$\frac{\partial(\nabla^2\psi)}{\partial t} - \frac{\varepsilon}{r}\frac{\partial(\psi,\nabla^2\psi)}{\partial(r,\theta)} = \frac{\varepsilon^2}{R_s}\nabla^4\psi, \tag{20}$$

Where, the velocity components are defined as, $v_r = \frac{1}{r}\frac{\partial\psi}{\partial\theta}$ and $v_\theta = -\frac{\partial\psi}{\partial r}$. R_s is the Reynolds' number defined as $R_s = \frac{\varepsilon U_0 a}{\nu}$ and characteristic amplitude $a\varepsilon = \frac{U_0}{\omega}$. Riley developed the solution for flow variables assuming ε <<1 and for that, the stream function can be expanded in powers of ε as:

$\psi(r,\theta) = \psi_0(r,\theta,t) + \varepsilon\{\psi_1^s(r,\theta) + \psi_1^u(r,\theta,t)\} + O(\varepsilon^2)$, where

To conform with the earlier work, Riley chose $x = \frac{\pi}{2} - \theta, y = r - 1$ and he obtained

$\tilde{\psi} = \sqrt{\frac{R_s}{2}}\frac{\psi}{\varepsilon}, \eta = \sqrt{\frac{R_s}{2}}\frac{y}{\varepsilon}$.

Substituting above in equation 20, he obtained

$\widetilde{\psi_0} = U(x)[\eta - \frac{1}{2}(1-i)\{1 - e^{-(1+i)\eta}\}]e^{it}$, similar to equation 10 by Stuart in 1965, where

$U(x) = -2i\{(\lambda - 1)\sin x + ie^{-ix}\}$ obtained by no-slip condition at $\eta = 0$. (21)

Now considering the terms of *O(ε)* in equation 29 and taking the time average $<\cdot>$, he obtained $< \widetilde{\psi_1^{(u)}} > = 0$, and

$$-\frac{1}{2}\frac{\partial^4\widetilde{\psi_1^{(s)}}}{\partial\eta^4} = < \frac{\partial(\widetilde{\psi_0},\partial^2\widetilde{\psi_0}/\partial\eta^2)}{\partial(x,\eta)} > \tag{22}$$

$$\frac{\partial\widetilde{\psi_0}}{\partial\eta} = U(x)[1 - e^{-(1+i)\eta}]e^{it} \tag{23}$$

$$\frac{\partial^2\widetilde{\psi_0}}{\partial\eta^2} = U(x)[(1+i)\left(e^{-(1+i)\eta}\right)]e^{it} \tag{24}$$

$$< \frac{\partial(\widetilde{\psi_0},\partial^2\widetilde{\psi_0}/\partial\eta^2)}{\partial(x,\eta)} > = \frac{\partial\widetilde{\psi_0}}{\partial x}\frac{\partial^3\widetilde{\psi_0}}{\partial\eta^3} - \frac{\partial\widetilde{\psi_0}}{\partial\eta}\frac{\partial^3\widetilde{\psi_0}}{\partial x\partial\eta^2} \tag{25}$$

Applying the identity, $< Re\left(Pe^{it}\right).Re\left(Qe^{it}\right) >= \frac{1}{2}Re(P^{*}Q)$, where P* denotes the complex conjugate of P and integrating three times after substituting the differentials, the authors obtained with c_is and d_is as constants,

$$\frac{1}{2}\frac{\partial\widetilde{\psi_1^{(s)}}}{\partial\eta} = Re[\left[\frac{d(UU^{*})}{dx}\left\{-\frac{1}{2}ie^{-(1-i)\eta} + \frac{(1-i)}{8}e^{-2\eta} + c_1\eta^2 + c_2\eta + c_3\right\}\right] - \left[U^{*}\frac{dU}{dx}\left\{\left(\frac{(1+i)}{2}\eta + i - \frac{1}{2}\right)e^{-(1-i)\eta} - \frac{1}{4}ie^{-2\eta} + \frac{d_1}{2}\eta^2 + d_2\eta + d_3\right\}\right]] \quad (26)$$

Applying the boundary conditions as follows:

$$\frac{\partial\widetilde{\psi_1^{(s)}}}{\partial\eta} = 0\ at\ \eta = 0\ gives\ c_3 = \frac{5i-1}{8}\ and\ d_3 = \frac{2-3i}{4} \quad (27)$$

$$\frac{\partial\widetilde{\psi_1^{(s)}}}{\partial\eta} = bounded\ as\ \eta \to \infty\ gives\ c_1 = c_2 = d_1 = d_2 = 0. \text{ Therefore,} \quad (28)$$

$$\frac{\partial\widetilde{\psi_1^{(s)}}}{\partial\eta} = \frac{d(UU^{*})}{dx}\left[\frac{1}{2}e^{-2\eta}\sin\eta + \frac{1}{8}e^{-2\eta} - \frac{1}{8}\right] - Re[U^{*}\frac{dU}{dx}\left\{\left(\frac{1+i}{2}\eta + i - \frac{1}{2}\right)e^{-(1-i)\eta} - \frac{1}{4}ie^{-2\eta} + \frac{2-3i}{4}\right\}] \quad (29)$$

With *U(x)* as in above expression (equation 21), Riley obtained

$$\frac{dU}{dx} = -2i(\lambda - 1)\cos x - 2ie^{-ix} \quad (30)$$

$$\frac{dU^{*}}{dx} = 2i(\lambda - 1)\cos x + 2ie^{ix} \quad (31)$$

$$U^{*}\frac{dU}{dx} = 2(\lambda - 1)\sin 2x + 2(\lambda - 1)\sin 2x - 4i\lambda \quad (32)$$

$$U\frac{dU^{*}}{dx} = 2(\lambda - 1)^2\sin 2x + 4(\lambda - 1)\sin 2x + 4i\lambda \quad (33)$$

$$U_s\ as\ \eta \to \infty\ then\ becomes\ [\frac{d(UU^{*})}{dx}\left(-\frac{1}{8}\right) - Re[U^{*}\frac{dU}{dx}\left(\frac{2-3i}{4}\right)] \quad (34)$$

$$U_s = \frac{3}{2}(1 - \lambda^2)\sin 2x + 3\lambda \quad (35)$$

Marmottant and Hilgenfeldt *et al.*[30], in 2003, together explained the mechanism of sonoporation in giant unilamellar lipid vesicles (GUVs) by violently collapsing bubbles in

microfluidic devices both theoretically and experimentally. He observed the vesicles being alternately attracted (in loop-like trajectories) and repelled (radially upwards and downwards) vigorously around the bubble. They concluded second-order effect of the nonlinearity in the Navier-Stokes equation due to four-fold increase of vesicle speed at double driving amplitudes. Qualitatively, at low viscosities (ν=1x10^{-6} m^2/s for pure water), the recirculation patterns they obtained were different than obtained by Elder *et al.*[26] in 1958 in millimeter sized bubbles. Theoretically, they concluded that micrometer scales of the experiments lead to a different regime of streaming motion in contrast to 'Stuart Streaming' as explained by Lighthill *et al.,* 1978.[31] They obtained small Reynolds number defined in Riley *et al.*[32] 1971 as ~0.04, and considered secondary streaming as Rayleigh-Nyborg-Westervelt (RNW) streaming.[30]

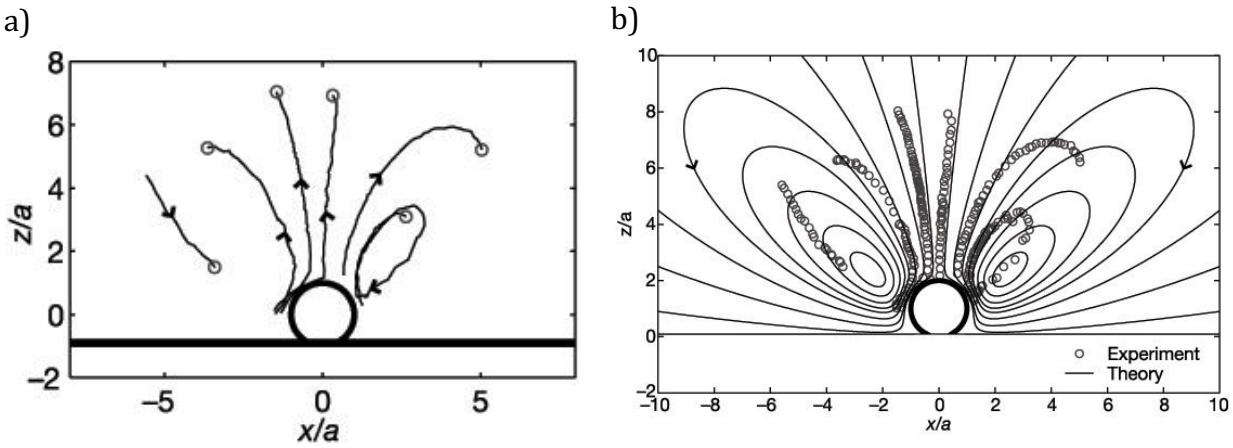

Figure 4: Streamlines due to acoustic microstreaming a) Trajectories of the lipid vesicles in a side view obtained experimentally b) Superimposition of the measured lipid vesicle trajectories along with streamlines of the flow achieved computationally. Reprinted with permission from reference number 30. Copyright © 2003 Springer Nature.

Following the studies of streaming patterns by encapsulated microbubbles in microfluidic devices, Wiklund *et al.* defined cavitation microstreaming as the flow formed by the viscous dissipation of acoustic energy in the boundary layer of a stably oscillating microbubble.[33] Therefore, after analyzing the mechanism with free bubbles in liquid, it was in 2011 and 2012 when microstreaming associated with sessile bubbles were studied experimentally in microfluidic devices.[34,35] Initially, the authors experimentally visualized the bubble induced microstreaming without any external flow and observed size selective trapping when a mixture of 2.5μm and 5μm sized particles were introduced in the microfluidic channel. As the particles enter the microchannel, due to denser streamlines near the bubble, the particles crossover to another streamline and settle in stable trajectory after the application of streaming flow. Larger particles are pushed in a smaller loop while smaller particles orbit in larger loops.

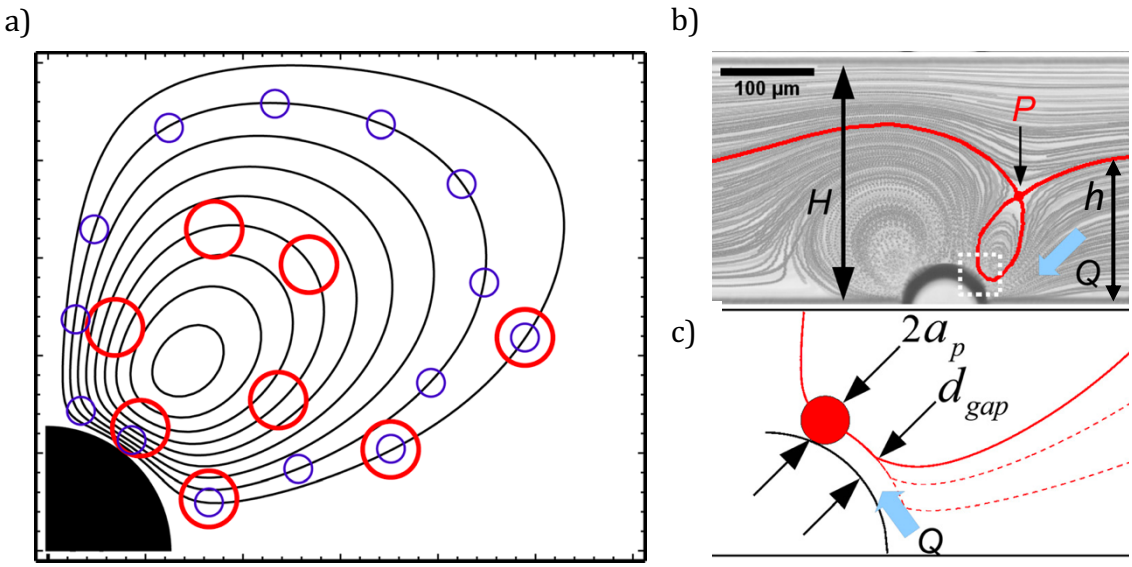

Figure 5: Particle separation phenomenon a) Schematic illustration of the circular streamlines for large and small particles. b) Flow field of the combined bubble induced

streaming and main-channel Poiseuille Flow. c) Schematic of the boxed region of (b).

However, owing to practical applications necessitating the importance of high throughput, they superimposed Poiseuille flow with bubble induced microstreaming. Here, at constant u_p, as the streaming velocity is increasing at large input voltages, u_s starts to dominate near the bubble and causes two vortex loop structures. Hence, the Poiseuille flow is partitioned in two regions by the critical streamline at the hyperbolic point P, and the fluid below the critical streamline has to pass through the gap between the upstream closed loop and the bubble surface. To understand the mechanism of trapping of 5μm sized particles and releasing of 2.5μm sized particles with superimposed Poiseuille flow, they applied the continuity equation and evaluated a parameter d_{gap} (predicted critical particle radius for trapping). With u_p and u_s as the mean Poiseuille velocity and streaming velocity, respectively, they obtained the following expression:

$$d_{gap} = \frac{u_p}{u_s}\, h\, [3\left(\frac{h}{H}\right) - 2(\frac{h}{H})^2] \tag{36}$$

Since the particles cannot penetrate the bubble, particles with radius $a_p > d_{gap}$ will be pushed into the vortex causing them to be trapped.

Following the analytical expression and empirical observations for particle trapping and separation, Rallabandi *et al*. derived the steady streaming solution for a sessile bubble in a microfluidic device. Similar to equation 20 in Riley *et al*., he developed an asymptotic solution in powers of ε as:

$$\psi = \psi_0 + \varepsilon\psi_1 + O(\varepsilon^2) \tag{37}$$

Where, ψ_0 is the leading order stream function for first order oscillatory flow and $\psi_1$is the second order streaming flow which consists of both steady and unsteady components. For

this, the authors only considered the steady component which constitutes the Eulerian mean flow and governed by the inhomogeneous Stokes equation similar to equation 22 in cylindrical coordinates. In general, since the steady motion of individual fluid elements are more relevant, they evaluated the Eulerian stream function with a Stokes drift term ψ_d as:

$$\psi_d = < [\frac{1}{r} \frac{\partial \psi_0}{\partial \theta} \int -\frac{\partial \psi_0}{\partial r} dt] > \quad (38)$$

Therefore, for periodic interfacial motion, the time-averaged terms can be expressed in the Lagrangian stream function as $\Psi = < \psi_1 > + \psi_d$.

Rallabandi *et al.* evaluated the bubble dynamics considering both 2-D and 3-D configuration of bubbles and made significant contribution to the field of acoustic microstreaming.[36,37] The knowledge can be applied to the microstreaming phenomenon in lateral cavity acoustic transducers as well (LCAT) for cell separation and fluid flow in microfluidic devices as evident in next chapter.

Lateral Cavity Acoustic Transducers (LCATs)

In this thesis, we are applying the acoustic microstreaming to lateral cavity acoustic transducers (LCAT) for selective cell capture from blood and disease diagnosis. LCAT device generates microstreaming with the help of a microfluidic channel comprising an array of dead-end side channels or cavities. When this device is primed with a fluid, air gets trapped in the dead-end side channel and behaves like a bubble. The oscillation of these interfaces, upon actuation by an acoustic source, leads to the formation of a first order periodic flow (Fig. 3a) within the fluid. At the boundary, the magnitude of the acoustically excited flow is given by

$$U_0 \sim d\omega$$

Where, U_0 is the first characteristic flow velocity of cavity induced microstreaming which is velocity of oscillating flow due to oscillatory motion of air-liquid interface in response to incident acoustic wave, d is the interface displacement amplitude and ω is the angular frequency of the acoustic field. The first order periodic flow induces a steady second-order streaming flow (Fig. 3a) near the air-liquid interface whose magnitude is given by

$$U_s \sim \frac{U_0^2}{\omega r}$$

Where, U_s is the second-order characteristic velocity of streaming flow which arises due to the net displacement of fluid parcels during each air-liquid interface oscillation cycle, and R is the equivalent radius of the air-liquid interface.

Previous work has shown that microstreaming flow at air-liquid interfaces can trap particles and the trajectories are dependent on particle properties such as size and density.[38] Wang *et al.*[34] demonstrated that larger size particles occupy smaller orbits while smaller particles occupy larger orbits in the perpendicular cavities. They explained that particles are unable to penetrate into the gas phase of the air-liquid interface, and that streaming flow generates closed loop vortices. Therefore, the center of particles of different sizes will be aligned with different close loop streamlines resulting in size-dependent orbits as shown in Fig. 3c, where the 15μm particles are forced into a streamline closer to the center of the vortex compared to that of a 10μm particle. We are utilizing an external syringe pump to introduce a bulk flow into the device, similar to Wang *et al*.[35], where they observed that particle release from streaming flow was dependent on the ratio of mean bulk flow velocity, U_b and the velocity of streaming flow, U_s. The release or trapping of a particular sized particle was determined by a value termed as d_{gap}. They noted that there is a critical streamline that separates closed streamlines from open streamlines and the fluid below this critical

streamline must flow through a width of d_{gap}, which is between the bubble surface and critical streamline. Since the particles cannot penetrate the bubble, particles with a diameter greater than $2d_{gap}$ will be are pushed away from the bubble such that the center crosses the closed streamline, causing it to trap. However, if the diameter of the particle is less than $2d_{gap}$, the center of the particle will remain in the open streamline causing it to release from the streaming flow as shown in Fig. 6c.

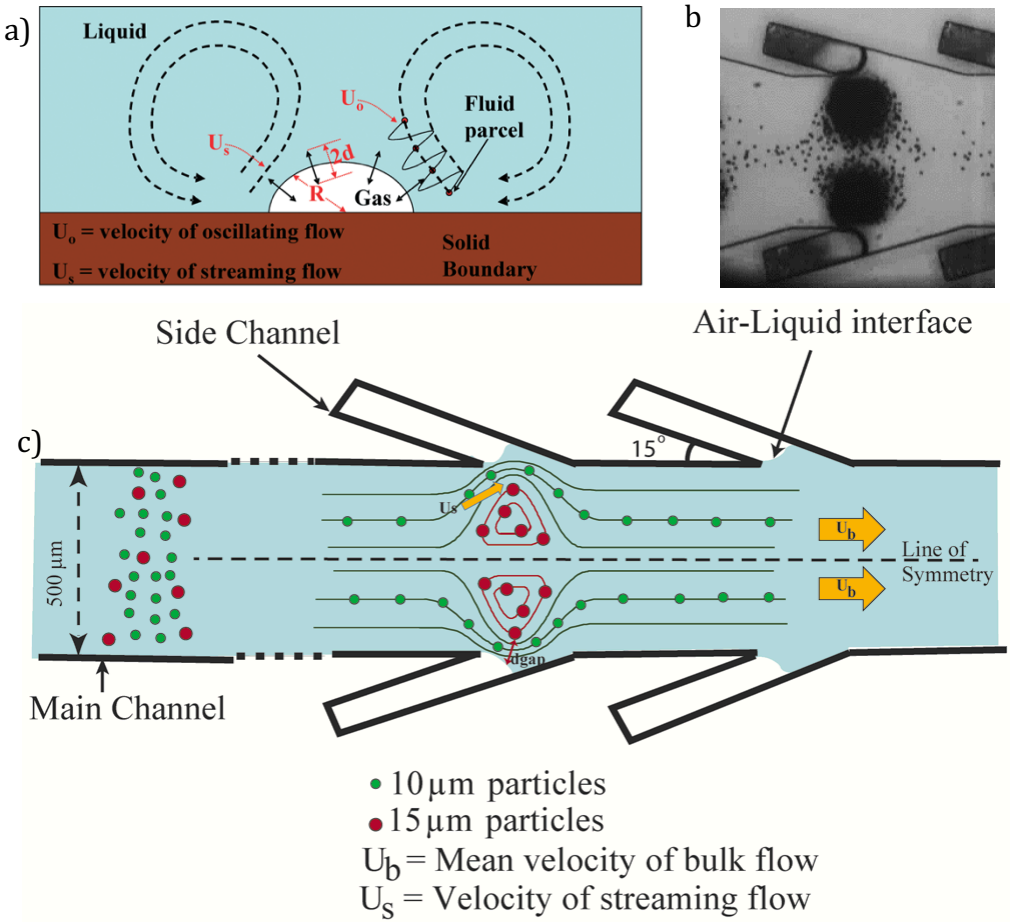

Figure 6: LCAT device operation. a) Representation of the first-order (U_0: Solid line) and second-order (U_S: dashed line) characteristic velocities at air-liquid interface. Reprinted with permission from reference number 38. Copyright © 2014 The Royal Society of Chemistry.

b) Bright-field image showing the trajectory of the particles in the device with a mixture of 10 μm diameter (million/ml) and 15μm diameter particles (10,000/ml). c) Schematic of the device showing the open and closed circular streamlines for particle/cell separation and enrichment.

This separation mechanism can be applied to the LCAT device as well and considering the symmetry of the air-liquid device along the long axis, the threshold value of U_b/U_s ratio can be determined to separate particles of different sizes. This separation will lead to trapping of larger sized particles in the streaming flow which further will help in enrichment in a small volume. Due to the symmetry, volumetric flow rate can be assumed to be divided evenly along the long axis of the microchannel. Based on continuity theory, the total flow rate through half of the cross-sectional area of the microchannel (V_1) must be equal to the flow rate through a narrow gap of air-liquid interface (V_2):

$$V_1 = U_b \frac{w}{2} H \; and \; V_2 = U_s d_{gap} H$$

Where, W and H are the width and height of the microchannel, respectively. Equating V_1 and V_2 and solving for d_{gap}, results in:

$$d_{gap} = \frac{U_b}{U_s} \frac{W}{2}$$

Therefore, in order to allow 10μm diameter particles to release, while trapping 15μm particles, a d_{gap} between 5μm and 7.5μm would be required. Considering 500μm as the channel width, 10μm particles should begin to release from microstreaming vortices when $U_b/U_s = 0.02$ while 15μm should begin to release when $U_b/U_s = 0.03$. Hence, an U_b/U_s ratio between 0.02 and 0.03 would allow 15μm particles to be trapped and releasing 10μm particles from microstreaming vortices, resulting in size-based separation.

Materials and Methods

Device Fabrication

1. LCAT alone device: The LCAT chip is composed of 200 LCATs spaced 200μm apart at an angle of 15° relative to the main channel. The main channel width and the side channel width were fixed to 500μm and 100μm respectively. The height of the device was remained constant to 100μm. Microfluidic devices were fabricated using soft lithographic techniques. Silicon wafer was first cleaned with 2% HF to render it hydrophobic and dehydrated at 120°C for 15minutes. Negative photoresist, SU-8 2050 was spin coated per manufacturer's (Microchem) protocol for 100μm height. Following spin coating, it was soft-baked, exposed, post baked and developed. After hard baking at 200°C, it was kept in silane overnight. Poly (dimethylsiloxane), PDMS (Sylgard 184, Dow Corning) base and curing agent at 11.5:1 ratio was mixed and poured on the mold. Following degassing in a desiccator, it was cured at 65°C overnight. Hardened PDMS was cut and peeled carefully. Inlet hole was punched with a 1.5mm biopsy punch and the outlet was cut. After cleaning the device, it was bonded on a thin cover slip (Fisher Scientific) using standard plasma procedure (Harrick). Following oxygen plasma, the bonded device was kept on a hot plate set at 65°C overnight to make the device hydrophobic.

2. Spiral iMF + LCAT device: The devices were fabricated using standard soft lithography. PDMS (polydimethyl siloxane) was cast on a mold fabricated using SU-8 (MicroChem) as negative photoresist. After curing PDMS at 65ºC for 2 hours, it was peeled and bonded to a glass coverslip (0.17 mm thick) using standard plasma bonder (Harrick). Bonding to

coverslip was done to ensure efficient actuation and induction of acoustic field and the device was kept on a hot plate at 65°C overnight to render hydrophobicity.

3. HIV-HPV-HSV multiplexed device: To fabricate the microfluidic device, we patterned SU-8 photoresist 2050 onto a 3-inch silicon wafer following the manufacturer's protocol for a height of 100 μm to fabricate the first layer with LCATs. Following that we aligned the second layer (50 μm height) with MA-56 aligner (Karl Suss) to fabricate VCATs. Polydimethylsiloxane (PDMS) was cast onto the wafer at a ratio of 1:11.5 (curing agent: base). Following the punching of inlet and outlet holes, the PDMS device was reversibly bonded to a microscope slide bearing nitrocellulose pads using a solution of Rain-X.

Cell sample preparation and analysis

1. MCF-7 cell culture: MCF-7 breast adenocarcinoma (HTB-185) cell line was procured from ATCC (Manassas, VA) and cultured per ATCC instruction in DMEM (Mediatech, Manassas, VA) supplemented with fetal bovine serum (10%), penicillin (100U/mL), streptomycin (100g/mL) (Mediatech, Manassas, VA), and Novolin R insulin (44U/L) (Novo Nordisk, Plainsboro, NJ).

2. SKBR-3 cell culture: SKBR-3 breast adenocarcinoma (HTB-30) cell line was procured from ATCC (Manassas, VA) and cultured as per ATCC instructions in RPMI (Mediatech, Manassas, VA) supplemented with fetal bovine serum (10%), penicillin (100U/mL), and streptomycin (100g/mL) (Mediatech, Manassas, VA).

3. DU-145 cell culture: DU-145 cells were cultured as a monolayers on a T-75 cell culture flask. ATCC-formulated Eagle's minimum essential medium was used as the basal medium to which fetal bovine serum (FBS) was added (10% by volume). After the cells reached desired confluency, the culture medium was discarded and the adherent cells layer was

rinsed with 1X PBS. 2.5mL of Trypsin + EDTA was added to the flask to disassociate the adherent cells. Cells were observed to have disassociated in approximately 3 minutes. Cells were then transferred to 10mL Eppendorf tube and 7.5 mL of the growth medium with FBS was added. Cells were then centrifuged at 1000rpms for 5min and the pellet was re-suspended in 10mL growth medium.

Biomarker Staining

1. Anti-Human EpCAM CD326 antibody: For biomarker staining on MCF-7 cells, anti-human EpCAM CD326 antibody conjugated with PE-Dazzle 594 (Biolegend) was used. After obtaining the cell pellet in an Eppendorf tube, they were blocked by adding 60uL Staining buffer (1% BSA, 0.1% NaN3 in 1X PBS, pH 7.4) to re- suspend cell pellets with 20µL of FcR block (Miltenyi Biotech) for 10 minutes. Appropriate volumes of antibody stain (3µg/mL) was added and incubated for 30 minutes on ice. Following incubation, the cells were washed with staining buffer and collected by centrifugation at 1000rpm for 5min. These pre-stained cells were observed under fluorescence and spiked in whole blood at appropriate concentrations.

2. DAPI: For nuclear staining of WBCs, we added DAPI (4', 6-diamidino-2-phenylindole) stain (Fisher Scientific) at the concentration of 1mg/mL and incubated the sample for 10min. Following that, we imaged the stained cells using DAPI filter of the fluorescent microscope.

Viability assay: Viability of cells were tested by using Trypan Blue viability test. In this test, the dye is taken up by dead cells which turns them blue, whereas live cells stay clear. Cell samples (10 µL each) were taken from inlet, outlet 1 (non-target cells) and outlet 2 (target cells). 10 µL of Trypan Blue was added to each of the sample. Live cells were counted by

ImageJ using a Countess cell counting chamber slide (Life Technologies) to determine the viability of cells in each sample.

3. Wright-Giemsa Staining: The blood cells after separation were stained using Wright-Giemsa Stain (Electron Microscopy Services). After making the smear of whole blood and its separated components (RBCs and WBCs), the cells were fixed and stained using Wright-Giemsa stain for 5 minutes. The glass slide is then washed in DI water carefully and dried for observation under the microscope.

Sample preparation for Monocyte isolation

De-identified male blood sample was obtained from Institute of Clinical and translational science, Irvine. All normal donor blood was processed within 24 hours after withdrawal. The blood sample was diluted to 10× by adding 0.9% saline or 1x PBS. This diluted sample was then infused into the integrated platform using a single syringe pump at the volumetric flow rate of 1.1mL/min. The PZT was actuated at 6.5 Vpp allowing larger monocytes to be trapped in the micro-vortices and subsequent collection at the outlet of the platform. On collection at the outlet, the collected monocytes were stained with CD14 antibody for confirmation. The protocol for CD14 antibody staining involved blocking the collected cell sample with FcR block (Miltenyi biotec) by addition of 60 µL of Staining buffer (1% BSA, 0.1% NaN3 in 1X PBS, pH 7.4) for resuspension of cell pellets and addition of 20µL FcR. The samples were incubated on ice for 10 min. 4 µL of CD14-PE dazzle 594 (Biolegend) antibodies were added to stain the samples for 30min/on ice. The stained sample was then washed twice with 1mL of staining buffer and then centrifuged at 1000 rpm for 5min. The cell pellet was then resuspended in fresh staining buffer and analyzed on a counter slide using a fluorescent microscope (TRITC filter).

Protein Expression and Microarray Printing

Mature HIV, HSV and HPV proteins were amplified by PCR, inserted into plasmid expression vectors, expressed by coupled *E. coli* based *in vitro* transcription and translation (IVTT) and printed on nitrocellulose coated slides. Approximately 1 nL (~0.4 ng protein of interest) of each IVTT reaction was spotted onto 16-pad nitrocellulose coated Oncyte Avid Slides (Grace Bio-Labs) using an OmniGrid Accent microarray printer (Digilab) equipped with a 946 Printhead and 946 MP4 Spotting Pins (ArrayIt). This array contains 56 of the most sero-reactive HIV proteins produced by IVTT, from HIV-1 subtypes A1, A2, B, C and D as well as HIV-2 groups A and B, plus 13 HIV glycoproteins produced in mammalian cells obtained from the NIH AIDS Reagent Repository, 34 of the most seroreactive HSV-1 and HSV-2 proteins and 24 of the most sero-reactive HPV proteins from nine publicly available subtypes: HPV-1, 2, 6, 11, 16, 18, 35, 43 and 56. All HSV and HPV proteins used were produced by IVTT.

Serum and Saliva Sample Collection and Processing

Anonymous blood and saliva samples were collected from normal volunteer donors at UCI with IRB approval and informed consent. Blood samples were centrifuged at 1300 rpm for 10 minutes to separate serum from cells. Saliva was collected using Sarstedt Salivette devices and processed according to the manufacturer's recommendations. Deidentified HIV+ sera and saliva samples were kindly provided by the Consortium for the Evaluation and Performance of HIV Incidence Assays. One-half percent Triton X-100 was added to the samples to inactivate viruses.

Chapter 1

LCAT Based Whole Blood Cell Sorting, Enrichment and Characterization

This chapter is adapted from the work "Neha Garg, Trisha M. Westerhof, Vick Liu, Robin Liu, Edward L. Nelson, Abraham P. Lee. Whole-Blood Sorting, Enrichment and *in situ* Immunolabeling of Cellular Subsets Using Acoustic Microstreaming. *Microsystems & Nanaoengineering*, 2018, 4, 17085."

1.1 Introduction

Efficient separation of cellular populations from whole blood is an essential preparatory step for many biological and clinical assays.[39] Conventional macro-scale cell sorting techniques include density gradient based centrifugation, immunolabeling-based separation such as fluorescence activated or, magnetic-activated cell sorting (FACS, MACS, respectively) and CellSearch. However, these techniques are limited by separation sensitivity, large blood sample volume requirement, multi-step interventions prone to

artifacts, processing time, and cost. Lab-on-a-chip and microfluidic systems developed for microscale separation techniques have been gaining importance over the past decade. Many types of unique cell sorting and enrichment devices have been devised but they are not usually able to work with unprocessed whole blood.[40–43] These technologies typically require pre-processed samples and cannot handle the physical properties and complex populations inherent in whole blood.[44–48] They are limited to either diluted [49,50] or lysed blood [51,52], and in some cases, density based centrifugation to reduce blood complexity and cell-cell interactions.[53–59]

The microfluidic cell sorting technologies that can handle whole blood, in general fall into two categories: label free sorting based on physical characteristics of the target cells or biomarker labeling. For example, Davis *et al*.[60] utilized deterministic lateral displacement (DLD) to separate whole blood components. Nagrath *et al*.[61] used microposts and Stott *et al*.[62] utilized herringbone structures to capture EpCAM+ CTCs from whole blood. In another study, Karabacack *et al*.[63] integrated DLD with inertial focusing and magnetophoresis for negative isolation of CTCs from whole blood. Although they successfully demonstrated target cell sorting, they were unable to enrich in a small volume (<50μL).

Acoustic microstreaming has been demonstrated in previous chapters to focus, sort and enrich target cells/particles within the microchannel.[64–66,38,35,67,34] Studies have shown negligible adverse effect of ultrasonic actuation on cellular phenotypes, viability and functional capacity.[38,47,59,68] In addition, as explained above, LCATs are capable of bulk pumping of the sample while simultaneously separating particles/cells by size based on the bubble surface oscillation amplitude. The oscillation thus controls the trapping and releasing of particles, correlated roughly to the ratio between bulk and streaming velocities. As

depicted in Fig. 7a, LCATs integrate the following sample processing steps 1: separate whole blood into its cellular constituents, 2: enrich rare cells based on size, and 3: deliver fluorescent biomolecules (monoclonal antibodies) to selectively label target cells. These functions allow one to identify target cells based on two important characteristics – size and surface biomarkers in a single device. Here, we are utilizing enrichment ratio (ER) as a metric to analyze the device performance.[53,69,70] It is defined as the enhancement of target cell to background cell ratio from the device input to the output sample.[70] ER in the order of ~100x to 1000x is clinically significant for subsequent gene profiling by RT-PCR as discussed by Tong *et al*.[52,71] In our device, we enhanced the ER to 170x for particle mixture (15 and 10μm at initial ratio 1:1,00,000). We achieved 213x enrichment of MCF-7 cells with respect to WBCs when spiked at 10 cells/mL in whole blood while ensuring the capturing of all target cells and thus avoiding false negatives.

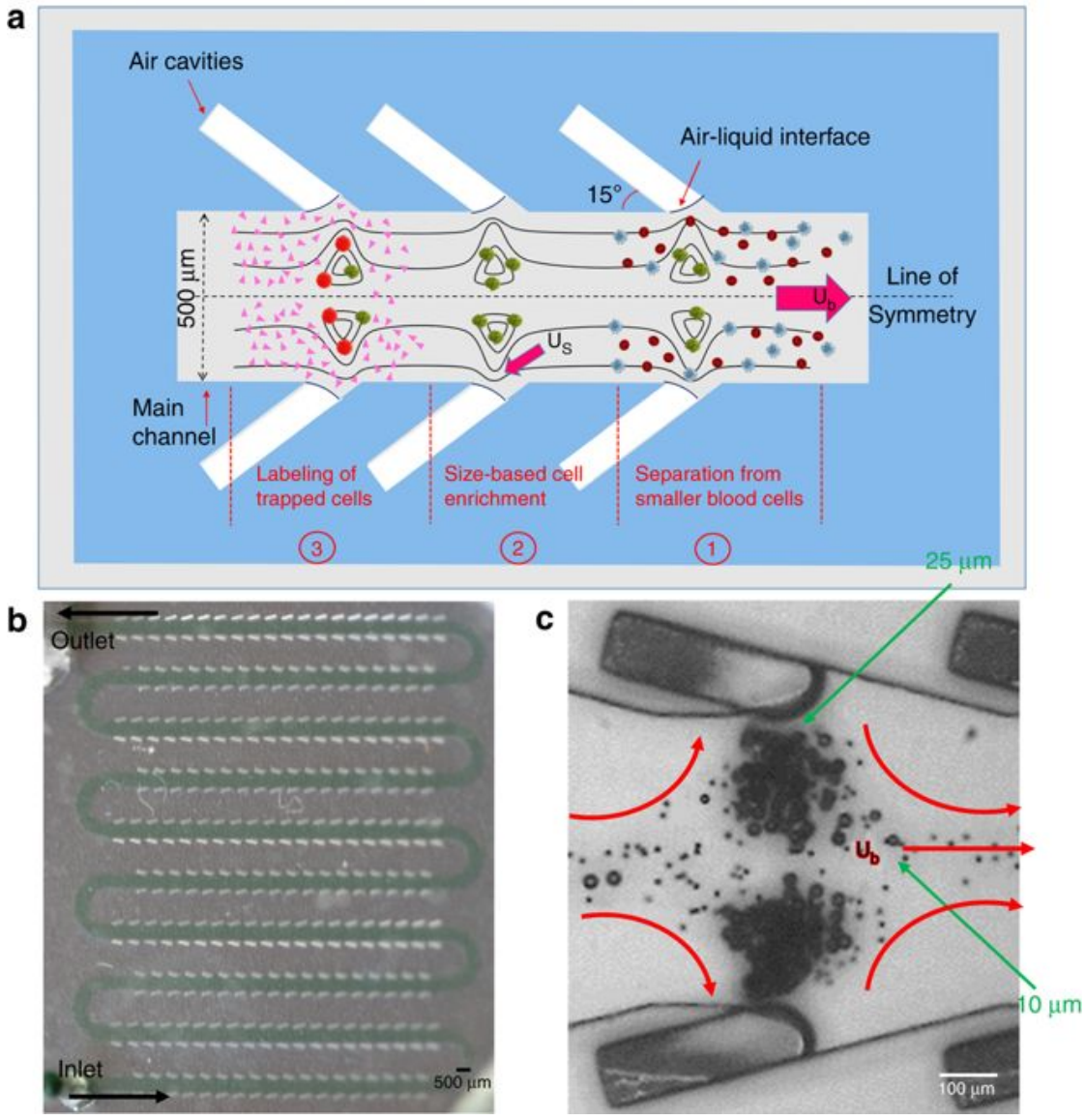

Figure 7: Device schematics for blood sample preparation. a) Illustration of size-based separation, enrichment and *in situ* immunolabeling in the LCAT device. b) Image of the polydimethylsiloxane (PDMS) based LCAT device. c) Bright-field image showing the trapping of 25µm sized particles in the closed circular streamlines and release of 10µm sized particles via open streamlines

1.2 Size based sorting from whole blood

At $2V_{pp}$, the PZT vibration induced the pumping of plasma and small platelets in the blood, but RBCs and WBCs were trapped in the vortices formed by the microstreaming flow (U_s). This resulted in the collection of 2μL of fluid enriched for plasma and platelets from the outlet. As the PZT voltage is increased to $2.5V_{pp}$, the increase in U_b/U_s results in RBCs being released from the microstreaming vortices and collected from the outlet. To increase the purity of separated sample, excess blood was pipetted out of the inlet and replaced with 30μL of PBS buffer. The device remained driven at $2.5V_{pp}$, until all RBCs were flushed out by the buffer. After collecting all the RBCs from the outlet, the voltage was further increased to $4.5V_{pp}$ to release remaining trapped WBCs. The separated samples were kept in individual vials for inspection.

The plasma and platelet sample were viewed in bright field at 40X on a countess slide while the whole blood, and RBC samples were stained with Wright-Giemsa stain to distinguish them within (Fig.8a, 8b). WBC samples were spotted on a fluorescent microscope using DAPI nuclear stain (Fig. 8b, right) followed by the morphological analysis as shown in Fig. 8d. By utilizing imageJ software for enumeration, the plasma sample consists of 96.3% platelets, the RBC sample consists of 90.8% RBCs, and the WBC sample consists of 66.4% WBCs (Fig. 8c).

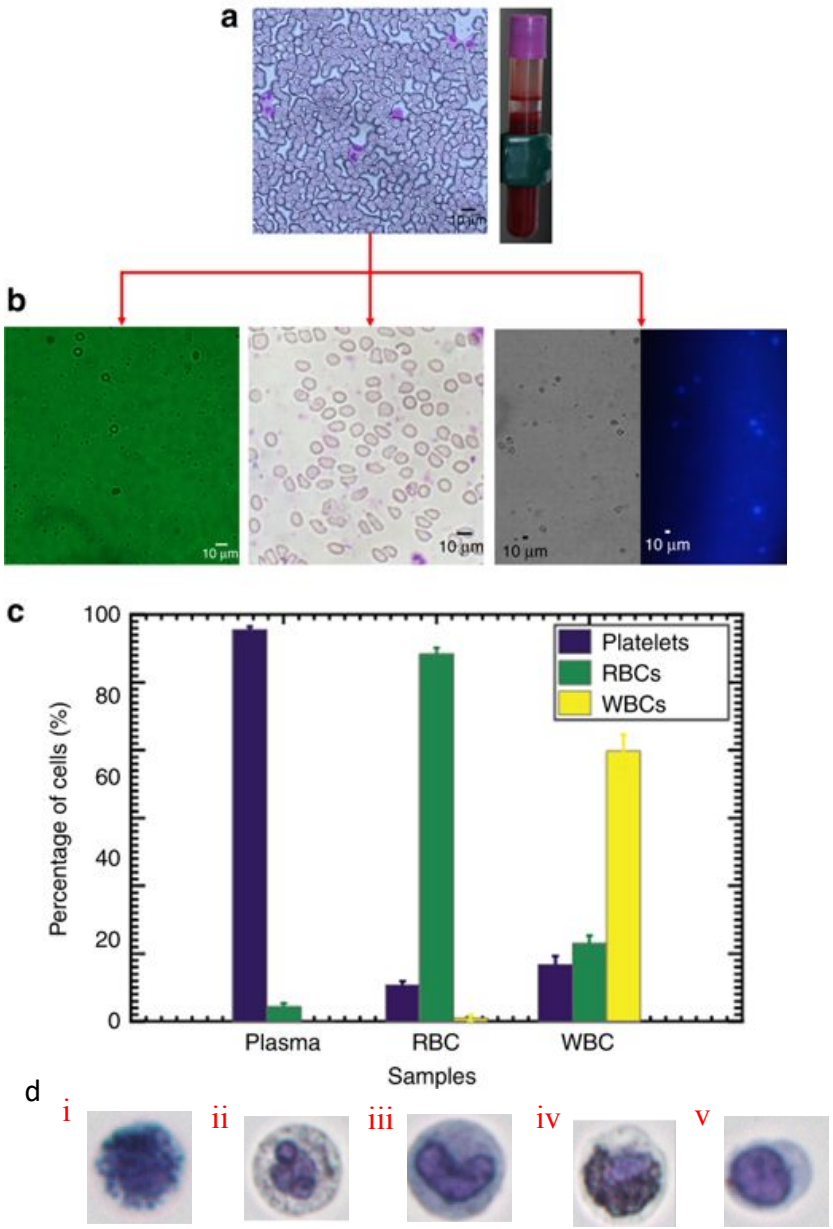

Figure 8: Experimental observations for sample preparation of whole blood. a) Smear of the whole blood stained with Wright-Giemsa stain (left), 10 ml vial of the whole, unprocessed blood. b) Bright-field image of the sample containing platelet rich plasma (left), Bright-field image of the smear of the RBC sample after sorting from device (middle), Bright-field and fluorescent image (DAPI) of WBC sample after device operation (right). c)

Bar graph showing the percentage of cells in each sample after sorting in the device (n=3). d) Bright-field image showing intact cell membranes of different WBC types (i) Basophil, (ii) Neutrophil, (iii) Monocyte, (iv) Eosinophil, and (v) Lymphocyte (stained with methylene blue, crystal violet and eosin Y) after acoustic exposure by LCAT

1.3 Size-based sorting with *in situ* immunolabelling

In some cases, rare cells such as circulating tumor cells or cancer-associated fibroblasts also exist in our circulatory system. Separation and enrichment of these rare cells is of prime interest for both prognosis and treatment monitoring. Post-separation analysis such as identification and enumeration can be performed by immunofluorescence and is unaffected by the presence of non-target cells in the output sample. Currently, despite considerable automation along with blood handling and separation, detection by immuno-staining of target cells is performed manually. The standard staining procedure takes at least one hour, and requires expensive centrifuges to collect cells maintained in suspension. To maximize the utility of lab- on-chip devices in point-of-care setting, we have integrated size-based separation with biomarker expression based immunolabeling. This enables our device to integrate complete hematological separation of cellular subsets and on-chip immunofluorescent labeling to confirm the identity of captured cells of interest based on both size and biomarker, reducing turnaround time, minimizing labor-intensive sample preparation, and limiting cost.

For proof of concept, MCF-7 breast cancer cells ($2.1x10^5$ cells /mL) were prepared into a single cell suspension. The LCAT device excitation voltage was set to capture the larger MCF-7 cells, followed by on-chip staining with anti-human EpCAM mAb conjugated to

PE/Dazzle 594 (Biolegend). 30µL of MCF-7 cell suspension in PBS was pumped at 2.5V_{pp} from the LCAT device inlet for 5min. After the cells were trapped in the microstreaming vortices, 20µL of Fc block (Miltenyi Biotec) was added in the inlet after removing the extra cell sample. Fc block was flown for 5min followed by pumping 4µL of CD326 (0.8µg anti-EpCAM) antibody for 2min (2µL/min). To prevent the inlet from emptying and air entering the channel, 30µL of staining buffer (1% BSA, 0.1% NaN3 in 1X PBS, pH 7.4) was added to the inlet for 3min. The buffer also served to wash out any unbound antibodies in the channel. After the cells were immunolabeled in the device, the fluorescent cells were imaged on-chip using a fluorescent upright microscope (Fig. 9a). Subsequently, stained MCF-7 cells were released at 4.5-5V_{pp} to analyze the fluorescent intensity and the morphology.

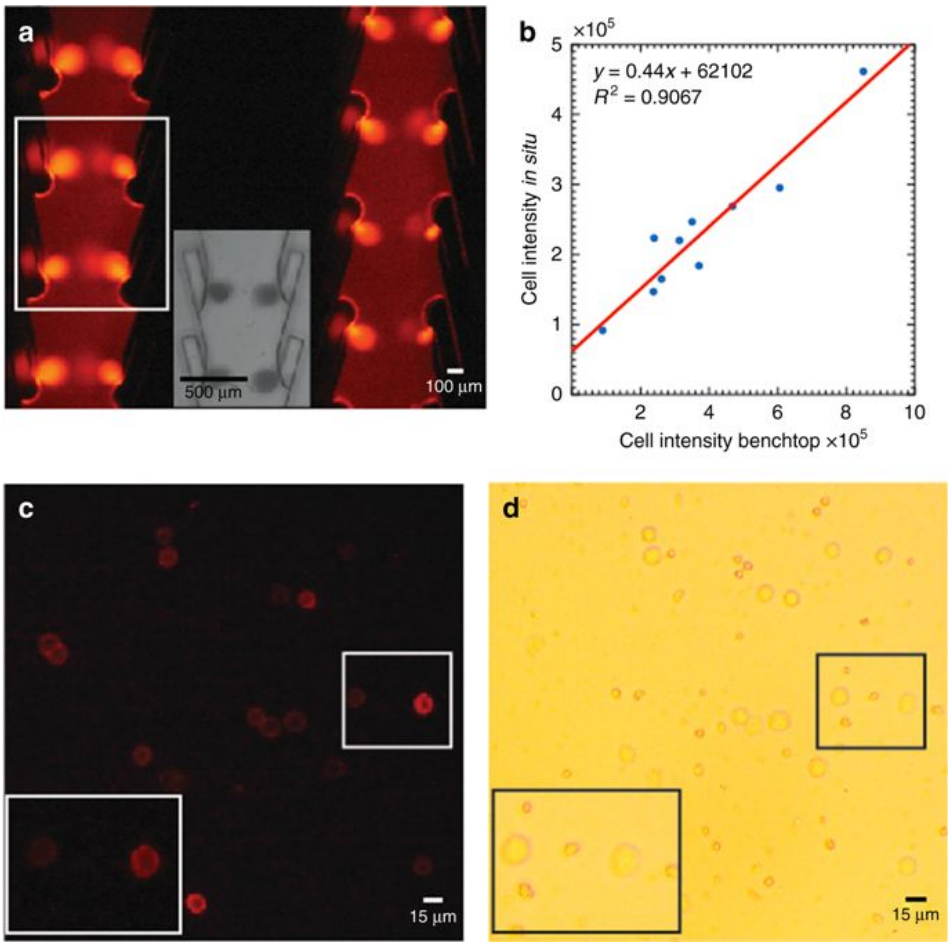

Figure 9: *In situ* immunolabeling of MCF-7 cells from blood. a) Fluorescent image of MCF-7 cells stained while trapped in device. Inset: Bright-field image of the boxed region. b) Plot of intensity correlation between staining protocol on device with benchtop staining (n=3). c) Fluorescent image of MCF-7 cells after sorting, enriching, and on-chip labeling. d) Bright-field image of the released sample containing WBCs (smaller) and MCF-7 cells.

We compared the detected expression level of the MCF-7 cells stained using a standard benchtop procedure (0.8µg, incubation time of 50-60min) to the 15min *in-situ* chip based staining procedure and a correlation of 91% demonstrates the similar expression level detected via on-chip staining regardless of the shortened staining time (Fig.9b). After optimizing the immunostaining protocol, we sought to produce a more realistic case by spiking MCF-7 cells into normal donor whole blood samples (50,000 cells/mL). The spiked blood samples were run through the device, with the intent to separate the cancer cells from the blood. Platelets and RBCs were first extracted, followed by pumping of 30µL of RBC lysing buffer (Gibco) for 5min to ensure complete removal of RBCs from the microstreaming vortices. As a result, a mixture of remaining WBCs and MCF-7 cells remained trapped at the microstreaming vortices. At this point, we immunostained the MCF-7 cells with anti-EpCAM antibody to discriminate them from the remaining WBCs on the device using the protocol described above and released the mixture at 4.5-5V_{pp}. The released sample of 20µL was placed on a countess slide, and imaged using a fluorescent filter (Fig. 9c), as well as bright field (Fig. 9d). 10x ratio increment (ER 9.71x) for fluorescently labeled MCF-7 cells with respect to WBCs confirms the identification and enumeration of target cancer cells specifically based on both size and marker expression, which is particularly important for clinical blood samples.

1.4 Device optimization at rare concentration

At this point, we demonstrated a quick and portable technique for separating blood components and detecting target cancer cells by immunolabeling on a single device. While the size of circulating tumor cells ranges from 15-25μm, the rate of occurrence is 1-10 cells/mL of whole blood, thus making them extremely difficult to track.[72] Since rare cell detection requires a large sample volume to process and to identify, enumerate and analyze, we used an external syringe pump. Efficient generation of bubble induced steady streaming flow and retaining constant bubble response to the chosen resonance frequency in LCAT device depends on controlled bubble shape and size. Since the LCAT device is fabricated with soft-lithography techniques using PDMS, its gas permeability is one of the reasons for bubble growth and shrinkage. The LCAT device was primed with an aqueous solution of 10% glycerol in lipid to maintain the stability of air-liquid interfaces and increase the time of operation.[73] Due to an external bulk flow, it was imperative to optimize the device with respect to flow rate and the voltage applied to PZT.

1.4.1 Device Operation

After the air-liquid interfaces were stabilized with the help of lipid and glycerol, we decided to optimize the device based on the operational parameters such as voltage, flow rate and time of operation. The sample solution used for the characterization of the device is a mixture of 10 and 15μm sized polystyrene particles (density = 1.06g/mL) at the concentration of million particles/mL and 10,000 particles/mL respectively. The sample solution was made in DI water with sucrose for density matching with BSA and tween 20 to prevent the coagulation of the particles and attachment on the device. The priming of the device to form the air-liquid interfaces was done with aqueous solution of 10% glycerol in

lipid at 10μL/min. During the process of particle trapping and releasing, we collected the waste containing 10μm sized particle populations from the outlet with both syringe pump and PZT ON. After the device operation, the trapped particles were released in 20μL after the PZT was switched OFF and pump ON. We performed the calculations for particle counts in ImageJ using 10μL volume in countess slide by taking fluorescent and bright field images of 15 and 10μm diameter particles respectively. ~100% trapping of 15μm diameter particles was confirmed by observing no fluorescent particle in the waste sample. We are using enrichment ratio as a quantitative measure to analyze the performance of the device which is defined as:

$$Enrichment\ Ratio\ (ER) = \frac{(Target\ cells/Background\ cells)\ output}{(Target\ cells/Background\ cells) input}$$

1.4.2 Flow rate as a parameter

Bulk flow velocity focusses the smaller non-target particles along the center line of the channel also called as line of symmetry. To carry out the separation from a larger volume of sample, we utilized an external syringe pump to introduce the bulk flow velocity, U_b. Flow rate has a direct correlation with bulk velocity (U_b). At low voltages, enrichment ratio decreases with an increase with flow rate due to increment in U_b/U_s beyond 0.03, which leads to the release of target 15μm particles (Fig. 10a). However, at high amplitudes (>2.5V_{pp}), enrichment ratio increases first and then decrease as shown in Fig. 10b. With larger Us and smaller value of U_b, U_b/U_s falls within the range and goes to maximum enrichment ratio of 8.5x at 25μL/min and 2.75V_{pp}. The decrease in enrichment ratio at flow rate lower than 25μL/min is due to U_b/U_s smaller than 0.02, leading to trapping of non-target smaller particles as well.

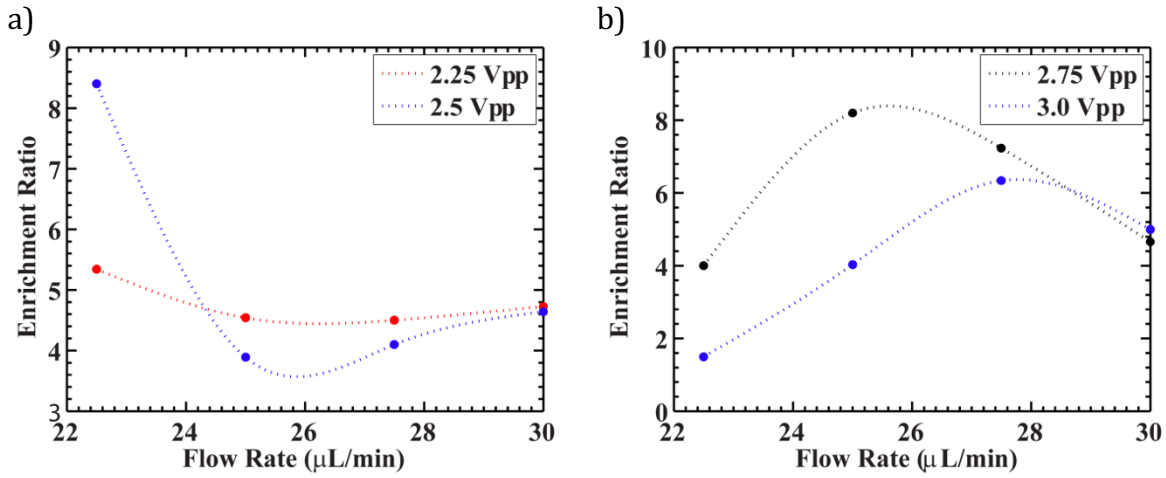

Figure 10: Dependence of enrichment ratio on flow rate for low (a), and for high (b) voltage values

1.4.3 Voltage as a parameter

The efficient trapping of target larger particles in microstreaming vortices and removal of non-target smaller particles in bulk flow depends on the competition between microstreaming velocity (U_s) and bulk flow rate (U_b). For complete trapping of 15μm particles and release of 10μm particles, $0.02 < U_b/U_s < 0.03$. At 25μL/min and 2.75V_{pp}, highest enrichment ratio of 8.5x was observed (Fig. 11b), due to U_b/U_s values in the interval [0.02, 0.03]. U_s increases with amplitude increment leading to decrease of U_b/U_s. As the ratio of U_b/U_s becomes lower than 0.02, non-target smaller particles start to trap in microstreaming vortices. This leads to reduction in enrichment ratio for voltage values greater than 2.75V_{pp}. At lower values of amplitude, lower U_s makes U_b/U_s higher than 0.03 where target 15μm particles are also not fully trapped and starts to release, providing low enrichment ratio. Similar trend was observed for flow rates 22.5μL/min and 25μL/min.

1.4.4 Operation with particle sample

After the operation parameters were achieved, enrichment ratio obtained was 8.5 due to trapping of approximately 40% of non-trapping 10μm sized particles in microstreaming vortices. To increase the purity and ER, we devised a washing and voltage switching procedure by applying a short pulse at low voltage while keeping bulk flow at the same rate (U_b) (Fig. 7a). When U_s decreases by reducing the PZT voltage to $2V_{pp}$, the increase in U_b/U_s ratio allows 10μm particles to be released. To prevent 15μm particles from releasing, this voltage is maintained for only 30sec. After that, the flow from the syringe pump was switched off and the voltage was increased to $3.5V_{pp}$ for 1.5min to remove 10μm particles by the LCATs own ability of generating bulk flow. We removed 78.2% of non-target 10μm particles (Fig. 11c), achieving 30x ER from the same starting material as above. To test at practical occurrence rate, we reduced the spiking concentration of 15μm particles to 10 particles/mL and achieved 170x ER with ~100% trapping efficiency (Fig. 11d and 11e).

Data presented up until this point utilized mixtures of 10μm and 15μm diameter particle. However, human erythrocytes and other hematopoietic subsets are much smaller in size. Therefore, to better represent the smaller diameter and heterogeneity of whole blood samples, we used a mixture of 7.32 (million/mL), 10 (million/mL) and 15μm (10,000/mL) diameter particles to mimic erythrocytes, leukocytes, and CTCs respectively. This mixture was flown in the device and 15μm particles were trapped while releasing 7.32 and 10μm particles at operation conditions same as above. The enrichment ratio 15μm particles was 39 with respect to 7.32μm particles and 28 with respect to 10μm particles.

1.5 Device validation with spiked particles and cultured cancer cells from unprocessed blood

Data shown at this point utilized micro-particles to represent peripheral blood mono-nucleated cells (WBCs) and CTCs. So, it is imperative to test the device capability of handling non-Newtonian whole blood sample comprising billions of deformable RBCs, platelets and leukocytes. This has been confirmed by spiking 25 and 15μm diameter particles in whole blood and enriching them while removing non-target RBCs and WBCs.

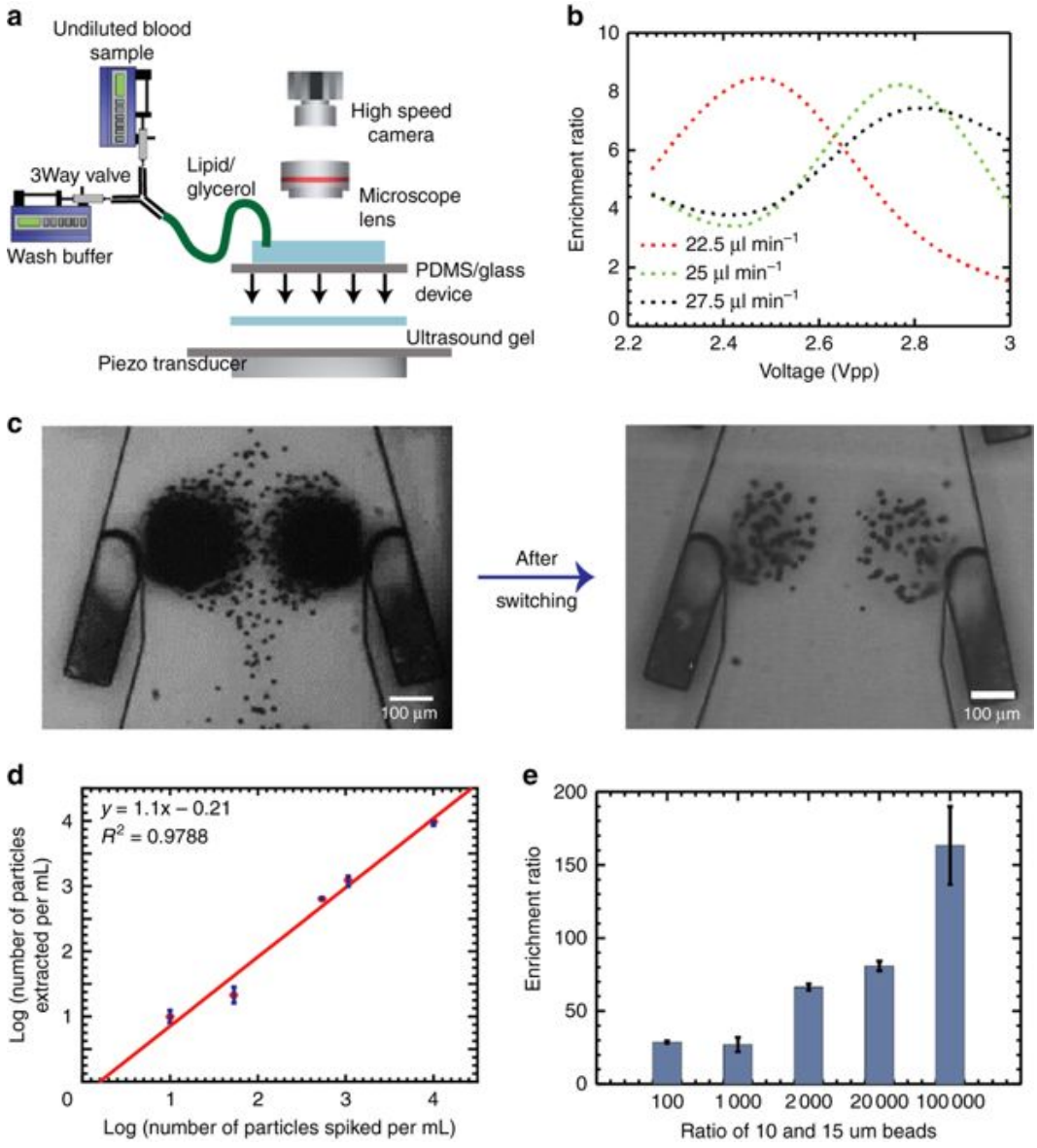

Figure 11: LCAT device validation with beads. a) Operational set-up with external syringe pump. (b) Device optimization with respect to flow rate and voltage. (c) Bright-field image showing vortices before (left) and after voltage switching (right). Plot of (d) trapping efficiency, and (e) enrichment ratio for 15μm sized particles at different concentrations in the presence of million per ml non-target 10 μm diameter particles (n=3).

We started with spiking particles with largest size in CTC spectrum and chose 25μm diameter particles labeled with Fluoresbrite® fluorophore having excitation (excitation maxima 441nm) and emission spectra (emission maxima 485nm) similar to fluorescein isothiocyanate (FITC). Whole blood from healthy donors was obtained from Institute for Clinical and Translational Science (ICTS) at UCI after the IRB approval. We chose the spiking range of the particles from 10,000/mL (Fig. 12d) to 10/mL to demonstrate the rarity in whole blood volume. The parameters for device operation were kept same as above: 25μL/min bulk flow rate, 2.75Vpp and 49.8 kHz resonating frequency of PZT and the air-liquid interfaces were made directly with blood. These interfaces behaved similar to the lipid-glycerol solution due to the high viscosity of blood and the presence of lipids/proteins in it. We imaged the device with the help of an upright microscope connected with high speed camera, phantom and observed the channel filled with RBCs as shown in Fig. 12a. After the blood flow for approx. 14min, we used 1X PBS to wash off the device and remove non-target cells. The assembly for the washing step was kept same as above with the help of 3-way valve. PBS was flown for approx. 20min which includes voltage switching. Due to the larger size of the particles, we gave the short pulse at $2.25V_{pp}$ for 30sec to release smaller RBCs/WBCs while keeping 25μm particles trapped as demonstrated in Fig. 12b and 12c. After the device operation for 34min, PZT was switched off and the trapped cells were

released in 20μL volume. We counted the trapped 25μm sized particles in the fluorescent image taken on countess slide with the help of imageJ and observed an enrichment ratio of 70x with respect to WBCs keeping in mind their initial concentration to be 1million/mL (Fig. 12e). We repeated the same procedure at low concentrations and achieved an enrichment ratio of 531x at spiking concentration of 10/mL as shown in Fig. 12f.

25μm diameter particles represent the farthest end of CTC size. After observing four 25μm particles from 400μL sample volume, we decided to spike smaller sized particles to represent CTCs and chose 15μm diameter particles. 15μm diameter particles were mixed in whole blood at low concentrations and the spiked sample was operated at similar parameters in the device. We used $2V_{pp}$ for voltage switching to release non-target RBCs and WBCs. Three to four particles were observed in the fluorescent image of the trapped sample (20μL) ultimately giving the enrichment ratio of 479x.

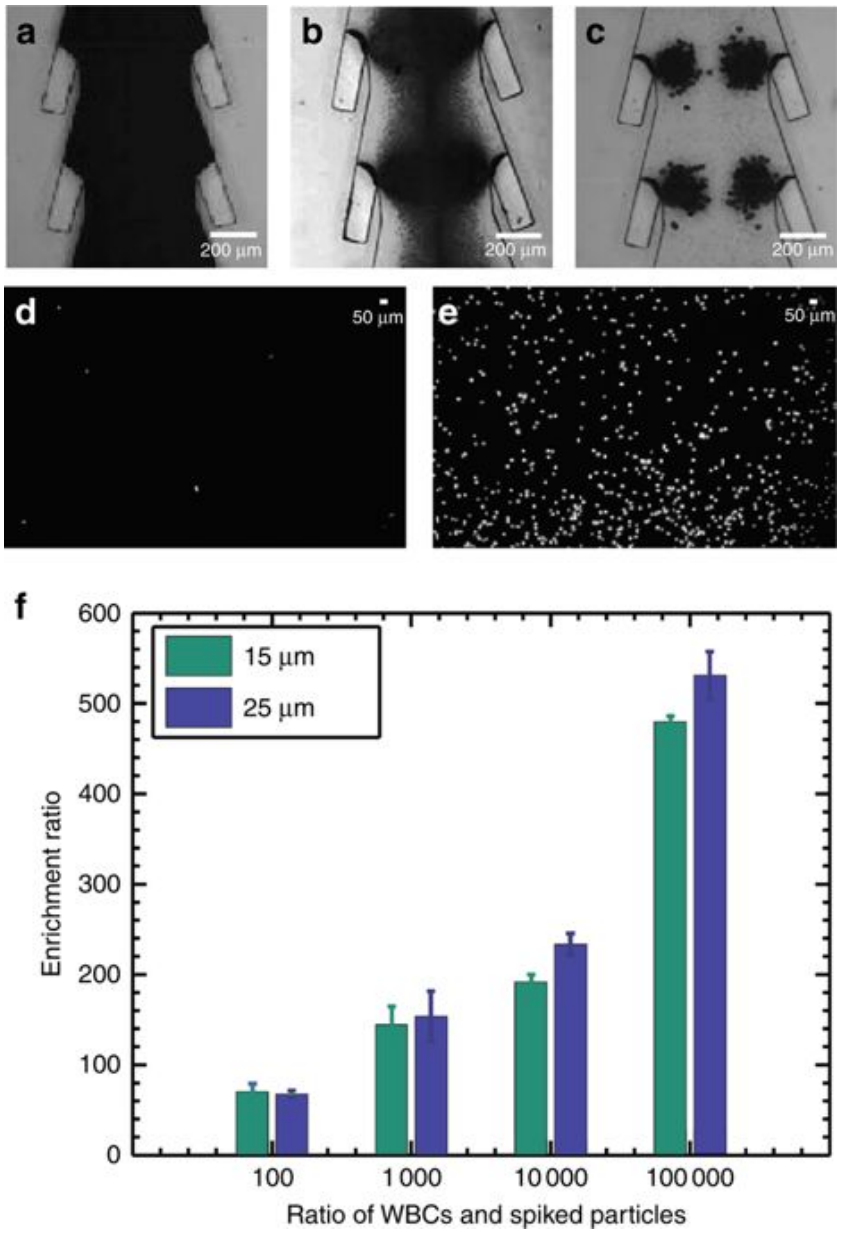

Figure 12: Enrichment of 25/15µm sized particles in whole blood. (a) Bright-field image of whole spiked blood in the LCAT device. (b) Bright-field image during the washing step in the device. (c) Bright-field image of pure vortices with 25µm diameter particles trapped after the device operation. (d) Fluorescent image of initial spiked blood (with 25µm diameter particles) at 10,000 per ml concentration. (e) Fluorescent image of enriched 25µm sized particles after releasing from device. (f) Plot of enrichment ratio with varying

spiking concentration of 25and 15μm diameter particles (n=3) for each spiking concentration.

As a final proof-of-concept experiment, the separation and enrichment of MCF-7 breast cancer cells from whole blood was demonstrated. MCF-7 cancer cells in suspension were immunofluorescently stained with anti-EpCAM antibody and then spiked into normal donor whole blood at concentrations ranging from 1,000/mL to 10/mL. The trapping and enrichment of MCF-7 cells was performed using the same protocol described in the sections above. After processing 400μL of spiked blood sample (separately spiked with 25μm, 15μm and MCF-7 cells) for 34min, we could capture and image 3-4 particles (Fig. 13a, 13b) and 4 cells (Fig. 13c) when they were spiked at initial concentration of 10/mL in whole blood, thereby giving ~100% trapping efficiency (Fig. 13e). After counting the fluorescent MCF-7 cells in the final sample, we obtained 213x enrichment at 10/mL spiking concentration (Fig. 13f). In addition, we cultured the enriched MCF-7 and SKBR-3 cells for 3 days in conditioned media to ensure the preservation of phenotypic and genotypic characteristics after ultrasound exposure and obtained successful proliferation after acoustic exposure as shown in bright field images (Fig. 13d). We immunostained MCF-7 and SKBR-3 cells in culture with DAPI antibody and obtained multiple nuclei as shown in Figure 13d (right).

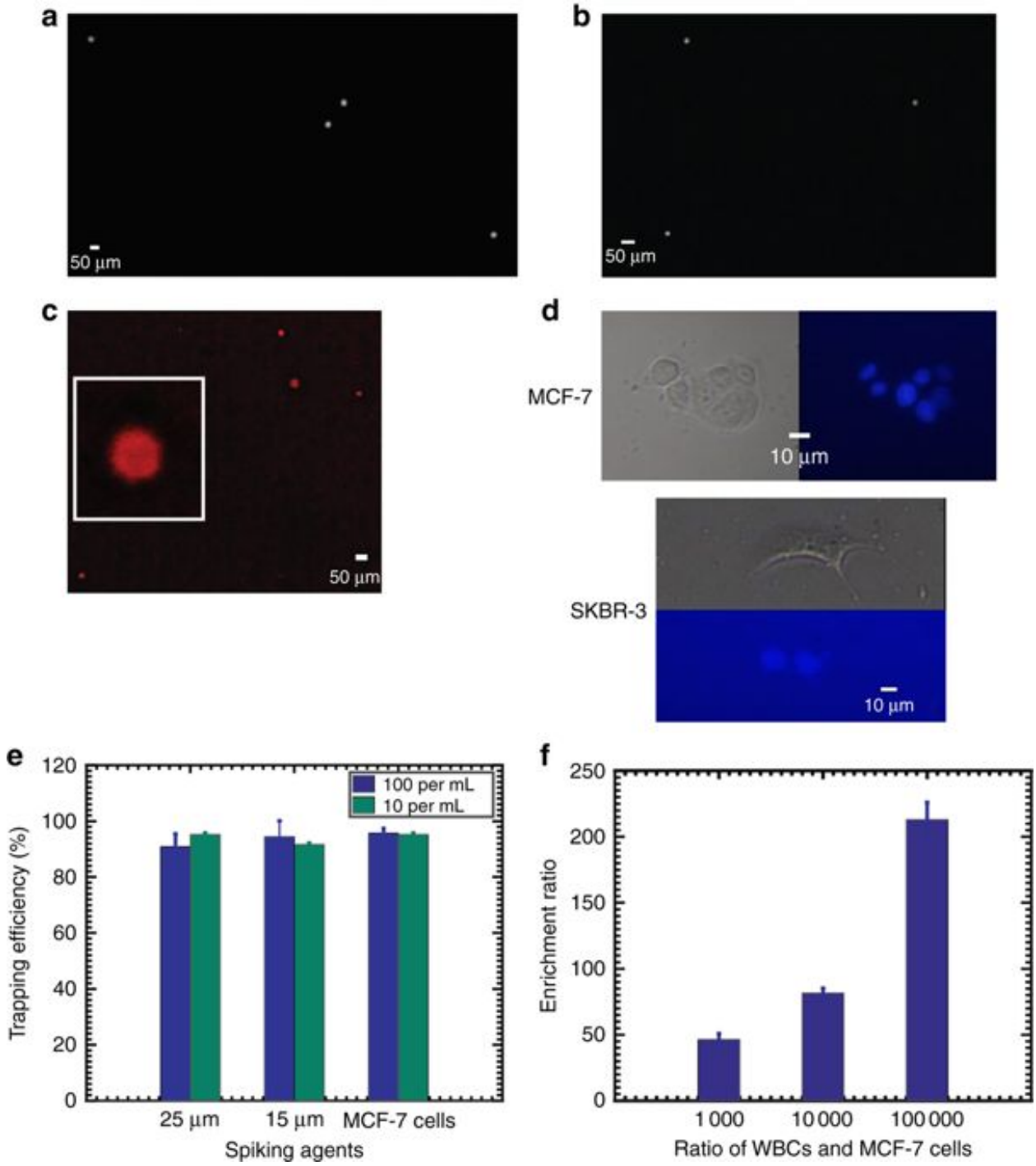

Figure 13: Enrichment of 25µm, 15µm and MCF-7 cells in whole blood. Fluorescent image of (a) 25µm, (b) 15µm and (c) MCF-7 cells released after analyzing 400µl of whole blood sample in device at 10/ml spiking level. (d) Bright-field and fluorescent image (DAPI)

showing the MCF-7 (top) and SKBR-3 (bottom) proliferating on the culture plate. (e) Plot of the trapping efficiency for 25μm, 15μm diameter particles and MCF-7 cells at 100/ml and 10/ml spiking concentration in whole blood (n=3). (f) Plot of enrichment ratio with varying concentration of MCF-7 cells in whole unprocessed blood sample (n=3).

1.6 Discussion

Rare cells in the circulatory system carry significance for improving cancer prognosis and monitoring treatment response.[39] The ultimate goal of liquid biopsy based detection of rare cells requires a multi-modal system that can process raw samples by separating, sorting and enriching for specific cell populations, and finally identifying the targeted cells via known biological markers.[74] Typically, each of these processes require separate instruments and the transfer of samples across different platforms, resulting in lowered sensitivity, specificity, and added costs.

As described here, our LCAT rare cell isolation platform can process whole blood without dilution, separate out the cellular subcomponents, isolate and enrich the targeted size-based population, and perform in situ immunolabeling. There is no other liquid biopsy system that can achieve this level of integration and multi-modal functionality. For example, the first category of rare cell detection platforms relied on surface biomarkers (e.g. EpCAM) and the binding to antibody-coated surfaces to filter and concentrate rare cells such as CTCs. However, it is now well known that cancer cells can undergo EMT (epithelial to mesenchymal transition) in circulation, causing undesired false negatives.[1] Another promising category of microfluidic systems is “label-free”, and they are able to sort blood cells based on their sizes using known techniques such as deterministic lateral displacement (DLD),[60,75] inertial microfluidics,[76] and acoustophoresis.[58,59,77] However, recent developments in oncology have

shown heterogeneity and great size overlap between rare cells such as CTCs and healthy WBCs.[57,78] Being able to separate blood cell sub-populations with fine resolution to define a size threshold that ensures ~100% capture of targeted rare cells, and then identify the targeted cells within this concentrated population via gentle immunolabeling in situ is a powerful combination of techniques needed for liquid biopsy. An integrated system that is multimodal, label-free, biomarker compatible, low cost and can be fully automated has enormous potential to make clinical impact. In this paper, our device has demonstrated the enrichment of MCF-7 cells from whole blood at concentrations as low as 10/mL, at ~100% capture efficiency, and verified by EpCAM biomarker staining in situ. In contrast, although hydrodynamic vortices based devices demonstrated cancer cell enrichment up to four orders of magnitude, it required significant blood dilution to avoid cell-cell interactions and the capture efficiency was only ~20%.[49] Another enormous advantage of this LCAT platform is in the speed of operation for cell enrichment and identification. Considering just the downstream analysis and enumeration of target cells after enrichment, benchtop immunostaining and fixation could take several hours. However, to develop an inexpensive and automated point-of-care device, we labelled the captured target cells in situ within 15mins and achieved 91% correlation in the fluorescence intensity by optimizing the LCAT pumped bulk flow.

While our system has great potential for liquid biopsy, it may be limited by throughput due to the low flow rate and the instability of LCATs over time. Inertial microfluidics-based devices are high-throughput (mL/min) but require significant dilution. Our strategy to improve throughput is to parallelize LCAT devices and increase the total blood sample volume it can handle. We are also optimizing the length of the sorting

microchannels to maximize microfluidic channel length while minimizing hydrodynamic resistance. Another possibility is to flow a second pass of the enriched 20μL sample in the device to reduce the volume required in the first place since it is likely the enrichment ratio will be greatly improved.

Overall, this chapter demonstrates a highly promising approach for integrated isolation, enrichment, release and identification of targeted blood cells, and ultimately could lead to the development of complete point-of-care blood diagnosis. The technology, based on acoustic microstreaming, processes whole blood and does not require centrifugation or benchside processing of separated blood components. Thus, an offshoot of this technology is to create a complete blood sample preparation front end device able to separate each of the blood cellular component (platelets, RBC and WBC), as each of these components contain critical information for the diagnosis of physiologic and pathologic conditions such as infectious diseases and inflammatory responses.

1.7 Conclusion

An acoustic microstreaming based LCAT device that can process whole blood and all its cellular constituents by size-based sorting, enrichment, and subsequent biomarker-based identification is reported. This is, to our knowledge, the first demonstration of a single microfluidic device that combines the advantages of both label-free detection and *in situ* immunolabeling to select for targeted specific cell types. It is also the first device that can separate and collect the major components in whole blood (platelet rich plasma sample, RBCs and WBCs). Rapid immunolabeling (15min) was demonstrated as targeted cells were trapped in microstreaming vortices. With these novel integrated functions, we demonstrated ~100% trapping efficiency of spiked polystyrene beads and MCF-7 cells in whole blood and

achieved ~200x enrichment ratio in the sorted sample of 20μL for concentrations as low as 10/mL.[79]

Chapter 2

Integrated Device for High-Throughput Sorting and Enrichment

This chapter is adapted from the work "Nivedita. Nivedita*, Neha Garg*, Abraham P. Lee, Ian Papautsky. A High Throughput Microfluidic Platform for Size-Selective Enrichment of Cell Populations in Tissue and Blood Samples. *Analyst*, 2017, 142, 2558-2569."

2.1 Introduction

The field of microfluidics has seen rapid development in the last decade, especially for applications involving isolation and enrichment of cells or particles.[80,81] Enrichment of cells is particularly critical to sample preparation of complex biological fluids and heterogeneous cell samples, for a variety of applications.[80–82] For example, sub-populations of cancer cells have been associated with stem cell like properties[83–85] and may offer insights into cancer progression and metastasis,[83,86–88] while heterogeneity in peripheral blood monocytes has been linked to differentiation into mature tissue macrophages, osteoclasts

and dendrite cells.[89,90] The advantages of using microfluidic sorting and enrichment systems lie in ease of use, small sample volume requirements, high efficiency, cost-effectiveness and disposable platforms, along with a wide range of separation modalities based on both physical and chemical properties of cells or particles.[81,82]

Passive microfluidic devices based on pressure driven flows, hydrodynamic forces and micro-channel geometry present promising sorting systems with high throughput (1–2 mL min^{-1}), but they are limited to size-based selectivity and subsequent purity of the sample obtained. In addition, active approaches based on an external force field for particle/cell isolation are highly selective and present high isolation efficiency but suffer from low throughput.[91,92] In this chapter, we present a novel integrated microfluidic platform that combines a passive sorting technique with an active enrichment method for high throughput, size-selective isolation of cells. The concept is illustrated in Fig. 14a. At the front end of the platform, a spiral inertial microfluidic (iMF) separator (developed in collaboration with Dr. Ian Papautsky's lab) exploits inertial focusing and Dean flows to remove non-target cells at high processing rate and directs the remaining sample to a lateral cavity acoustic transducer (LCAT) at the back end, for further selective enrichment of the target particles/cells (Fig.14b). The integrated platform was first characterized using polystyrene particles and the limit of enrichment was tested by spiking particles in blood. Following parametric optimization, the integrated platform was tested for two applications: enrichment of larger sub-population of prostate cancer cells derived from brain metastasis (DU-145 cells)[93,94] and enrichment of larger monocytes from human peripheral blood. The inherent mismatch between the operational conditions and design restrictions for each of the two systems presented a number of design challenges that needed to be addressed before integration.

Thus, we first optimized each system individually keeping the channel height fixed in both systems for ease of fabrication. The payoff of this optimization and subsequent integration was the successful combination of two distinct sample preparation steps of extraction, isolation, and enrichment in a single platform with sorting throughput of 50 million cells/min, >85% sorting efficiency and 44,000x enrichment with respect to RBCs. The demonstrated work is particularly relevant for applications requiring selective enrichment of particles/ cells from a complex mixture, such as biochemical assays, enrichment of a cell population from a tissue biopsy (such as sub-population of cancer cells) or isolation of rare cells (such as larger monocytes) from blood.

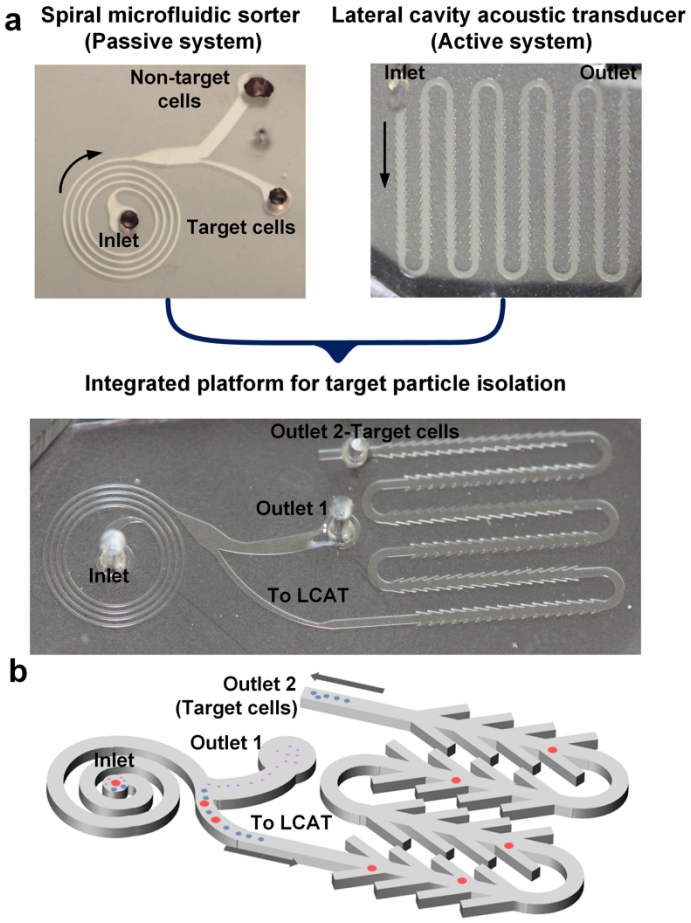

Figure 14: An integrated platform for the separation of particles from blood. (a) A spiral iMF device is integrated into the front end for RBC extraction, with an LCAT in the back end for target cell isolation and enrichment. (b) Schematic illustrating the size-based separation dynamics in the integrated platform

2.2 Spiral iMF cell extractor

Sorting of particles using the concept of inertial microfluidics is facilitated by the effects of inherent hydrodynamic forces within a laminar Poiseuille flow on motion of particles in a microchannel.[95–97] In flows with a moderate Reynolds number (Re) ($\sim 1 < Re < \sim 200$), these effects cause the suspended particles to focus in distinct streams according to their size. The net lift force (F_L) acting on these microparticles is highly dependent on their diameter and can be defined as

$$F_L = \rho G^2 C_L {a_p}^4 \quad (1)$$

where ρ is the carrier fluid density, a_p is the cell (or particle) diameter, C_L is the lift co-efficient, and G is the shear rate that is dependent on flow velocity and characteristic length.[95,96,98]

In a curved rectangular microchannel, the net lift force interacts with curvature induced Dean drag (due to Dean vortices) leading to a single equilibrium position per particle size.[50,95,99] The Dean drag force (F_D) can be defined as

$$F_D = 3\pi\mu U_D a_p \quad (2)$$

where μ is fluid viscosity and U_D is the average Dean velocity. Since the ratio of net lift force and Dean drag is highly dependent on bioparticle size ($F_L/F_D \, \alpha \, {a_p}^3$), the balance of two forces can be adjusted to manipulate the focusing positions of particles according to their respective sizes.[95,99] Suspended particles migrate towards a single focusing position near the

inner channel wall where the force due to Dean drag balances the net lift force, leading to particles equilibrating near the center of inner channel wall with the largest particles focusing closer to the wall (Fig. 15a). This concept has been exploited to develop spiral inertial microfluidic devices to successfully sort cells according to their size.[50,99,100] For example, Kuntaegowdanahalli *et al.*[99] used Archimedean spiral to separate neural cells with ~80% efficiency and Nivedita *et al.*[50] further improved the spiral sorter for high throughput, high efficiency (~90%) plasma and blood sorting. Guan *et al.*[101] used spiral channels with trapezoidal cross section for >90% WBCs enrichment. In this work, we have exploited the existing concept of spiral sorting to develop a high throughput, continuous RBC extractor that is both integrable and highly efficient.

2.2.1 Parametric optimization

To confirm the focusing positions for the integrated device, we first optimized the spiral iMF extractor separately using polystyrene particles of sizes comparable to target cells, WBCs and RBCs. These size- ranges were selected to represent blood cells since blood is the most commonly tested biological fluid. As such, a number of other human biological samples such as cancer cell lines DU-145 or HPET (human prostate epithelial/hTERT cancer cell line) often have the comparable cell size range of 7-30μm.[93,94] The Archimedean spiral design was optimized to an aspect ratio of 0.5. The inner diameter was fixed at 2mm with the input port of 1mm diameter. Center-to-center distance between each of the spiral loops was fixed to 200 μm, with the width of the channel being 200 μm and height 100 μm. For parametric optimization, we used a mixture of polystyrene particles of diameter 7.32 μm (standard deviation, σ = 0.53 μm) to represent smaller cell sizes/non-target cells and 25 μm (σ = 2.5 μm) diameter particles to represent larger target cells. The two sizes

represented the opposite ends of the spectrum of the intended sample mixture. Unlike previous designs, we designed the outlet system with an asymmetric bifurcation. This asymmetric bifurcation causes the majority of flow to elute into outlet 1 (non-target cells) and only a small portion of the flow near the inner channel wall elutes into outlet 2 (target cells to LCAT). This allows for a very efficient separation of the focused streams of 7.32 and 25 μm diameter particles, as described below.

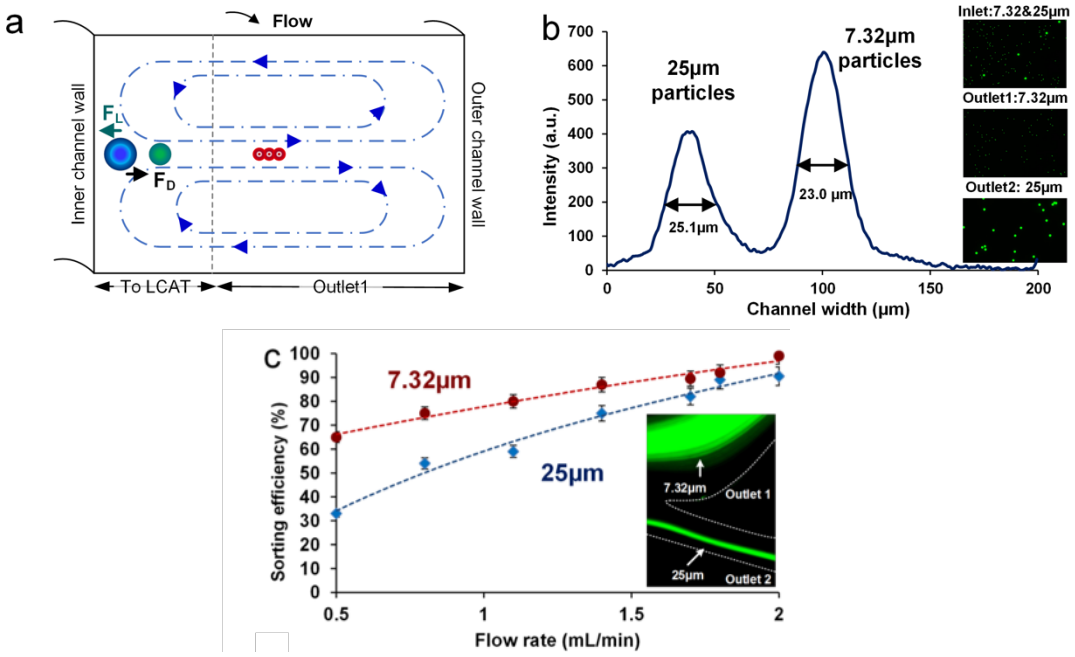

Figure 15: Design and optimization of spiral iMF cell extractor. (a) Schematic of formation of cross-sectional Dean vortices in a curved rectangular channel and the cell/particle focusing regime. (b) Intensity plot across the channel width at the outer-most loop and before the expansion in the spiral sorter. Insets show the images of the collected sample at the inlet, outlet 1 and outlet 2. (c) Plot of the sorting efficiency of 25 and 7.32 μm diameter particles eluting into outlet 1.

At $Re \sim 160$, the 25 μm diameter particles focused in a single stream near the inner channel wall and 7.32 μm diameter particles focused in a band near the center of the channel. The intensity plot across the channel width at the end of the outer-most loop of the spiral, shows the peak of focused stream of 25 μm diameter particles with the FWHM (full width at half maximum) of 25.11 μm, indicating a tightly focused stream (Fig. 15b). The second peak in the plot with the FWHM of 23.02 μm shows the band of 7.32 μm diameter particles focused towards the center of the channel (Fig. 15b). The insets in Fig. 2b show samples collected at the inlet and each of the outlets indicating the efficiency of separation. Sorting efficiency was then quantified as a function of flow rate and with respect to each of the particle sizes in the mixture (Fig. 15c). Sorting efficiency (SE) was calculated by counting the total number of particles/cells in each outlet.

$$SE = \frac{N_a}{(N_a + N_b)} \times 100$$

where N_a is the number of target cells in the desired outlet (outlet 2) and N_b is the number of target cells in other outlet (outlet 1). Flow rate was not increased beyond 2 mL/min as it transitions into unstable secondary flow regime and disturbs the desired focusing regime. For $Re \sim 165$, >90% efficiency of sorting 7.32 μm particles was observed, indicating that the spiral iMF exactor could provide a high throughput and highly efficient solution for RBC extraction in the integrated system. The separated sample with larger target particles/cells could then be further enriched using LCAT.

2.3 Integrated Platform

With LCAT alone device optimization demonstrated in previous chapter, both the iMF extractor and LCAT cell isolator were integrated to provide a novel platform for selective

particle/cell isolation directly from a label-free, *Ht* = 0.5 blood sample and sub-population isolation of DU-145 cell line, as described in the following sections.

2.3.1 Device Operation

Syringe interfaced with clear Tygon tubing and FEP tubing (1/16'' diameter) using luer connector was inserted in syringe pump (New Era) to control the flow rate. For acoustic actuation, function generator (Agilent Technologies) with voltage amplifier (Krohn-Hite Corp.) was used to provide desired amplitude (Vpp) square waveform. These square waves actuated a Piezoelectric Transducer (Steiner and Martins) at a resonating frequency of 49.8 kHz. For individual spiral iMF and the integrated device particle optimization, a mixture of fluorescent polystyrene particles of diameter 7.32 μm (Bangs Lab, S.D. = 0.53μm) (representing RBCs) and 25 μm (Polysciences Inc., S.D. = 2.5μm) diameter particles (representing larger rare cells) was used. The distribution of particles across the channel was observed using an inverted fluorescence microscope (IX-71, Olympus). The images captured by the 12-bit CCD Camera (Retiga Exi, QImaging), were Z-stacked (~10-100 images) using Image J software. The individual LCAT device was optimized using a mixture of 15 μm (Phosphorex Inc., S.D. = 0.140) and 10 μm (Phosphorex Inc., S.D. =1.270) diameter particles. 1''×1'' silicon wafer was glued (Krazy Glue) on the PZT to make the surface more reflective. PZT was mounted on a cover of a standard petri dish using double sided tape. Ultrasound gel (Parker Labs Inc.) was used for improved conduction between the glass cover slip of the device and silicon wafer attached to the PZT. Images were taken using Phantom v310 (Vision Research Inc.) camera by means of an upright microscope (Nikon LV150). The flow was switched from sample to PBS from a second syringe pump maintained at the original flow rate using a 2-way valve. PBS (Life Technologies) was used to release the

trapped particles and collect the enriched sample from LCAT after the function generator was switched off. All cells/particles were counted by ImageJ using a Countess cell counting chamber slide (Life Technologies) under an inverted microscope (Olympus). De-identified male whole blood samples were obtained from Hoxworth Blood Center (University of Cincinnati) or from Institute of Clinical and Translational Science (University of California, Irvine). The blood samples were diluted using 0.9% saline or PBS. For the spiral iMF section of integrated device, bright field images were taken with an exposure of 10 μs and ~10-20 images were stacked to represent the focusing regime. Single images were taken at an exposure of 300 μs for imaging trapped particles in microstreaming vortices formed in the LCAT section of the integrated device.

2.3.2 Particle optimization with particles

After the optimization and parameterization of the individual components of the whole device, we integrated them together to validate the sorting and enrichment in the same, single device. Our integrated platform combines spiral iMF and LCATs for the extraction of smaller non–target cells and subsequent enrichment of larger target cells. As discussed earlier, integration presented a wide mismatch of volumetric flow rate (Q) requirements between the two components. Spiral iMF device demonstrated optimal sorting efficiency at flow rates in the order of Q ~ 1500 μL/min, whereas the LCAT gave high trapping efficiency at Q ~ 25 μL/min. We resolved this 60× gap between the operational flow rates of the two devices by manipulating the pressure drop across spiral outlet system and the interconnecting channel (Fig. 16a). The expansion of channel width to 1000 μm in spiral iMF outlet system aided in sorting by separating the focused streams of particles/cells. Additionally, this expansion allowed distribution of the fluid/sample volume across a larger

width, thereby allowing further sectioning of the flow at the bifurcation/outlets causing a resultant decrease in volumetric flow rate at the entrance of the outlet leading to LCAT (expansion causes reduction in average velocity in m/s). Furthermore, the pressure drop across the bifurcation combined with that of the interconnecting channel reduced the average flow rate to ~35 µL/min at the point of entry for LCAT. This projected reduction in flow rate provided LCAT with the bulk flow needed for trapping of larger cells/particles, although at a higher voltage (6.5V_{pp}) as compared to standalone LCAT device. Based on this concept, we designed an integrated device with the capability of extraction of bulk non-target cells in the first stage (spiral iMF) and entrapment of larger target cells in microvortices from the remaining sample in the second stage (LCAT).

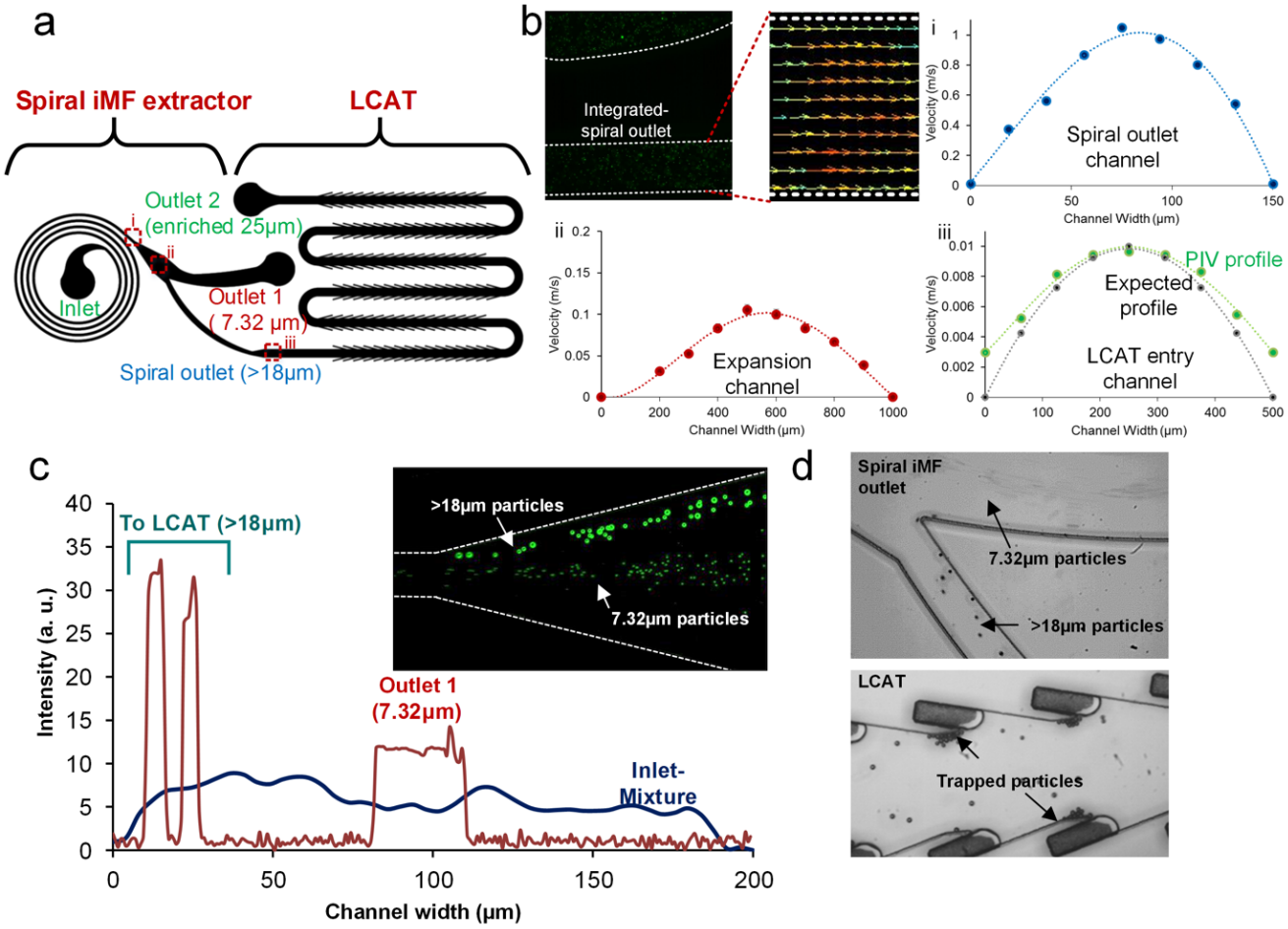

Figure 16: Integrated device design and parametric optimization. (a) Schematic of the integrated device with the spiral iMF and LCAT sections integrated into a single platform. (b) PIV scan and subsequent plots of the velocity magnitude as observed at (i) the spiral outlet channel, (ii) expansion channel, and (iii) LCAT entry channel. (c) Intensity scans across the channel width of the spiral iMF section within the integrated device. The scans were taken at the innermost loop and the outermost look, for the standard deviation z-stack. The inset shows the pseudo colored standard deviation z-stack of the focused 7.32 μm diameter particles and >18 μm diameter particles. (d) Bright-field images of the 7.32 μm diameter particles eluting into outlet 1 and >18 μm diameter particles eluting into the LCAT (top), where they got trapped in the microvortices actuated at 6.5 V_{pp} (bottom).

Integration affected the flow and operational regime in both the components. Since, the trapping efficiency in LCAT depends on bulk flow velocity, the input flow rate at spiral iMF inlet needed to be reduced to reach the optimum value. It was imperative to accomplish a reduction in volumetric flow rate, while maintaining the range of operational parameters and projected sorting and trapping efficiencies as determined in the individual optimization. For this purpose, the height of the entire platform was reduced to ~75 μm. The aspect ratio of spiral iMF was maintained (AR = 0.5) by reducing the width to 150 μm. The input Re was kept at ~160 as determined in the previous sections.

To confirm the appropriate reduction in flow rate within the platform, we performed PIV (particle image velocimetry). The flow was seeded with fluorescently labeled polystyrene particles with diameter 2.1 μm (Fig. 16b). Vector plots were extracted for each of the critical sections in the design namely, (i) outlet channel of the spiral, (ii) expansion channel after the spiral extractor and (iii) LCAT entry channel post the inter-connecting

channel. Fig.16b shows the velocity plots obtained for each of the aforementioned three sections. These plots illustrate the required reduction in the functional flow rate for LCAT to entrap the target particles, while keeping the net/input processing flow rate high.

We started with optimizing the integrated device parameters with polystyrene particles before testing the device with any biological sample. We mixed 7.32 μm and 18+ μm diameter particles (20 μm and 25 μm diameter particles) to simulate the opposite ends of the cell size spectrum in a blood sample. The 7.32 μm diameter particles at a concentration of 10^6/mL represented non-target cells such as RBC/WBCs, while the 18+ μm diameter particles at a concentration of 10,000/mL represented larger target cells such as monocytes or side-populations from tumor biopsies. For the formation of air-liquid interfaces in LCAT section of integrated device, sample solution was directly infused into the integrated device inlet. At $Re \sim 160$, we observed that 7.32 μm particles eluted into outlet 1 and 18+ μm particles eluted into the interconnecting channel leading to LCAT. To illustrate the focusing regime, we plotted intensity scan across iMF channel width at the inner-most loop and the outer-most loop (Fig. 16c). At inner-loop, the entire channel had uniform distribution of particles and as the flow progressed to outer loop, 7.32 μm diameter particles focused in a band, thereby eluting into outlet 1. The 18+ μm diameter particles focused closer to inner channel wall, thereby eluting into the interconnecting channel towards LCAT. The intensity scan was taken using the standard deviation z-stack of the bright field images of focused particles. The bifurcation at asymmetric outlet of spiral iMF was designed to be blunt because sharp corners can often result in formation of microvortices due to acoustic actuation, which in turn can interfere with inertial focusing. Hence, when PZT was turned on, we observed that the particles stay in the desired focusing regions irrespective of slight

focusing fluctuations (Fig. 16d). After the actuation of the device at 6.5 V_{pp}, the 18+ μm diameter particles were trapped in the microstreaming vortices as expected (Fig. 16d). Higher voltages were used for optimal trapping to compensate for the variation of bulk flow rate in the integrated device. Following the parametric determination, we tested the integrated device with particles spiked in human blood sample.

2.3.3 Particles spiked in blood

The inherent hydrodynamic forces acting on cells used in size-based sorting in an inertial microfluidic device are drastically affected by blood rheology. Whole blood is highly viscous and non-Newtonian owing to the concentration of plasma proteins, hematocrit, and leukocyte and platelet counts. Dean vortices have been known to manifest in viscous fluids, however, inertial lift forces which balance the Dean drag to focus the cells and particles in a spiral iMF are substantial only in a Newtonian, Poiseuille flow. To focus cells and particles in the optimized flow conditions, whole blood was diluted to reduce cellular interactions and approach Newtonian flow regime. We initially diluted whole blood with a factor of 20× (hematocrit *Ht* = 2.4%) and spiked it with 25 μm diameter particles at 10,000 particles/mL concentration (Fig. 17a). At *Re* ~ 160, we observed that the particles focused closer to the inner channel wall and eluted into interconnecting channel towards LCAT. RBCs focused in a broad band near the center of the channel and eluted into outlet 1 (Fig. 17b). To further optimize the sorting efficiency of the device, we tested blood samples with dilutions ranging from 20× to 200× and the resulting *Ht* of 2.4% to 0.24%.

Since the dilution factor is dictated mainly by the inertial lift forces required for focusing, sorting efficiency and purity of the 25 μm diameter particles were evaluated in spiral iMF section of the integrated device. As expected, the sorting efficiency improved to

95% with higher dilution owing to reduction in cell-to-cell interaction as well as more precise control over inertial lift forces (Fig. 17c). However, the ideal sample conditions dictate that there should be minimum sample dilution before running it through the device. Since we observed ~85% sorting efficiency at 20× dilution in spiral iMF, we decided to operate the integrated device at 20× dilution or lower and evaluate the enrichment of 25 μm diameter particles in the trapped sample by the LCAT section of integrated device.

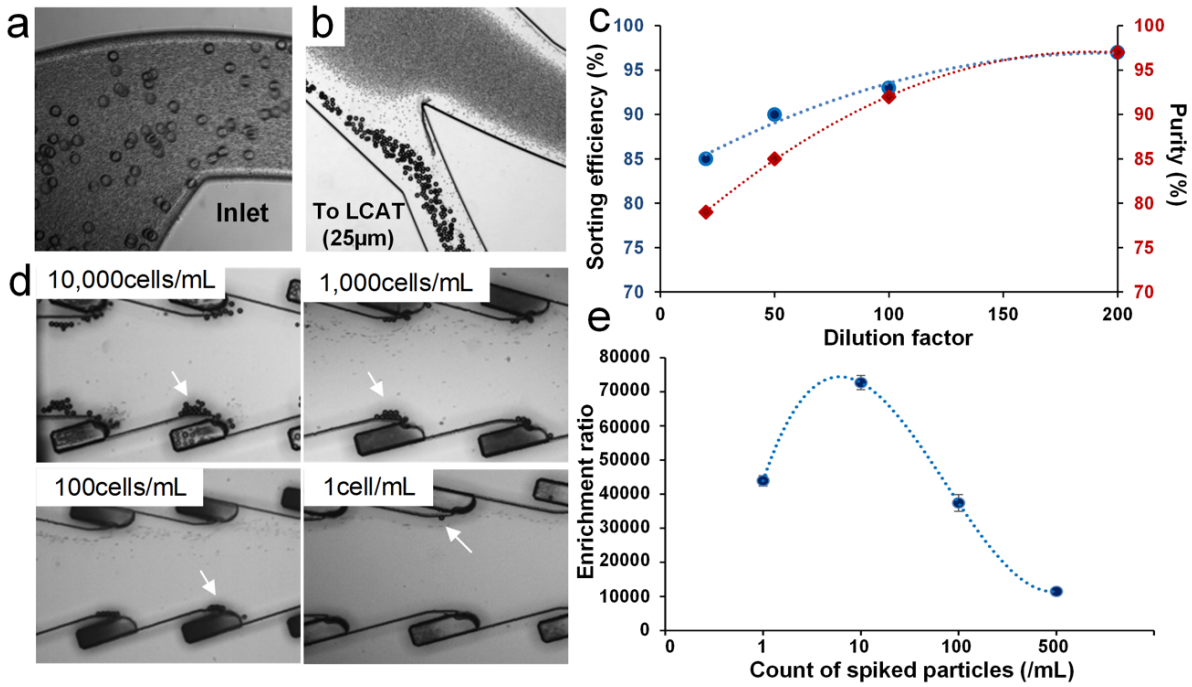

Figure 17: Integrated device operation with particles spiked in blood. (a) z-stack of the bright-field images of 25 μm diameter particles spiked in 20x diluted blood sample at the inlet of the integrated device. (b) z-stack of the bright-field images of the focused 25 μm diameter particles eluting into the interconnecting channel towards the LCAT and RBCs eluting into outlet 1. (c) Sorting efficiency of the spiral iMF in the integrated device for 25 μm diameter particles and the purity of the sample that eluted into the LCAT. (d) Trapped 25 μm diameter particles in microvortices in the LCAT section of the integrated device at

varying spiked concentrations. (e) Enrichment ratio evaluated at each of the spiked concentrations at the input of the integrated device

After the majority of RBCs were separated using spiral iMF, the 20× diluted sample with WBCs and larger particles (25 μm diameter) eluted into the LCAT section for further enrichment. The concentration of 25 μm diameter particles in input blood sample was varied from 10,000 particles/mL to 1 particles/ ml to evaluate the enrichment limit of integrated LCAT. Lower limit of 1 particle/mL was assigned to provide the baseline for extraction at rare concentrations and evaluate the sensitivity of entrapment to extreme requirements. Entrapment of the particles was observed at PZT actuation of $6.5V_{pp}$ (Fig. 17d). In fact, the selectivity was high enough to allow entrapment even at the low concentration of 1 particle/mL. After the collection of enriched samples by flowing buffer (PBS) through the device, we evaluated the enrichment ratio at each spiked concentration with respect to the remnant of RBCs and obtained enrichment ratios on the order of 10^4 (Fig. 4e). Additionally, we observed an increase in enrichment ratio with decrease in spiked particle concentration, suggesting that the device is selective and sensitive enough to sort out even the rarest particle populations. The reduction in enrichment ratio for the concentration of 1 particle/mL (4.4×10^4) can be attributed to the entrapment of non-target particles in the empty microstreaming vortices over time. Hence, the integrated platform provides highest enrichment (8.8×10^4) at the target concentration of 10 particles/mL. We also determined the recovery rate for enriched particles from blood to be 66.6%. These results suggest that the integrated device is capable of successfully extracting smaller non-target cells such as RBCs from the given heterogeneous sample at a high throughput and selectively trapping the desired particles/cells, thereby providing high enrichment of the target particles even at the

lower concentrations. Following the optimization with particles spiked in blood, we tested the platform for two target applications: 1) sub-population isolation of DU-145 cells, and 2) enrichment of monocytes from human blood.

2.3.4 Target applications for cell enrichment

Cell enrichment is particularly vital in fundamental cell biology research. One of the critical questions being investigated, particularly in cancer biology, is the mechanism governing cancer progression and metastasis. Of particular interest are the rare sub-populations of cells within a cancer cell line that have been found to be therapy resistant.[83–85,88,102] These cells are often different in terms of the markers they express, the ability to self-renew, along with being morphologically different from the rest of the cancer tissue.[83–88,103] Hence, size-based enrichment of these sub-populations provides an alternate sample preparation modality for further investigation into their phenotype as well as their migration and invasion properties. Additionally, size-based enrichment of these sub-populations can be used to determine if size is a defining marker for such cells to possess properties of self-renewability (stem-cell like properties). Furthermore, size-based enrichment provides a label-free approach which ensures the maintenance of sample integrity for further investigation and analysis.

We used our integrated platform to significantly enrich (~77×) a sub-population of larger DU-145 cells (>16μm). The DU-145 cell line is derived from the prostate metastatic tumor in brain.[93,94] The cell size range of the DU-145 cell line was found to be very heterogeneous with cell sizes ranging from 7μm-28μm.[93,94] We prepared an input sample with average concentration of 25,000 cells/mL and infused the sample with a rate of ~1.1 mL/min. DU-145 cells are adherent cells, therefore, the cell concentration at the input

sample was maintained at 25,000 cells/mL to ensure that cells don't adhere to each other to form aggregates. We observed entrapment of larger (>16 μm) cells in the microvortices at the optimized PZT actuation voltage of 6.5 V_{pp} (Fig. 18a). The imaging of the outlet sample revealed enriched larger DU-145 cells. We plotted the size-comparison of the inlet sample and the outlet sample for comparison as a box plot, showing significant enrichment of larger cells in the outlet sample (Fig. 18b). The enrichment of DU-145 cells was achieved at a high processing rate of ~28000 cells/mL and high purity of ~91.7%. Additionally, we were able to achieve a recovery rate of 67.5%, which is comparable to the recovery rate obtained for particles spiked in blood. To assess the viability of cells post enrichment, we performed a viability assay using Trypan Blue to determine the number of viable cells obtained after passing through the integrated platform (Fig. 18c). We obtained 98.7% viable cells in outlet 1 (non-target cells). These cells passed only through the first stage-spiral extractor of the integrated platform. Cells in outlet 2 (enriched target cells) were 90% viable having passed through the entire integrated platform (spiral extractor+ LCAT). Enrichment of a sub-population of cells that are morphologically different (size) from the rest of the cancer cell population, provides a unique sample set for further investigation into cancer progression and metastasis. Post enrichment, these cells can be grown to the required confluency in a 3D culture and then specific assays can be performed to determine the migration and invasion ability, along with self-renewability of the enriched cells. This information will potentially provide vital insight into development of tumor as well as regression in patients undergoing therapy.

In addition to cancer biology, size- based enrichment is particularly relevant to hematopoietic cells which are significantly heterogeneous in size. The monocyte

heterogeneity has been linked to macrophage lineage and differentiation into mature tissue osteoclasts and dendrite cells.[89,90,104,105] The classification of monocytes into classical, intermediate and non-classical has been dependent on expression of CD14 and CD 16.[89,90] Recent work has shown that there may be sub-populations of monocytes that differ in size, granularity, functionality and even nuclear morphology.[106] Furthermore, these sub-populations have not yet been fully characterized and the surface markers specific to each type have not yet been fully identified. For in depth investigation into how this differentiation is linked to the sub-populations of monocytes,[90,104,105] it is significant to be able to sort these sub-populations without any labeling. The integrated platform proposed in this work can sort and enrich a rare sub-population of monocytes. Since this method is label free (size being the only marker) the collected cells can be further characterized for differentiation patterns, granularity and functionality. Here, we have used our platform to enrich the extremely rare sub-population of larger monocytes (18μm+). We infused 10× diluted blood at the rate of 1.1mL/min into the integrated device and were able to successfully obtain an extremely pure, enriched sample containing only larger monocytes (Fig. 18d). The presence of monocytes in the outlet sample was confirmed by CD14 staining. Owing to the extreme rarity of larger monocytes (~2.2% of mononuclear cells),[89,104,105] it was difficult to determine the exact number of cells in the inlet sample. We estimated the enrichment of the target cells (large monocytes) with respect to non-target cells to be 987.6×. Fig. 18e shows the size comparison of the enriched sub-population of larger monocytes (as compared to the input blood sample and the non-target cells (RBCs and smaller WBCs) collected at outlet 1. The average size of the enriched sub-population of monocytes was 17.3 μm. For this application, we used human blood sample without any modifications to its

cellular composition. Therefore, exact recovery rate could not be calculated because initial monocyte percentage varies from sample to sample, so the initial concentration can't be determined. However, we are able to report the recovery rate of DU-145 cells and particle spiked blood as 67%. Furthermore, use of microstreaming for acoustic actuation instead of standing wave or cavitation, preserves cell physiology and functionality for further analysis of enriched cells.[107,68]

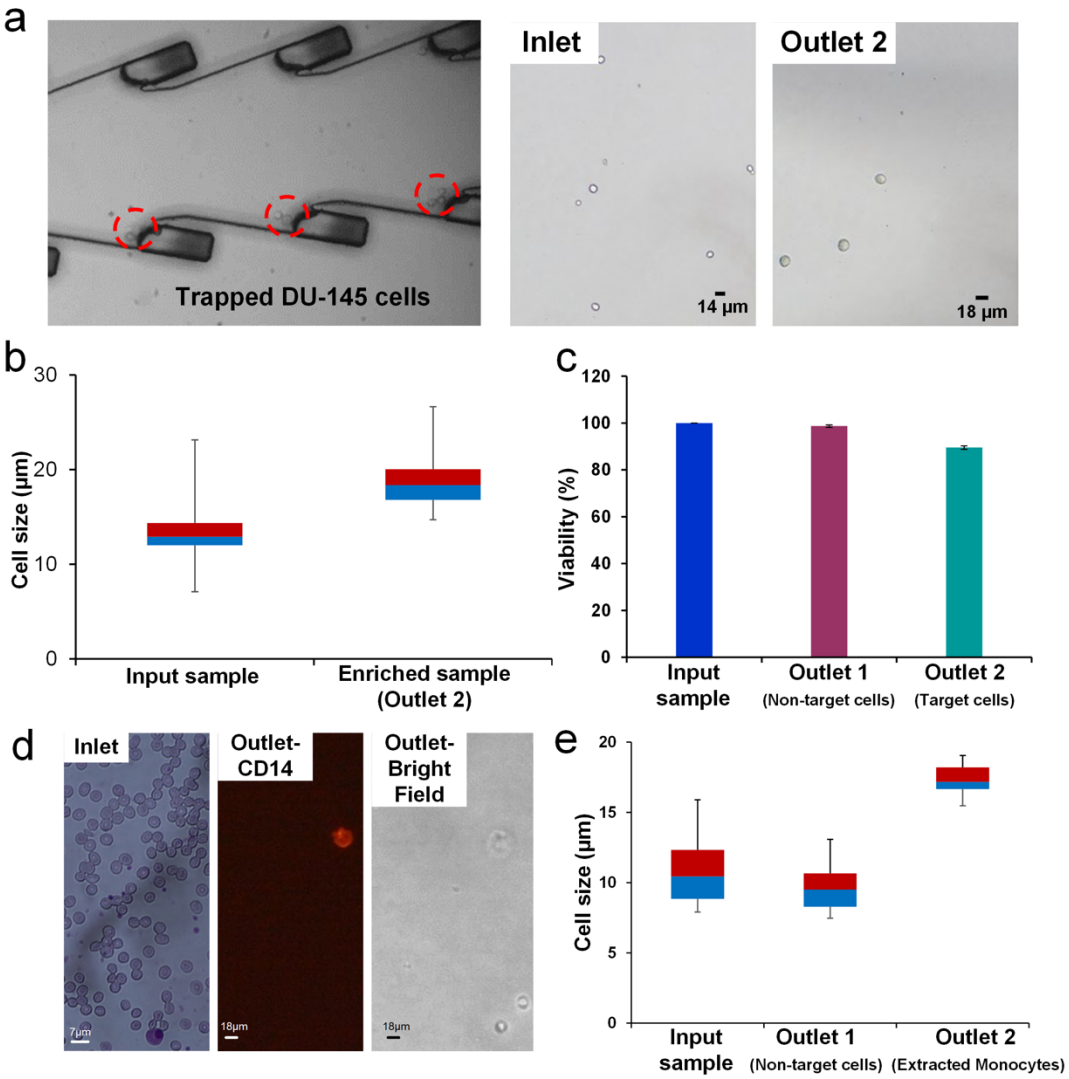

Figure 18: Integrated device used for two applications in cellular biology. (a) Bright-field image of the larger DU-145 cells trapped in the microvortices of the integrated device (left),

along with images showing the inlet sample and the sample at the outlet (right). (b) Box plot showing the range of cell-sizes of DU-145 cell sample at the inlet and the sample obtained after the enrichment using the integrated platform. The plot shows the enrichment of larger DU-145 cells in the outlet sample. (c) Plot showing the viability of DU-145 cells. We obtained 90% viability of enriched target cells. (d) Images showing the use of the integrated device for the isolation of a sub-population of monocytes. The Wright-Giemsa stained inlet sample shows a majority of RBCs with a few WBCs (left). The outlet sample obtained contained only monocytes, the presence of which was confirmed using the CD14 fluorescent antibody (middle). e) Box plot showing the size comparison of cells at the inlet (blood sample), outlet 1 (non-target cells) and extracted larger monocytes (target cells) from outlet 2.

The ability of the device to successfully enrich sub-population of DU-145 and larger monocytes at the high processing rate along with high purity of enriched sample, shows the potential versatility and utility of the platform. Further improvement on enrichment ratio and throughput will ensure that the device is comparable to current state of the art lab-on-chip enrichment devices.

2.4 Discussion and Conclusions

In this work, we have successfully demonstrated an integrated iMF+LCAT device for selective isolation and enrichment of cells from a heterogeneous mixture like cancer cell line and blood. Our integrated system combines passive and active microfluidic components for sample extraction and enrichment, despite the significant disparity in the operational flow rates of the two devices. Using this platform, we demonstrated successful removal (up to >90%) of smaller non-target cells (smaller DU-145 cells and RBCs and smaller WBCs) in

spiral iMF at the front end for minimum interference in the isolation of larger target cells. LCAT or the back end of the platform was used to trap larger (18+) cells with ~90% viability (Larger DU-145 cells and large monocytes).

The platform can enrich even the lowest of concentrations of spiked particles in blood (1 particle/mL) with high purity/enrichment ratio (44,000×). The overall throughput is controlled by the amount of sample processed by the entire platform, which is ~1mL/min (for bulk non-target cell extraction). Additionally, the enrichment of target cells in 50μL volume provides a highly concentrated sample of the target cell population. Using this platform, we were able to successfully enrich larger side-population of DU-145 cells with >91% purity. Additionally, we were able to isolate rare larger monocytes from 10× diluted blood with enrichment of 987×. In comparison with the current microfluidic devices that are limited by shear induced stress,[75] low throughput [61] or reliance on labeling,[61,62] our integrated platform offers label free and size-selective sample sorting and enrichment in a single pass. In fact, our approach dispenses with the need for pre-processing of input sample such as RBC lysing [45,59,52] for pre-processing of a blood sample prior to enrichment, thereby maintaining sample integrity.

Our integrated platform eliminates the trade-off between high purity and high throughput as experienced in previous size-based microfluidic devices. Furthermore, our approach offers a continuous, flow through, single step operation, unlike the multi-step devices such as the vortex isolator[92] that relies on a two-step process of trap and release with different flow rates. In future, we will be working on fine-tuning the size-selection criteria of the platform for higher enrichment. Overall, this work demonstrates a highly promising

approach to selective isolation and enrichment of particles/cells, and ultimately could lead to development of a single-step blood liquid-biopsy platform.[73]

Chapter 3

Disease Diagnosis in Integrated Microarray and Acoustic Microstreaming Platform

This chapter is adapted from the work "Neha Garg, Dylan Boyle, Arlo Randall, Andy Teng, Jozelyn Pablo, Xiaowu Liang, David Camerini*, Abraham P. Lee*. Rapid Immunodiagnostics of Multiple Viral Infections in an Acoustic Microstreaming Device with Serum and Saliva Samples. *Lab on a Chip*, 2019, 19, 1524-1533"

3.1 Introduction

In 2016, an estimated 36.7 million people were living with human immunodeficiency virus (HIV), including 1.8 million new cases and 1 million deaths worldwide.[108] More than 3.7 billion people under the age of 50 – or 67% of the population – are estimated to be

infected with herpes simplex virus type 1 (HSV-1), the primary cause of oral herpes, and 417 million people aged 15-49 years are estimated to be infected with HSV-2, the primary cause of genital herpes.[109] Human papilloma virus (HPV) infection is also very common with an estimated 11.7% prevalence worldwide or nearly 900 million infected people.[110] HIV, HSV and HPV can all be transmitted sexually as well as vertically.[12–14] Moreover, HPV and HSV can also be transmitted by more casual contact.[13,14]

Clinicians have observed that patients with one sexually transmitted disease (STD) are more likely to have another, either concomitantly or subsequently. Moreover, both HSV-1 and HSV-2, in immunocompromised people such as those with HIV, can have severe symptoms with more frequent outbreaks. Genital lesions by HSV-2 increase the risk of acquiring new HIV infections by approximately three fold.[19,20] In females, synergism between HIV and HPV have also been observed, and women who are HIV-seropositive have higher rates of HPV infection than women who are HIV-seronegative.[111] Higher rates of hysterectomy among HIV-infected women are persistent due to poor response to treatment and recurrent neoplasia.[112] However, with early and appropriate diagnosis, HPV related cervical cancer is a preventable disease. Therefore, we developed a novel multiplexed microfluidic device to diagnose multiple HIV, HSV and HPV antigen reactivity from serum and saliva samples within <20 minutes.

Standard laboratory methods for detection of HIV infection include nucleic acid based viral load assay as well as western blot, and enzyme linked immunosorbent assays (ELISA) for detection of anti-HIV antibodies.[113] Clinical diagnosis of HSV or HPV infection is confirmed by viral culture (cytological testing) and DNA detection in fluid from blisters and cervical lesions for the latter. Cytological testing has low sensitivity (45%), and poor

specificity as it is highly subjective to the interpretation of the cytologist.[114,115] On the other hand, standard nucleic acid based testing is expensive, time-consuming (>2 hours), and needs genomic amplification.[116] Bench-top western blot and ELISA take a long time (up to two days) due to inefficient mass transport for immune-agents to move from a solution to the surface, require trained personnel and utilize large sample volumes, which makes them unsuitable for use in resource limited areas.[117] With such a high prevalence of these viral infections, integrating and incorporating, rapid (<20 minutes), multiplexed, and low-cost diagnosis is desirable.

Recent advances in microfluidic technologies hold promise for the development of rapid, portable diagnostic tests for HIV, HPV and HSV.[118,119] Microfluidic devices for detection of infectious diseases generally use either nucleic acids or immunoassays based on antigen-antibody interactions for detecting viral load. Nucleic acid based microfluidic devices, however, require additional sample pre-treatment steps such as cell lysis, nucleic acid extraction and amplification which adds complexity.[120,121] Lateral flow immunoassays, on the other hand, use capillary forces for fluid actuation on paper based microfluidic devices [122,123], however, they generally have low sensitivity (μM-mM), are qualitative, rely on user interpretation and are unable to detect multiple targets at once.[124] Microfluidic devices for capturing and detecting intact HIV-1 using antibody conjugated quantum dots, magnetic beads, and photonic crystals [125–127] are promising but they suffer from added expense and typically more bulky instrumentation needs.

ELISA or western blot based microfluidic devices have been developed with chemiluminescent [128,129], fluorescent [130], plasmonic [131], or colorimetric [132] detection to measure the antibody concentration in bodily fluids. However, chemiluminescence,

fluorescence and plasmonic detection of antibodies require expensive instrumentation and are not suitable for resource-limited settings. Quantitative colorimetric detection which can rapidly generate the diagnosis will be vital. Recently, a microfluidic chip has been developed to capture antibodies against HIV-1 glycoprotein 41 and glycoprotein 36 using silver ions on gold for signal amplification.[133–135] Although, the optical detection was inexpensive and simple to use, the system was limited to detection of a handful of antigens. Here, we demonstrate a quick, portable, multiplexed immunoassay for detection of infection with three viruses simultaneously. Moreover, our assay utilized multiple antigens from each virus to increase both sensitivity (≤ 20 pM) and specificity.

Here we integrate a protein microarray printed on a nitrocellulose coated glass slide [19,136,137] with an acoustic microstreaming based microfluidic device to pump and mix the ELISA reagents.[65,138] The reagent flow is achieved with lateral cavity acoustic transducers (LCATs) and the mixing is achieved with vertical cavity acoustic transducers (VCATs). As explained in chapter 1, LCATs are the dead-end side channels arrayed in the X-Y plane while VCATs lead to the formation of the air pockets in the Z direction (normal to the plane) (Fig. 19a). An activated piezoelectric transducer (PZT) transmits acoustic energy to the air-liquid interfaces in both LCATs and VCATs, causing them to vibrate and produce streaming patterns in the nearby fluid. Net bulk fluid flow is generated by the LCAT vortices and fluid mixing is created in the direction perpendicular to fluid flow by two vortices in opposite directions due to the activity of VCATs. This transitions the biomolecular transport from diffusion dominated to convective, thereby reducing the detection time by more rapid antigen-antibody binding.[139] In this work, we show the diagnosis from serum samples of HIV, HPV, HSV positive patients and normal donors within 17.5 minutes in comparison with the

benchtop assay on the same microarrays which takes two hours up to overnight. We found antigens that showed significant reactivity for anti-HIV, anti-HPV and anti-HSV antibodies from serum samples; these are candidates for the diagnosis of these viral infections. To further demonstrate the device capability in a doctor's or dentist's office or where access to healthcare and phlebotomists is limited, we operate the device using saliva samples from HIV, HPV and HSV positive people. Overall, this work demonstrates a rapid and portable diagnostic platform for the detection of multiple biomarkers as a result of single or co-infection with HIV, HSV and HPV to monitor infections, reduce resistance and improve overall healthcare.

3.2 Assay Details

After priming, the microfluidic device was placed onto a piezoelectric transducer coated with ultrasound gel, subjected to a square wave at 49.8 kHz, 7 V_{pp} and sample (diluted 1:25) was added to the inlet port.[79] The sample was loaded continuously for five minutes and remaining sample was removed from the inlet. Blocking buffer was then pumped for one minute to remove unbound antibodies from the pad. Next, 25 μL of alkaline phosphatase conjugated goat anti-human IgG or goat anti-human IgA was added and pumped for five minutes. After a second wash with blocking buffer for one minute to remove unbound secondary antibodies, 25 μL of substrate (NBT/BCIP) was pumped and incubated for 3.5 minutes to generate the colored product on antibody-bound antigen spots. The pad was then washed with blocking buffer and DI water (one minute each) to remove excess substrate and prevent color intensity saturation. The pad was finally dried at room temperature after de-laminating the PDMS device and imaged using a USB microscope (Koolertron). All experiments were performed in accordance with the Institutional Biosafety Committee

Guidelines (protocol number: 2011-1383) and approved by the Institutional Review Board (Study number: 2012-8675) at University of California Irvine. Study participants were fully informed regarding the purposes of the study and consent was obtained.

3.3 Results

We previously utilized acoustic microstreaming to demonstrate pumping, mixing, sorting and enrichment of target cells/particles from complex biofluids such as blood.[73,140,141] For the present study, fluid pumping was accomplished by 100 μm wide LCATs arranged at a 15° angle to the main channel (500 μm) and spaced 350 μm that were designed and fabricated (Fig. 19a). For fluid mixing, VCATs with 100 μm diameter and spacing, oriented at 90° relative to the main fluid channel were aligned on the top wall of the microarray assay chambers (Fig. 19a). These dead-end side channels trap air and generate air-liquid interfaces when primed with an aqueous solution. The vibration of these air-liquid interfaces by a PZT cause first-order periodic flow in the liquid phase. This induces a steady second-order flow within the boundary layer and the slip condition then drives the steady streaming in the bulk of the fluid. The cavities at 15° generate a net force parallel to the flow direction. However, at 90°, two equal and opposite force components parallel to the flow direction cancel each other and the perpendicular component recirculates the fluid in the vertical direction, thereby causing mixing. Fig. 19b shows the molded PDMS microfluidic device bonded to a glass slide with eight nitrocellulose pads bonded to it which can aid in running eight patient samples in parallel.

3.3.1 Analysis of HSV, HIV and HPV positive serum samples

We printed a 12 by 13 array (pitch: 300μm) of immune-reactive HIV, HPV and HSV proteins on nitrocellulose pads bonded to microscope slides. The layout of the spotted antigens is shown in Fig. 19c. Each spot was printed with ~20 ng total protein (~0.4 ng protein of interest). We first analyzed the reactivity of pooled purified anti-HIV-IgG from the NIH AIDS Reagent Program and then five serum samples each from HIV+, HIV and HPV double+ and HSV+ individuals as well as five HIV, HPV and HSV triple negative samples using the assay demonstrated before. HIV-Ig and secondary antibody (AP conjugated goat anti-human IgG) were diluted at 1:50 and utilized for sample incubation time optimization from 1 minute to 5 minutes. We observed the maximum normalized intensity at 5 minute sample incubation as shown in Fig. 19d and to reduce the noise level (intensity of negative control spots) and reduce the total assay time, we decided to incubate the antibody samples for 5 min. Subsequently, patient sera and secondary antibodies were diluted 1:25 in blocking buffer with 20% and 2% *E. coli* lysate, respectively and substrate incubation was optimized to 3.5 minutes after analyzing the HIV-Ig positive signal to blank signal intensity ratio. Serum samples were then tested for reactivity with the antigen spots using the 17.5minute assay. After quantification using ImageJ, the spotted pads (Fig. 20a (i)-(iv) for triple negative, HSV+, HIV+ as well as HIV and HPV double + samples respectively) were analyzed using R software and the heatmap is shown in Fig. 20b.

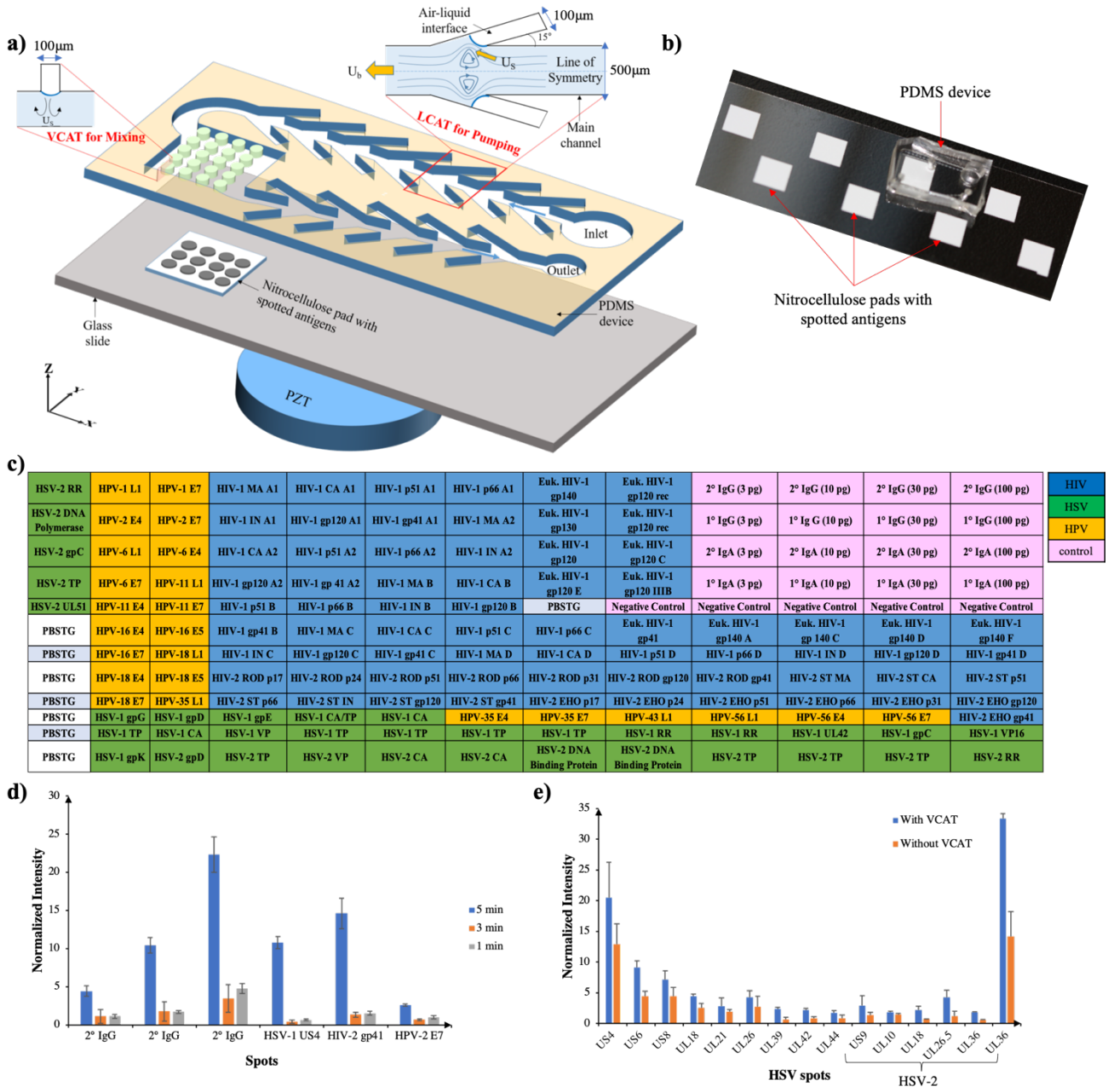

HSV-2 RR	HPV-1 L1	HPV-1 E7	HIV-1 MA A1	HIV-1 CA A1	HIV-1 p51 A1	HIV-1 p66 A1	Euk. HIV-1 gp140	Euk. HIV-1 gp120 rec	2° IgG (3 pg)	2° IgG (10 pg)	2° IgG (30 pg)	2° IgG (100 pg)	HIV
HSV-2 DNA Polymerase	HPV-2 E4	HPV-2 E7	HIV-1 IN A1	HIV-1 gp120 A1	HIV-1 gp41 A1	HIV-1 MA A2	Euk. HIV-1 gp130	Euk. HIV-1 gp120 rec	1° IgG (3 pg)	1° Ig G (10 pg)	1° IgG (30 pg)	1° IgG (100 pg)	HSV
HSV-2 gpC	HPV-6 L1	HPV-6 E4	HIV-1 CA A2	HIV-1 p51 A2	HIV-1 p66 A2	HIV-1 IN A2	Euk. HIV-1 gp120	Euk. HIV-1 gp120 C	2° IgA (3 pg)	2° IgA (10 pg)	2° IgA (30 pg)	2° IgA (100 pg)	HPV
HSV-2 TP	HPV-6 E7	HPV-11 L1	HIV-1 gp120 A2	HIV-1 gp 41 A2	HIV-1 MA B	HIV-1 CA B	Euk. HIV-1 gp120 E	Euk. HIV-1 gp120 IIIB	1° IgA (3 pg)	1° IgA (10 pg)	1° IgA (30 pg)	1° IgA (100 pg)	control
HSV-2 UL51	HPV-11 E4	HPV-11 E7	HIV-1 p51 B	HIV-1 p66 B	HIV-1 IN B	HIV-1 gp120 B	PBSTG	Negative Control	Negative Control	Negative Control	Negative Control	Negative Control	Negative Control
PBSTG	HPV-16 E4	HPV-16 E5	HIV-1 gp41 B	HIV-1 MA C	HIV-1 CA C	HIV-1 p51 C	HIV-1 p66 C	Euk. HIV-1 gp41	Euk. HIV-1 gp140 A	Euk. HIV-1 gp 140 C	Euk. HIV-1 gp140 D	Euk. HIV-1 gp140 F	
PBSTG	HPV-16 E7	HPV-18 L1	HIV-1 IN C	HIV-1 gp120 C	HIV-1 gp41 C	HIV-1 MA D	HIV-1 CA D	HIV-1 p51 D	HIV-1 p66 D	HIV-1 IN D	HIV-1 gp120 D	HIV-1 gp41 D	
PBSTG	HPV-18 E4	HPV-18 E5	HIV-2 ROD p17	HIV-2 ROD p24	HIV-2 ROD p51	HIV-2 ROD p66	HIV-2 ROD p31	HIV-2 ROD gp120	HIV-2 ROD gp41	HIV-2 ST MA	HIV-2 ST CA	HIV-2 ST p51	
PBSTG	HPV-18 E7	HPV-35 L1	HIV-2 ST p66	HIV-2 ST IN	HIV-2 ST gp120	HIV-2 ST gp41	HIV-2 EHO p17	HIV-2 EHO p24	HIV-2 EHO p51	HIV-2 EHO p66	HIV-2 EHO p31	HIV-2 EHO gp120	
PBSTG	HSV-1 gpG	HSV-1 gpD	HSV-1 gpE	HSV-1 CA/TP	HSV-1 CA	HPV-35 E4	HPV-35 E7	HPV-43 L1	HPV-56 L1	HPV-56 E4	HPV-56 E7	HIV-2 EHO gp41	
PBSTG	HSV-1 TP	HSV-1 CA	HSV-1 VP	HSV-1 TP	HSV-1 TP	HSV-1 TP	HSV-1 TP	HSV-1 RR	HSV-1 RR	HSV-1 UL42	HSV-1 gpC	HSV-1 VP16	
PBSTG	HSV-1 gpK	HSV-2 gpD	HSV-2 TP	HSV-2 VP	HSV-2 CA	HSV-2 CA	HSV-2 DNA Binding Protein	HSV-2 DNA Binding Protein	HSV-2 TP	HSV-2 TP	HSV-2 TP	HSV-2 RR	

Figure 19: Schematic and layout of an integrated microfluidic device for multiplexed detection of viral infection. (a) Device schematic showing LCATs and VCATs for pumping and mixing of patient sample containing antibodies aligned on the nitrocellulose pad respectively. (b) PDMS device bonded on the top of the nitrocellulose pad, ready for use. (c) Layout of HSV, HIV and HPV antigens produced by IVTT and HIV antigens produced in eukaryotic cells as well as primary and secondary IgG and IgA along with negative controls.

(d) Plot of normalized spot intensity for reactivity against various spots at different sample incubation times. e) Plot of normalized intensity for reactivity against HSV+ spots for devices with and without VCAT mixers

We used the rapid microfluidic assay we developed to test the reactivity of HSV+ sera with HSV antigens on the array. We found significant reactivity, compared to negative control sera, with nine antigens having ~4x intensity differences ($p<<0.05$) (Fig. 21a). Seven of these are HSV-1 proteins including glycoproteins G (US4), E (US8), D (US6), and C (UL42), viral capsid proteins encoded by genes UL26, UL18 and UL26.5 and tegument protein UL21. Furthermore, virion membrane glycoprotein D (US6) and tegument protein US9 showed significant positive reactivity among HSV-2 antigens. In addition, we assessed the importance of VCATs for mixing by analyzing the HSV+ sera in an LCAT-only device. As shown in Fig. 19e, we observed higher signal-to-noise ratio of the antibodies with spotted antigens when VCATs were utilized for mixing. This is due to efficient fluid displacement, especially during washing of non-specific antibodies, which resulted in lower intensity (noise) of negative controls.

Similarly, Fig. 21b (i) shows the top ten HIV antigens produced by IVTT that were found to be most significantly reactive with HIV+ sera compared to the reactivity of negative sera ($p<10^{-4}$). These antigens represent HIV-1 group M viruses, clades B, D and A2 which are responsible for a large part of the global AIDS pandemic. In addition to HIV-1 subtypes, the HIV+ patient samples also showed positive reactivity with HIV-2 antigens from both major groups, A and B. Furthermore, we compared the reactivity of the HIV+ and negative sera with purified HIV glycoproteins produced in eukaryotic cells. We found ten HIV glycoproteins that had $\geq$5x intensity differences and were statistically significant with $p <<0.05$ (Fig. 21b (ii)).

These antigens were derived from HIV-1 clades A-F, which together comprise more than 90% of the worldwide AIDS pandemic. The HIV+ sera also showed significant reactivity with HSV-1 glycoprotein G (US4) with ~2x intensity and p <0.05 which might be due to HSV-1 infection.

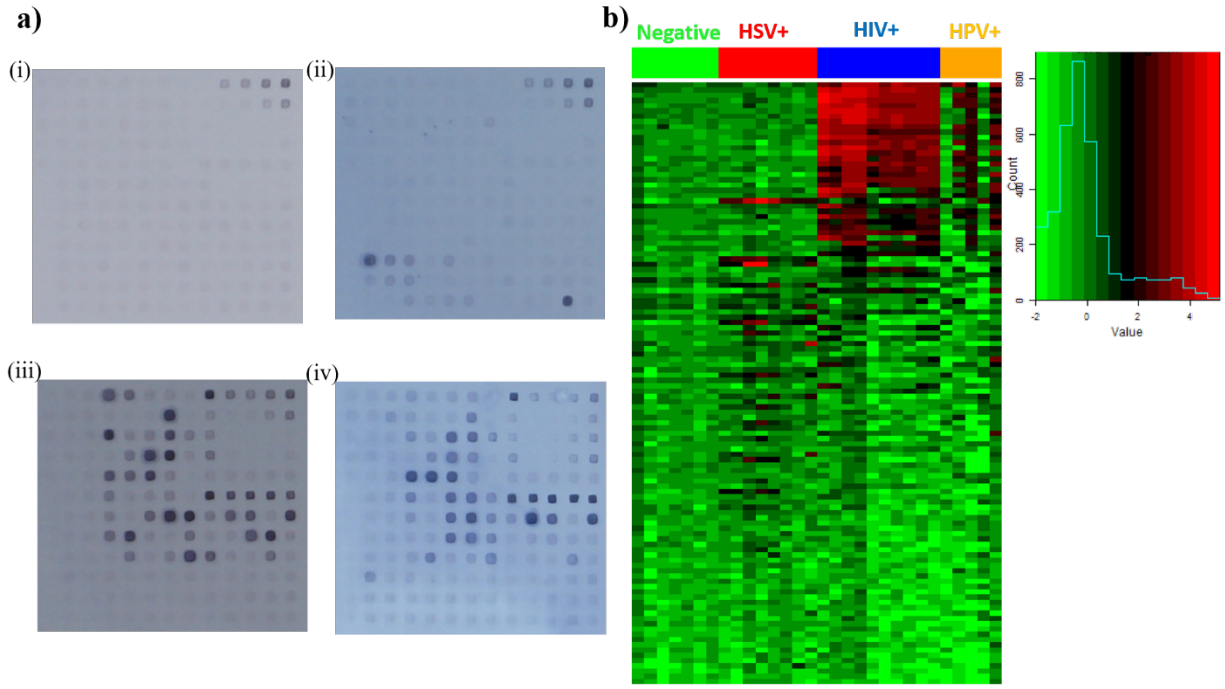

Figure 20: Serum antibody reactivity with HSV, HIV and HPV proteins on microarray. (a) Microarrays following 17.5 minute assay with (i) triple negative donor sera (n=4 patient samples, two repeats), (ii) HSV+ donor sera (n=4 patient samples, two repeats), (iii) HIV+ donor sera (n=5 patient samples, two repeats), and (iv) HIV+, HPV+ sera (n=5 patient samples). (b) Heat map of serum antibody reactivity with the color histogram on right indicating the spot intensity on a log base 2 scale.

HIV-infected individuals have higher levels of HPV seropositivity, with an increased frequency of infection with multiple HPV types simultaneously compared to HIV negative people. Therefore, we analyzed HIV+ sera which were reactive with HPV antigens and compared their reactivity with that of triple-virus negative samples. To increase the signal

intensity, we added AP conjugated goat anti-human IgA antibodies along with goat anti-human IgG secondary antibodies at 1:25 dilution for this assay only. HPV reactivity was weaker than HIV or HSV reactivity, but we observed near-significant reactivity with three HPV antigens: HPV-1 E7, HPV-2 E7 ($p < 0.1$), and HPV-16 E5, with ~2x intensity in comparison to the negative spots as shown in Fig. 21c. In addition, we observed significant reactivity (~2x intensity, $p<0.05$) of these patient samples with HSV-1 antigens glycoprotein G (US4), and capsid protein (UL26). HSV-2 antigens such as DNA polymerase subunit (UL42) and trans-activator tegument protein of early genes (UL48) also demonstrated near significant positive reactivity with $p < 0.1$. This is likely due to HSV-1 and HSV-2 infection in one or more of these HIV-infected subjects.

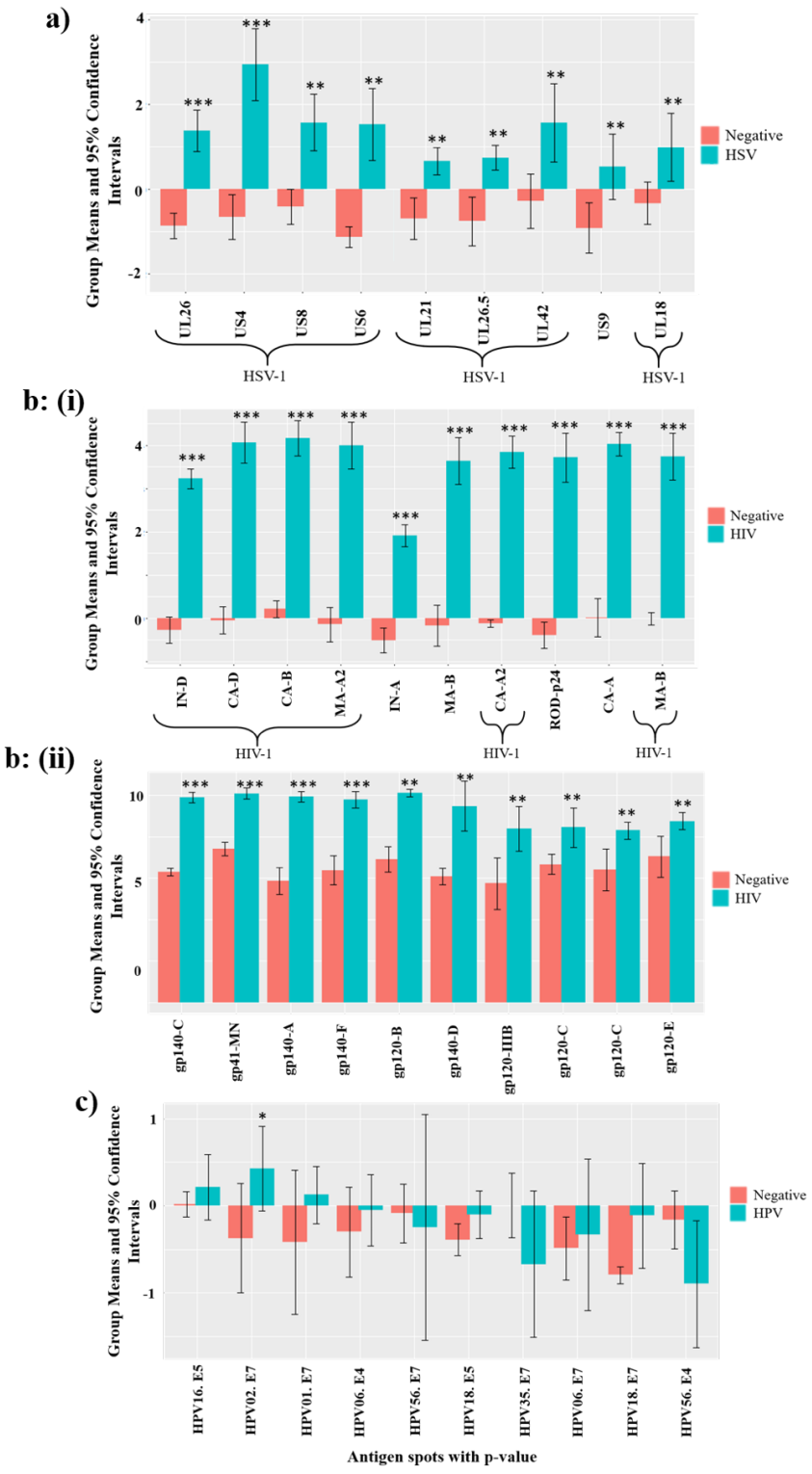

Figure 21: Most significantly reactive proteins with positive serum antibodies in comparison to triple negative serum samples. (a) reactivity of HSV+ serum samples with

HSV protein on the microarray. (b) (i) reactivity of HIV+ serum samples with HIV+ proteins produced by IVTT, (ii) reactivity of HIV+ serum samples with HIV+ proteins produced in eukaryotic cells. (c) reactivity of HIV and HPV dual positive serum samples with HPV IVTT proteins. *** Denotes significance with $p < 10^{-4}$, ** indicates significance for $p < 0.05$, * shows significance for $p<0.1$. Y-axis displays the average intensity of the spots with log base 2.

3.3.2 Analysis of HSV, HIV and HPV positive saliva samples

After demonstrating the device's potential using serum samples, we wanted to develop a diagnostic test which can utilize oral samples to minimize invasive sample collection. We tested saliva samples from four HIV+, four HIV and HSV double+, four HIV and HPV double+ and 4 triple negative individuals. Since, saliva has lower antibody titers, we reduced the dilution from 1:25 to 1:1 in blocking buffer (anti-IgG secondary antibody: 1:25) and used the same 17.5 minute assay. Images of the post-assay protein microarrays and a heat map of the reactivity (Fig. 22a and 22b) show reactivity of the positive saliva samples in comparison to triple negative samples.

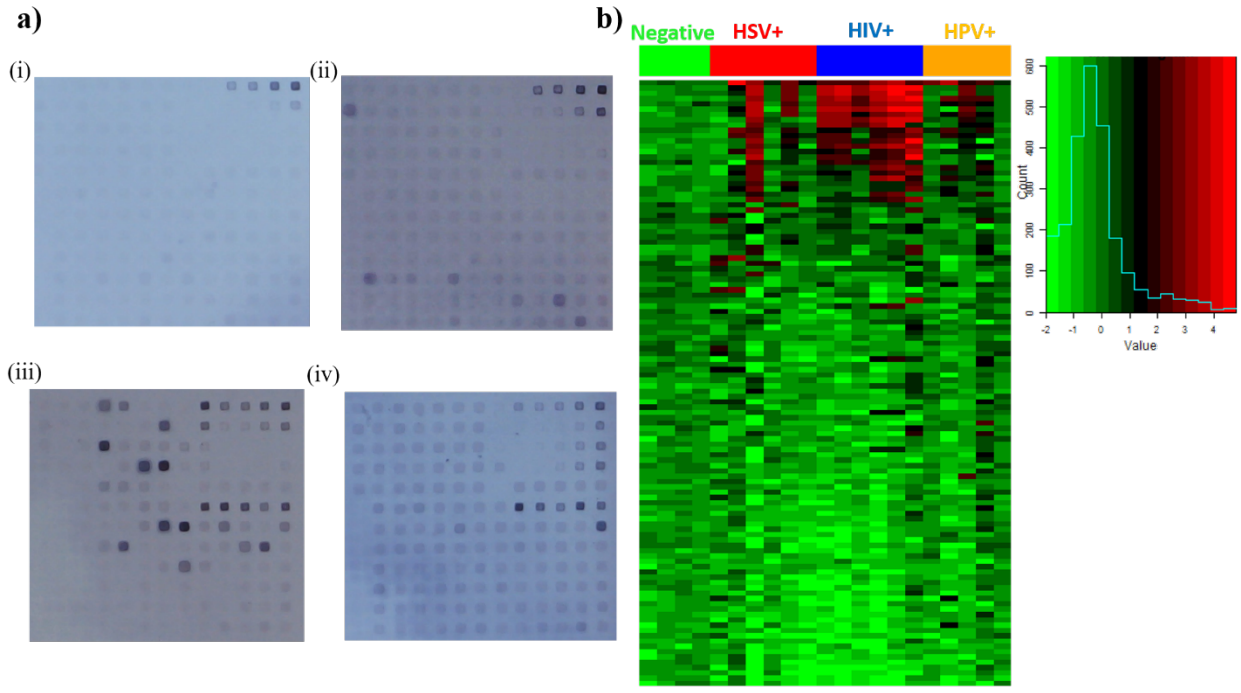

Figure 22: Saliva antibody reactivity with HSV, HIV and HPV proteins on microarray. (a) Microarrays following 17.5 minute assay with (i) triple negative donor saliva (n=4 patient samples), (ii) HIV+, HSV+ donor saliva (n=6 patient samples), (iii) HIV+ donor saliva (n=4 patient samples, two repeats), and (iv) HIV+, HPV+ saliva (n=5 patient samples). (b) Heat map of saliva antibody with the color histogram on right indicating intensity on a log base 2 scale.

HIV, HSV double+ saliva showed slightly greater reactivity in comparison to the triple negative saliva with HSV-1 glycoprotein G (US4) and (UL42) DNA polymerase subunit from HSV-1 and HSV-2 (Fig. 23a). The large error bars are due to the relatively weak signals and the small number of samples used.

After comparing the reactivity of HIV+ saliva samples to the reactivity of negative saliva samples, we ranked the most significantly reactive antigens based on the p-value.

These donors showed 6-30 fold intensity differences for reactivity with HIV-1 proteins produced by IVTT such as the transmembrane glycoprotein, gp41 from clade D, capsid protein, p24 from clades A2, B and D and matrix protein, p17 from clades A2 and B. The top nine most significantly reactive antigens from HIV-1 and HIV-2 are shown in Fig. 23b (i). Similar to HIV+ sera, the positive reactivity among HIV-1 antigens were from clades B, D and A2. The saliva samples also showed reactivity with HIV-2 matrix antigens from groups A and B. The HIV+ saliva samples demonstrated significant reactivity with seven glycoproteins produced in eukaryotic cells ($p<<0.05$); 6-30 fold more intense than in triple negative samples as shown in Fig. 23b (ii). HIV single positive saliva samples didn't present any significant HSV+ or HPV+ reactivity.

We then compared the HIV and HPV double positive saliva samples with triple negative saliva samples and similar to serum samples, we added AP conjugated anti-IgA antibodies to increase the signal intensity. As shown in Fig. 23c, HIV, HPV double + saliva showed significant and near significant reactivity (~2x intensity) with HPV-2 E7 ($p<0.05$), HPV-35 E7 ($p<0.1$), HPV-18 E5 ($p<0.1$), HPV-56 E4, HPV-56 E7, HPV-18 E7, and HPV-6 E4. In addition, we observed significant reactivity (~2x intensity) of these samples with HSV-1 tegument protein (UL21, $p<0.05$) and near significant reactivity with HSV-2 large tegument protein (UL36, $p<0.1$), HSV-1 glycoprotein G (US4), capsid protein (UL18), glycoprotein C (UL44), and virion protein VP16 (UL48). As for the HIV+, HPV+ serum samples, this likely resulted from HSV-1 and HSV-2 infection of one or more of the subjects.

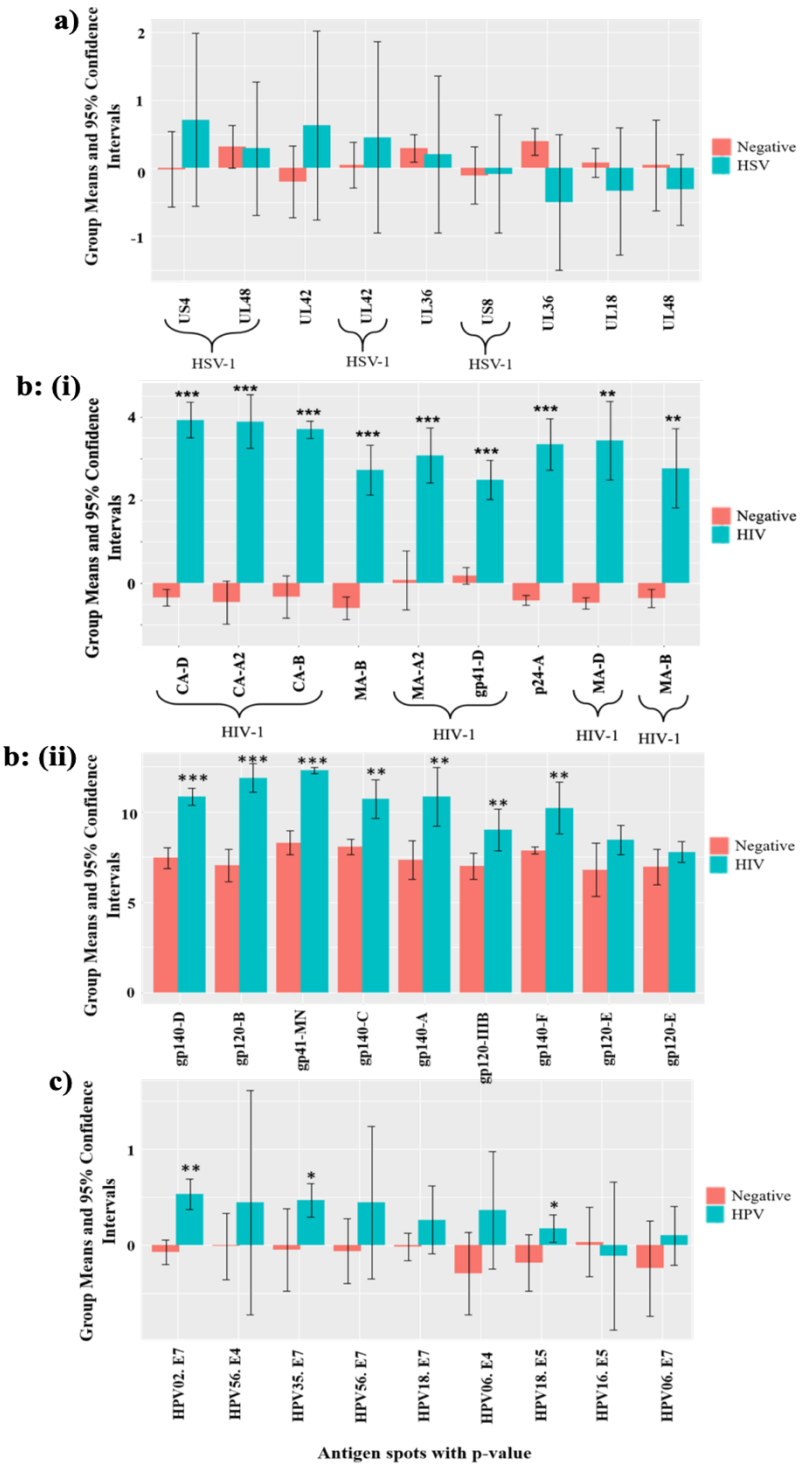

Figure 23: Most significantly reactive proteins with positive saliva sample antibodies in comparison to triple negative saliva samples. (a) reactivity of HSV+ saliva samples with HSV proteins on the microarray. (b) (i) reactivity of HIV+ saliva samples with HIV proteins

produced by IVTT. (ii) reactivity of HIV+ saliva samples with HIV proteins produced in eukaryotic cells. (c) reactivity of HIV and HPV dual positive saliva samples with HPV IVTT proteins. *** Denotes significance with $p < 10^{-4}$, ** indicates significance for $p < 0.05$, * shows significance for $p<0.1$. Y-axis displays the average intensity of the spots with log base 2.

3.4 Discussion

Currently, the diagnosis and treatment of viral infections with HIV, HPV and HSV is based on a handful of highly expressed biomarkers and each infection is diagnosed with different assays which causes delayed diagnoses and added expense.[141] Many co-infections by HPV and HSV in HIV infected people go undetected which then results in full blown infections and encompass huge epidemiological burden.[142] While a multiplexed HIV, HBV, HCV and syphilis screening is in development; the combined and simultaneous infections by HIV, HPV and HSV are at high-risk and needs continuous monitoring.[142] Although metagenomic shotgun sequencing is powerful in screening a broad range of viruses and detected both HPV and HSV (combined) in a dermal swab sample, it is limited due to longer assay times (72 hours) with high costs [143] and needs nucleic acid extraction and amplification. Bonito *et al.* utilized Luminex-based multiplexed platform and found the presence of both HPV-SD2 and HSV-1 in raw sewage samples.[144] Cao *et al.* utilized DNA microarray to simultaneously characterize pathogens including HSV and HPV with high sensitivity (10^2 – 10^3 copies), but the target genes were specific for single biomarker (glycoprotein B gene for HSV and L1 gene for HPV) and the hybridization process took ~1.5 hours.[145] In this work, we demonstrate for the first time a novel microfluidic platform capable of detecting multiple biomarkers as a result of single viral infection or co-infection with HIV (both HIV-1 and HIV-2), HSV (both HSV-1 and

HSV-2) and HPV (L1, E4, E7 for HPV-1, 2, 6, 11, 16, 18, 35, 56) within 17.5 minutes. This may be particularly relevant for HIV infected populations who often have other infections that interact with HIV and vice versa. For example, genital HSV infection increases the acquisition risk of HIV infection which leads to worsened clinical presentation of HSV infection due to the HIV induced immune-suppression. In addition, HIV-infected persons encompass a heavy burden of HPV-associated disease linked mostly to progressive immune suppression.[146] With the presented microfluidic device, we observed that HIV+ serum and saliva samples showed significant reactivity with both HSV (US4, UL26, UL21) and HPV (HPV-2 E7 and HPV-35 E7) antigens. Therefore, in order to avoid false negatives and achieve precise diagnosis, we demonstrate, for the first time, diagnosis of all three pathogens within 17.5 minutes, necessitating the importance of a multiplexed assay. On the other hand, we observed varied reactivity of US4 in both HSV+ serum and saliva samples which can lead to test ambiguities and incomplete diagnosis. In order to minimize these risks and provide improved diagnosis of HSV infection, we identified multiple antigens such as capsid proteins (UL26, UL26.5, UL18), glycoprotein E (US8), tegument protein (UL21, US9), and DNA polymerase processivity factor (UL42), that are characteristic of antibodies produced during HSV (type 1 and type 2) infection. Therefore, contrary to the tests based on single antigens for diagnosing HIV and HSV [147], this technology will be able to provide clear, distinct antigens or antigen sets for serodiagnostic biomarker, vaccine, and therapeutic product development.

Although significant reactivity was obtained with serum samples, its sample preparation is time consuming and needs phlebotomists to draw blood. Therefore, to develop a diagnostic test for large scale detection at community health centers and dental clinics, we validated our platform with saliva samples. This is particularly important while handling of

pediatric and geriatric patients in order to reduce the number of blood draws or when access to healthcare is limited in remote locations where phlebotomists are unavailable [148]. Although, antibody detection for HIV from oral fluids has been developed, its dependence on single antigen (p24) might lead to false negatives. In addition, both HPV and HSV from saliva samples were detected with antibodies specific to secretory IgA by nephelometry and ELISA, respectively, which takes time and lacks specificity. In this work, with saliva samples, we obtained significant reactivity of multiple proteins from all three viruses, HIV, HSV and HPV similar to serum samples. Although antibody titers in saliva are generally low, we obtained six common antigens from serum and saliva samples which belongs to both HIV-1 (CA-B, CA-D, MA-A2, CA-A2, MA-B) and HIV-2 (MA-B, p24) and can be utilized as antigen sets for HIV diagnosis. While saliva reactivity was not found to be significant for HSV, US4 and UL42 from HSV-1 showed positive reactivity in both serum and saliva samples. HPV-2 E7 was common between HPV+ serum and saliva samples but due to asymptomatic nature of both HSV and HPV infections and sample preparations, it seems more appropriate to utilize serum samples for HSV and HPV diagnosis. Therefore, this device can also be used at the point-of-care in doctor's or dentist's office to screen for infections that affect care, using saliva samples. For example, HPV has been implicated in oropharyngeal cancer and identifying its symptoms via oral or dental examinations (saliva) may be the key to early detection and diagnosis. In addition, an oral test for detection of antibodies will allow large-scale population testing at community health centers, STD clinics and dental settings, thereby reducing the number of deaths worldwide.[148]

Overall, this work demonstrates a highly promising approach for identification, analysis, and monitoring of antibodies to specific antigens or antigen sets as a result of single or

multiple infections. This technology, based on acoustic microstreaming, assesses the reactivity of serum and saliva samples with the spotted antigens in less than twenty minutes. We observed diverse antibody responses and significant positive reactivity with multiple antigens from each virus. Hence this platform enables simultaneous screening of multiple antigens from various infections in different samples at reduced cost and time which are especially relevant for use in resource limited settings.

3.5 Conclusions

An acoustic microstreaming based LCAT-VCAT device that can assess the reactivity of antibodies from both serum and saliva samples to detect multiple infections is reported. Within 17.5 minutes of operation, diverse antibody responses and significant positive reactivity with multiple antigens from HSV, HIV and HPV to prevent false negatives is demonstrated. This study validates the use of integrated high-throughput microarray to show significant cross-reactivity between HSV and HIV infected serum samples, HSV and HIV-HPV dual positive serum and saliva samples. Finally, colorimetry-based analysis applied in the present work enables easy on-site testing which is suitable for point-of-care diagnosis.[149]

Chapter 4

Summary and Future Directions

4.1 Summary

Individual cellular and sub-cellular populations from unprocessed blood carry plethora of information about the proper functioning of all tissues and organs in the body. This makes its separation and analysis of prime interest for both medical and scientific applications while playing an important role in disease diagnosis and prognosis. However, to adequately understand the information provided from its subsets, it requires efficient technologies. Currently, blood is separated into different components by density-based centrifugation methods using ficoll histopaque which is labor intensive, expensive and does not allow for high-resolution sorting of blood. Although antibody-based approaches such as fluorescence activated cell sorting (FACS) or magnetic-activated cell sorter (MACS) are available commercially, they are time-consuming, expensive and does not process whole blood.

Lab-on-chip systems have been developed as efficient and powerful approaches for high-throughput blood separation (both cellular and sub-cellular components), owing to

their precise control of fluid behavior, utilize small sample volumes and achieve continuous molecular and functional analysis down to single-cell level. In the research presented here, we developed lateral cavity acoustic transducers (LCATs) as simple geometric features that utilize an array of acoustically actuated air-liquid interfaces to generate acoustic microstreaming flows and manipulate cells/particles. In addition, when these are oriented at an angle, they create a net bulk flow from inlet to outlet.

In this dissertation, we first demonstrated the LCATs capability to utilize whole blood and sort different cellular components (platelets, RBCs and WBCs) owing to their difference in size. Further, we extended its application to sort and enrich rare cells such as CTCs or cancer-associated fibroblasts from whole blood and characterized them on chip using *in situ* immunolabeling. Although we achieved highly efficient trapping (>99%) and enrichment (~200x) of these rare cells at 10/ml spiking concentrations in whole blood, rare cells can exist at concentrations as low as 1 per 7.5 ml of whole blood. And for that, we integrated the active LCAT device with a high throughput, passive spiral iMF microfluidic device and demonstrated the selective sorting and enrichment of side populations from tissue biopsy and blood.

Following that, due to the existence of numerous sub-cellular components such as antibodies in blood, we showed the diagnosis of three infectious diseases (HIV, HPV and HSV) simultaneously using an LCAT-VCAT (Vertical cavity acoustic transducers) device integrated with proteomic microarray. In addition, to demonstrate the device's potential as a point-of-care device, in limited resource settings or where phlebotomists are unavailable, we validated the device with saliva samples containing antibodies for HIV, HPV and HSV and demonstrated significant positive reactivity within 17.5 minutes. To the author's knowledge,

this is the first demonstration of a multi-functional device which can not only process whole, unprocessed blood for sorting and enrichment of cellular populations, but also utilize sub-cellular populations for rapid and multiplexed disease diagnosis.

4.2 Plasma Extraction

With rising healthcare costs, lack of highly trained personnel, and the trend to bring healthcare closer to the patient, easy-to-use, low complexity healthcare solutions, that allow for rapid, low cost preparation of whole blood samples is critical for effective point-of-care (POC) diagnostics.[150] Consolidation of core labs as a reaction to high price pressure and increasing throughput are driving the need for faster time to result, error-minimized sample preparation and robust automation of the diagnostic process. The efficient separation of plasma/serum from whole blood is an important step to prevent blood components (both cellular and sub-cellular) from interfering with assay analyses downstream. In the absence of an automated and sensitive blood-plasma separation method, extra washing steps are required, thus, increasing complexity, more complicated automation and longer sample-to-answer times.

Current methods to achieve plasma/serum separation are manual and laborious, often requiring mixing by hand, centrifugation, and final manual transfer of serum/plasma to a fresh tube.[151] As with any manual process, these steps are subject to human error. Centrifuging can damage blood cells resulting in loss of sample integrity,[152] and the entire time-consuming process contains inherent variability due to inconsistencies in manual handling between technicians. Some methods include a porous membrane to trap blood cells and allow blood plasma to flow through.[153,154] Others have fabricated comb and weir-type filter structures and reported a cross-flow based microfluidic devices for continuous plasma separation. However, both weir-based and membrane-based devices suffer from utilization of whole blood, complex fabrication of small pore sized filters, RBCs contamination and

clogging.[155] Still others may use hemolysis reagents to lyse various blood cells, leaving the blood plasma and cellular contents in suspension.

Other microfluidic research groups have also made important innovations to separate blood components. Son *et al.* achieve hemolysis free blood separation by integrating a porous membrane into a microfluidic flow channel.[156] Another example includes Zhang *et al.*, who used gravitational sedimentation and bifurcation in a laminar flow channel to delaminate blood cells from blood plasma, creating a continuous flow of blood plasma that can run for up to four hours.[157] Finally, Yang *et al*. separated blood based on the Zweifach-Fung effect in a microfluidic device.[158] Although successful plasma separation was demonstrated, these technologies suffered from low-throughput and could not process whole blood.

A chip design capable of processing a whole blood sample with no previous preparation is desired. Due to LCAT's capability of pumping and successful operation with whole blood, we decelerated the cellular components such as platelets, RBCs and WBCs by trapping in the vortices. During the process, the fluidic component of blood, plasma, travelled with the device's bulk velocity causing it to separate and flow dominantly. Once the whole unprocessed blood was poured in the inlet of the device, plasma was separated through the and pulled by the end user. For the extraction, we started with the current device primed with 1x PBS buffer, and extracted 80µl of the plasma by running multiple devices. To analyze the quality and compare with the current gold standard (centrifuged), we utilized Beckman Coulter AU Analyzer for glucose concentration. However, we obtained only 2mg/dl glucose concentration in comparison to 77mg/dl in centrifuged plasma as shown in Fig. 24a (patient 1) which is due to the presence of PBS buffer while forming the air-liquid interfaces, leading

to ~33x dilution. Following that, we reduced the PBS priming and utilized LCAT's oqn capability of pumping whole blood to form air-liquid interfaces. We primed the first 4 rows of LCAT and started the PZT actuation. As a result, we extracted 40μL (3μL of plasma from 30μL whole blood per device) and obtained similar glucose concentration (Patient 2, Fig. 24a) compared to centrifuged plasma. We then moved one step further and analyzed the extracted sample for wider spectrum of analytes such as total protein (TP), alanine transferase (ALT), Vancomycin, and IgG in heparinized blood (compared to EDTA blood). We obtained similar concentrations of TP (Patient 3, Figure 24b), and ALT (Patient 3, Figure 24c). In order to increase the throughput, we scaled up the current device 4x by increasing the main channel width to 1mm (From 500μm) and height to 200μm (from 100μm) and utilized a chrome mask (in comparison to thin film transparency mask) to obtained high resolution features. We obtained ~12μl of plasma from 120μl of whole blood within 5min. After running 6 devices, we collected ~70μl of plasma to analyzed for glucose, total protein, and IgG in LCAT extracted plasma and centrifuged plasma. We obtained similar concentration of glucose (Patient 4, Figure 24a), TP (Patient 4, Figure 24b), and IgG (Patient 4, Figure 24d). We repeated the similar procedure with another blood sample and obtained similar concentration of glucose (Patient 5, Fig. 24a), TP (Patient 5, Fig. 24b) and Vancomycin (Patient 5, Fig. 24c) concentrations.

During the process, we also measured lactate dehydrogenase (LDH) concentration in LCAT extracted plasma and centrifuged plasma and obtained 240.9U/L in LCAT device vs 50U/L in centrifuged plasma. This is due to sensitivity of LDH assay with hemoglobin and hemolysis in the plasma extracted by LCAT.

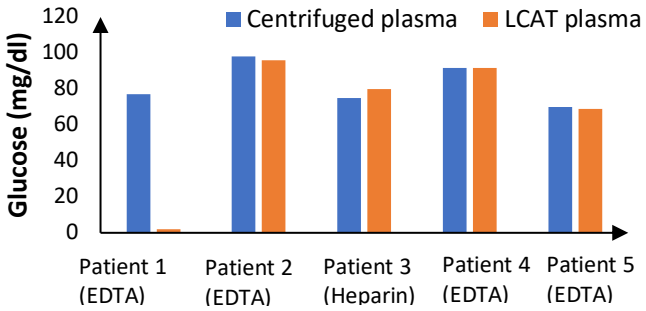
Centrifuged plasma
LCAT plasma
Glucose (mg/dl)
120
100
80
60
40
20
0
Patient 1 (EDTA)
Patient 2 (EDTA)
Patient 3 (Heparin)
Patient 4 (EDTA)
Patient 5 (EDTA)

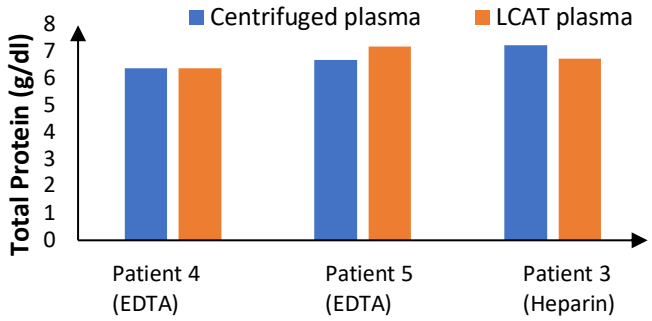
Centrifuged plasma
LCAT plasma
Total Protein (g/dl)
8
7
6
5
4
3
2
1
0
Patient 4 (EDTA)
Patient 5 (EDTA)
Patient 3 (Heparin)

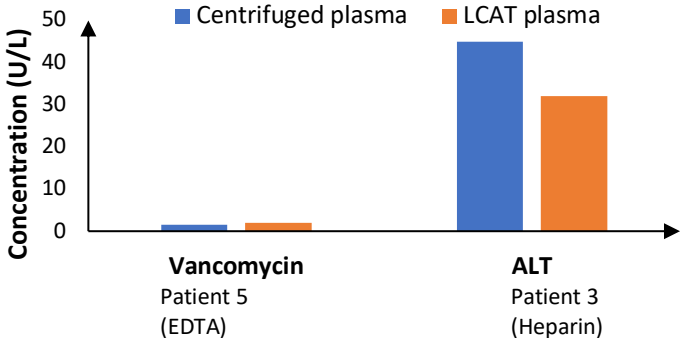
Centrifuged plasma
LCAT plasma
Concentration (U/L)
50
40
30
20
10
0
Vancomycin
Patient 5 (EDTA)
ALT
Patient 3 (Heparin)

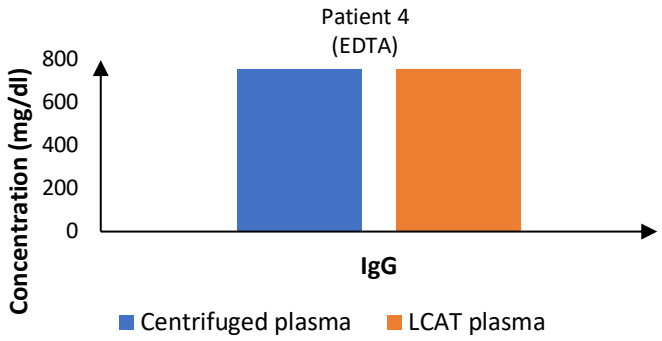
Patient 4 (EDTA)
Concentration (mg/dl)
800
600
400
200
0
IgG
Centrifuged plasma
LCAT plasma

Figure 24**:** Comparison of various analytes (a) Glucose, (b) Total protein (TP), (c) Vancomycin and Alanine Transferase (ALT), (d) IgG measured in LCAT extracted plasma with centrifuged plasma.

Although the device is very promising in comparison to other technologies, several points need to be addressed in future such as:

- Hemolysis
- Improvement in extraction efficiency from 10% (with respect to whole blood) within <10min
- High-throughput fabrication
- process clinical sample with high protein or lipid content

4.3 OSTE based LCAT Device Fabrication

Many academic researchers around the world are developing unique and innovative microfluidic devices, but most of the field still relies on the polydimethylsiloxane polymer (PDMS) as a standard.[159] Although the polymer is cost and time effective for small prototype batches, the material is difficult to transfer to large scale industrial methods.[160] Consequently, the microfluidic field has a gap between research prototypes and proof-of-concept devices that are closer to a manufacturable product. Carlborg and van der Wijngaart *et al*. in 2011, showcased Off-Stoichiometry Thiol-Ene polymers (OSTE) as an alternative to PDMS, with potential to bridge the gap between academia and industry.[161] As described in their work, OSTE can form both soft and rigid parts, can be bonded in minutes under ultraviolet exposure (UV), and can be treated to create hydrophobic features. This Off-Stoichiometry Thiol-Ene polymer is created by mixing monomers with thiol functional groups, and monomers with allyl functional groups, in unequal parts so that there is an excess of one of the monomers. When the two are uniformly mixed and cured under UV light, the monomer with the lesser ratio completely polymerizes with its pairing component, and forms a solid polymer. However, an excess quantity of the other monomer still remains dispersed throughout the polymer. To differentiate between different mixtures, the authors used the terminology OSTE-Thiol (90) to represent a polymer in which 90 percent of the thiol groups are in excess, while OSTE-Allyl (30) has 30 percent of the allyl groups in excess. By changing the degree of off-stoichiometry, the resulting polymer can range from rigid in strength (1300 MPa Young's modulus) to pliable (down to 120 MPa Young's modulus). The best advantage of this polymer is the ability of the excess thiol or allyl groups to pair with each other under UV exposure; when one surface of excess thiol is brought into contact with

a surface of excess allyl, the two readily bond under UV. This "click" reaction allows easy bonding of device layers, and allows the device surfaces to be treated with chemicals functionalized with thiol or allyl groups.[162] In addition to the above, OSTE has many desirable features which can improve the functionality of microfluidic devices (Table 1).

Qualities Considered	**PDMS Polymer**	**OSTE Polymer**
Rigidity	Pliable, often requires a stiff carrier or mounting	Can be formulated to be pliable or rigid
Reactivity to Solvents	May dissolve in or swell in many organic solvents	Resistant to most organic solvents
Fabrication Time	Requires up to a day for curing of polymer and baking after plasma bonding	Devices can be polymerized and bonded in 2 to 3 UV step, 15 minutes or less each
Bonding Process	Requires plasma bonding	Performed more cheaply, using ultraviolet exposure
Alignment of Multiple Layers	After plasma treatment, layers must be aligned in under one minute, before bond strength is lost	Layers can be aligned freely before UV exposure
Permeability	Permeable to gases and some liquids	Not permeable to gases or liquids

Table 1: Comparison of OSTE fabricated devices with PDMS fabrication

To successfully fabricate the LCAT device with OSTE polymer, we changed the OSTE-Allyl stoichiometry from 30% excess allyl to 20% excess allyl, to improve polymerization. We created thin, flat layers of soft OSTE-Thiol (90) by spin coating, and we molded microfluidic channels in the stiff OSTE-Allyl (20), as shown in Figure 25b, respectively. To achieve a thin layer of OSTE-Thiol (90), we spun the polymer on a glass slide or glass cover slip using a Laurell Spin Coater (WS-650-23) at 400 rotations per minute for 10 seconds, then at 1,000 rotations per minute for 60 seconds. After the spin coating was finished, we

exposed the OSTE-Allyl (20) layer to UV light in a Jelight UVO Cleaner (model 342) for 15 minutes.

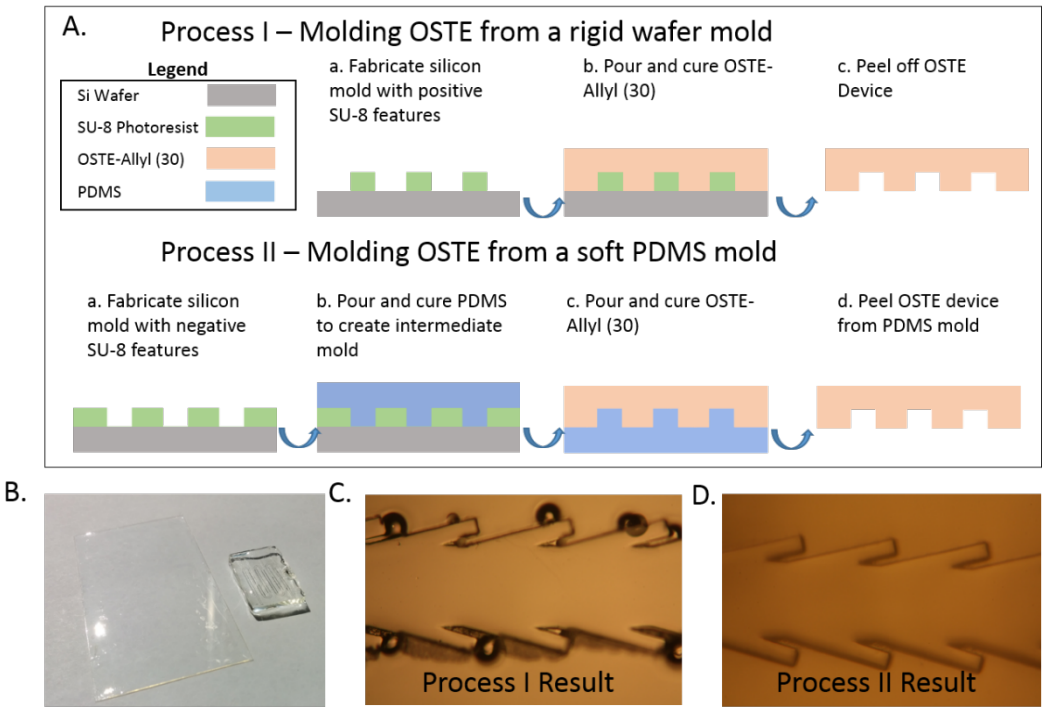

Figure 25: An overview of the fabrication process to make OSTE devices. (A) Shown here are two methods for producing OSTE-Allyl (20) chips; Process I use molding of OSTE directly from a silicon wafer, while Process II uses PDMS as the mold for OSTE. (B) Photograph of a glass cover slip with a coating of soft OSTE-Thiol (90), and an LCAT device made from stiff OSTE-Allyl (20). (C) A 10X magnification view of LCAT features created by Process I, which can cause unwanted bubbles and tearing of features. (D) A 10X view of the same chip created by Process II, showing features with higher detail and resolution

We molded microfluidic channels into the device by molding the stiff OSTE-Allyl (20) onto a silicon wafer with SU-8 photoresist patterns. Although we were able to achieve the fabrication using OSTE, the resolution was significantly low. As shown in Fig. 25c, when the cured OSTE-Allyl (20) was peeled from the mold, small microfluidic features would fracture

and break off from the device due to the polymer's brittle nature and the mold's non-flexible patterns. To improve the feature resolution, we decided to add an additional step to the molding process. Instead of molding the OSTE-Allyl (20) from a silicon mold, we fabricated flexible molds from polydimethylsiloxane (PDMS), allowing the flexible mold to be easily peeled from the stiff OSTE chip.

To create the flexible PDMS secondary mold, we first fabricated a silicon wafer with SU-8 patterns as a primary mold. To accommodate the correct mold features on the PDMS mold, we used an inverted UV mask to create inverted features on the silicon wafer. Figure 25A shows a comparison between direct molding of the OSTE from a silicon mold, versus molding of the OSTE from a PDMS mold. After the PDMS mold was cast from the wafer, we cut the PDMS into smaller sections, and wrapped the PDMS with Scotch tape to form a small area in which to pour the OSTE polymer. After pouring the OSTE, the polymer was cured under UV for 15 minutes. Once the OSTE was cured, the flexible PDMS can be easily peeled away from the OSTE chip under room temperature. Using this method, we created microfluidic channels with smaller features and with higher repeatability, as shown in Figure 25D. This improvement in feature resolution was especially important in fabricating the LCAT device, which requires well defined features to create vortices in the chip.

Hydrophobic Coating

After improving the feature quality in the OSTE devices, we set out to create chips with hydrophobic surfaces as detailed by Carlborg *et al*.[161] In order to make both materials (stiff OSTE-Allyl (20), soft OSTE-Thiol (90)), it is necessary to use a hydrophobic molecule with either a thiol group or an allyl group to properly match the excess groups in the OSTE polymer. As a result, we purchased Poly(vinylmethylsiloxane) (ABCR-GmBH AB109396) and

[2-3% (Mercaptopropyl)methylsiloxane]-dimethylsiloxane copolymer (ABCR-GmBH AB113727). Both of the substances are essentially hydrophobic PDMS particles, with Poly(vinylmethylsiloxane) having an exposed thiol group capable of bonding with OSTE-Allyl, and [2-3% (Mercaptopropyl)methylsiloxane]-dimethylsiloxane having an exposed allyl group capable of bonding with OSTE-Thiol. To create hydrophobic OSTE layers, we made dissolved solutions of each molecule by adding 10% weight by weight of the respective hydrophobic molecule and 0.5% weight by weight ITX photoinitiator (Sigma-Aldrich 406317-25) to a toluene solution. We submerged the OSTE-Thiol and OSTE-Allyl parts in the respective solution in a glass petri dish, and then exposed the parts to UV for 5 minutes. Once complete, we washed the parts with toluene, and dried them with compressed nitrogen gas.

	Reported Here		**Reported by Carlborg *et al*.**[161]	
	Untreated	Treated	Untreated	Treated
OSTE-Allyl (20/30)	32°	79°	68°	77°
OSTE-Thiol (90)	45°	83°	76°	97°

Table 2: Comparison of contact angles achieved by us and others

As a result of the treatment, we observed a significant improvement in the contact angles. However, further improvement is needed for successful operation of the LCAT device which strongly relies on the bubble formation on hydrophobic PDMS (contact angle: 105°). In addition, it is imperative that the air bubbles within the LCAT remain in a uniform shape which changes drastically within 20min. Although due to because gas impermeability of OSTE and its hard nature, the interfaces remained stable for 5hours, further optimization and device consistency need to be observed. Furthermore, the applications of particle

separation and pumping need further analysis in OSTE devices in order to utilize it as a gap-bridging alternative to PDMS.

Bibliography

1. Koumoutsakos, P., Pivkin, I. & Milde, F. The Fluid Mechanics of Cancer and Its Therapy. *Annual Review of Fluid Mechanics* **45**, 325–355 (2013).
2. Hanahan, D. & Weinberg, R. A. Hallmarks of Cancer: The Next Generation. *Cell* **144**, 646–674 (2011).
3. Subotic, S., Wyler, S. & Bachmann, A. Surgical Treatment of Localised Renal Cancer. *European Urology Supplements* **11**, 60–65 (2012).
4. Skliarenko, J. & Warde, P. Practical and clinical applications of radiation therapy. *Medicine* **44**, 15–19 (2016).
5. Corrie, P. G. Cytotoxic chemotherapy: clinical aspects. *Medicine* **36**, 24–28 (2008).
6. Masihi, K. N. Fighting infection using immunomodulatory agents. *Expert Opinion on Biological Therapy* **1**, 641–653 (2001).
7. Carlson, M. J., Thiel, K. W. & Leslie, K. K. Past, present, and future of hormonal therapy in recurrent endometrial cancer. *Int J Womens Health* **6**, 429–435 (2014).
8. Devriese, L. A. *et al.* Circulating tumor cell detection in advanced non-small cell lung cancer patients by multi-marker QPCR analysis. *Lung Cancer* **75**, 242–247 (2012).
9. Miller, M. C., Doyle, G. V. & Terstappen, L. W. M. M. Significance of Circulating Tumor Cells Detected by the CellSearch System in Patients with Metastatic Breast Colorectal and Prostate Cancer. *J Oncol* **2010**, (2010).
10. Kalluri, R. & Neilson, E. G. Epithelial-mesenchymal transition and its implications for fibrosis. *J Clin Invest* **112**, 1776–1784 (2003).
11. Kalluri, R. & Weinberg, R. A. The basics of epithelial-mesenchymal transition. *J Clin Invest* **119**, 1420–1428 (2009).
12. Seitz, R. Human Immunodeficiency Virus (HIV). *Transfus Med Hemother* **43**, 203–222 (2016).
13. Tasoglu, S. *et al.* Advances in Nanotechnology and Microfluidics for Human Papillomavirus Diagnostics. *Proceedings of the IEEE* **103**, 161–178 (2015).
14. Cowan, F. M. *et al.* Herpes simplex virus type 1 infection: a sexually transmitted infection of adolescence? *Sexually Transmitted Infections* **78**, 346–348 (2002).

15. Lifson, M. A. *et al.* Advances in biosensing strategies for HIV-1 detection, diagnosis, and therapeutic monitoring. *Advanced Drug Delivery Reviews* **103**, 90–104 (2016).
16. Schiller, J. T., Day, P. M. & Kines, R. C. Current understanding of the mechanism of HPV infection. *Gynecologic Oncology* **118**, S12–S17 (2010).
17. Ljubojevic, S. & Skerlev, M. HPV-associated diseases. *Clinics in Dermatology* **32**, 227–234 (2014).
18. Balasubramaniam, R., Kuperstein, A. S. & Stoopler, E. T. Update on Oral Herpes Virus Infections. *Dental Clinics of North America* **58**, 265–280 (2014).
19. Kalantari-Dehaghi, M. *et al.* Discovery of Potential Diagnostic and Vaccine Antigens in Herpes Simplex Virus 1 and 2 by Proteome-Wide Antibody Profiling. *Journal of Virology* **86**, 4328–4339 (2012).
20. Wald, A. & Link, K. Risk of Human Immunodeficiency Virus Infection in Herpes Simplex Virus Type 2–Seropositive Persons: A Meta-analysis. *J Infect Dis* **185**, 45–52 (2002).
21. Whitesides, G. M. The origins and the future of microfluidics. *Nature* **442**, 368 (2006).
22. Ghosh, S., Kurup, G. K., Lee, A. P. & Ahn, C. A mass manufacturable thermoplastic based microfluidic droplet generator on Cyclic Olefin Copolymer (COC). *J. Micromech. Microeng.* (2019). doi:10.1088/1361-6439/ab0e60
23. Nyborg, W. L. Acoustic Streaming near a Boundary. *The Journal of the Acoustical Society of America* **30**, 329–339 (1958).
24. Strutt John William. I. On the circulation of air observed in Kundt's tubes, and on some allied acoustical problems. *Philosophical Transactions of the Royal Society of London* **175**, 1–21 (1884).
25. Kolb, J. & Nyborg, W. L. Small-Scale Acoustic Streaming in Liquids. *The Journal of the Acoustical Society of America* **28**, 1237–1242 (1956).
26. Elder, S. A. Cavitation Microstreaming. *The Journal of the Acoustical Society of America* **31**, 54–64 (1959).
27. Stuart, J. T. Double boundary layers in oscillatory viscous flow. *Journal of Fluid Mechanics* **24**, 673–687 (1966).
28. Riley, N. Oscillating viscous flows. *Mathematika* **12**, 161–175 (1965).
29. Riley, N. Acoustic streaming about a cylinder in orthogonal beams. *Journal of Fluid Mechanics* **242**, 387–394 (1992).

30. Marmottant, P. & Hilgenfeldt, S. Controlled vesicle deformation and lysis by single oscillating bubbles. *Nature* **423**, 153 (2003).
31. Lighthill, S. J. Acoustic streaming. *Journal of Sound and Vibration* **61**, 391–418 (1978).
32. Davidson, B. J. & Riley, N. Cavitation microstreaming. *Journal of Sound and Vibration* **15**, 217–233 (1971).
33. Wiklund, M., Green, R. & Ohlin, M. Acoustofluidics 14: Applications of acoustic streaming in microfluidic devices. *Lab Chip* **12**, 2438–2451 (2012).
34. Wang, C., Jalikop, S. V. & Hilgenfeldt, S. Size-sensitive sorting of microparticles through control of flow geometry. *Appl. Phys. Lett.* **99**, 034101 (2011).
35. Wang, C., Jalikop, S. V. & Hilgenfeldt, S. Efficient manipulation of microparticles in bubble streaming flows. *Biomicrofluidics* **6**, 012801 (2012).
36. Rallabandi, B., Wang, C. & Hilgenfeldt, S. Two-dimensional streaming flows driven by sessile semicylindrical microbubbles. *Journal of Fluid Mechanics* **739**, 57–71 (2014).
37. Rallabandi, B., Marin, A., Rossi, M., Kähler, C. J. & Hilgenfeldt, S. Three-dimensional streaming flow in confined geometries. *Journal of Fluid Mechanics* **777**, 408–429 (2015).
38. V. Patel, M., A. Nanayakkara, I., G. Simon, M. & P. Lee, A. Cavity-induced microstreaming for simultaneous on-chip pumping and size-based separation of cells and particles. *Lab on a Chip* **14**, 3860–3872 (2014).
39. Yu, Z. T. F., Yong, K. M. A. & Fu, J. Microfluidic Blood Cell Sorting: Now and Beyond. *Small* **10**, 1687–1703 (2014).
40. Toner, M. & Irimia, D. Blood-on-a-Chip. *Annual Review of Biomedical Engineering* **7**, 77–103 (2005).
41. Cui, F., Rhee, M., Singh, A. & Tripathi, A. Microfluidic Sample Preparation for Medical Diagnostics. *Annual Review of Biomedical Engineering* **17**, 267–286 (2015).
42. Bhagat, A. A. S. *et al.* Microfluidics for cell separation. *Med Biol Eng Comput* **48**, 999–1014 (2010).
43. Jin, C. *et al.* Technologies for label-free separation of circulating tumor cells: from historical foundations to recent developments. *Lab Chip* **14**, 32–44 (2013).
44. Che, J. *et al.* Classification of large circulating tumor cells isolated with ultra-high throughput microfluidic Vortex technology. *Oncotarget* **7**, 12748–12760 (2016).

45. Gupta, V. *et al.* ApoStream™, a new dielectrophoretic device for antibody independent isolation and recovery of viable cancer cells from blood. *Biomicrofluidics* **6**, (2012).
46. Lin, B. K., McFaul, S. M., Jin, C., Black, P. C. & Ma, H. Highly selective biomechanical separation of cancer cells from leukocytes using microfluidic ratchets and hydrodynamic concentrator. *Biomicrofluidics* **7**, (2013).
47. Li, P. *et al.* Acoustic separation of circulating tumor cells. *Proc Natl Acad Sci U S A* **112**, 4970–4975 (2015).
48. Yamada, M., Seko, W., Yanai, T., Ninomiya, K. & Seki, M. Slanted, asymmetric microfluidic lattices as size-selective sieves for continuous particle/cell sorting. *Lab Chip* **17**, 304–314 (2017).
49. Sollier, E. *et al.* Size-selective collection of circulating tumor cells using Vortex technology. *Lab Chip* **14**, 63–77 (2013).
50. Nivedita, N. & Papautsky, I. Continuous separation of blood cells in spiral microfluidic devices. *Biomicrofluidics* **7**, (2013).
51. Gao, J., Riahi, R., Sin, M. L. Y., Zhang, S. & Wong, P. K. Electrokinetic focusing and separation of mammalian cells in conductive biological fluids. *Analyst* **137**, 5215–5221 (2012).
52. Augustsson, P., Magnusson, C., Nordin, M., Lilja, H. & Laurell, T. Microfluidic, Label-Free Enrichment of Prostate Cancer Cells in Blood Based on Acoustophoresis. *Anal Chem* **84**, 7954–7962 (2012).
53. McFaul, S. M., Lin, B. K. & Ma, H. Cell separation based on size and deformability using microfluidic funnel ratchets. *Lab Chip* **12**, 2369–2376 (2012).
54. Filip Petersson, †, Lena Åberg, ‡, Ann-Margret Swärd-Nilsson, ‡ and & Thomas Laurell*, †. Free Flow Acoustophoresis: Microfluidic-Based Mode of Particle and Cell Separation. (2007). doi:10.1021/ac070444e
55. Kotz, K. T. *et al.* Clinical microfluidics for neutrophil genomics and proteomics. *Nature Medicine* **16**, 1042–1047 (2010).
56. Issadore, D. *et al.* Self-assembled magnetic filter for highly efficient immunomagnetic separation. *Lab Chip* **11**, 147–151 (2010).

57. Kim, M. S. *et al.* SSA-MOA: a novel CTC isolation platform using selective size amplification (SSA) and a multi-obstacle architecture (MOA) filter. *Lab Chip* **12**, 2874–2880 (2012).
58. Antfolk, M., Magnusson, C., Augustsson, P., Lilja, H. & Laurell, T. Acoustofluidic, Label-Free Separation and Simultaneous Concentration of Rare Tumor Cells from White Blood Cells. (2015). doi:10.1021/acs.analchem.5b02023
59. Ding, X. *et al.* Cell separation using tilted-angle standing surface acoustic waves. *PNAS* **111**, 12992–12997 (2014).
60. Davis, J. A. *et al.* Deterministic hydrodynamics: Taking blood apart. *PNAS* **103**, 14779–14784 (2006).
61. Nagrath, S. *et al.* Isolation of rare circulating tumour cells in cancer patients by microchip technology. *Nature* **450**, 1235–1239 (2007).
62. Stott, S. L. *et al.* Isolation of circulating tumor cells using a microvortex-generating herringbone-chip. *PNAS* **107**, 18392–18397 (2010).
63. Karabacak, N. M. *et al.* Microfluidic, marker-free isolation of circulating tumor cells from blood samples. *Nature Protocols* **9**, 694–710 (2014).
64. Huang, P.-H. *et al.* A reliable and programmable acoustofluidic pump powered by oscillating sharp-edge structures. *Lab Chip* **14**, 4319–4323 (2014).
65. Tovar, A. R. & Lee, A. P. Lateral cavity acoustic transducer. *Lab Chip* **9**, 41–43 (2009).
66. V. Patel, M., R. Tovar, A. & P. Lee, A. Lateral cavity acoustic transducer as an on-chip cell/particle microfluidic switch. *Lab on a Chip* **12**, 139–145 (2012).
67. Rogers, P. & Neild, A. Selective particle trapping using an oscillating microbubble. *Lab Chip* **11**, 3710–3715 (2011).
68. Burguillos, M. A. *et al.* Microchannel Acoustophoresis does not Impact Survival or Function of Microglia, Leukocytes or Tumor Cells. *PLOS ONE* **8**, e64233 (2013).
69. Hur, S. C., Mach, A. J. & Di Carlo, D. High-throughput size-based rare cell enrichment using microscale vortices. *Biomicrofluidics* **5**, (2011).
70. Chen, Y. *et al.* Rare cell isolation and analysis in microfluidics. *Lab Chip* **14**, 626–645 (2014).
71. Tong, X., Yang, L., Lang, J. C., Zborowski, M. & Chalmers, J. J. Application of immunomagnetic cell enrichment in combination with RT-PCR for the detection of rare

circulating head and neck tumor cells in human peripheral blood. *Cytometry Part B: Clinical Cytometry* **72B**, 310–323 (2007).

72. Dhar, M. *et al.* Label-free enumeration, collection and downstream cytological and cytogenetic analysis of circulating tumor cells. *Scientific Reports* **6**, 35474 (2016).
73. Nivedita, N., Garg, N., Lee, A. P. & Papautsky, I. A high throughput microfluidic platform for size-selective enrichment of cell populations in tissue and blood samples. *Analyst* **142**, 2558–2569 (2017).
74. Yu, M., Stott, S., Toner, M., Maheswaran, S. & Haber, D. A. Circulating tumor cells: approaches to isolation and characterization. *The Journal of Cell Biology* **192**, 373–382 (2011).
75. Liu, Z. *et al.* Rapid isolation of cancer cells using microfluidic deterministic lateral displacement structure. *Biomicrofluidics* **7**, (2013).
76. Carlo, D. D. Inertial microfluidics. *Lab Chip* **9**, 3038–3046 (2009).
77. Chen, Y. *et al.* High-throughput acoustic separation of platelets from whole blood. *Lab Chip* **16**, 3466–3472 (2016).
78. Marrinucci, D. *et al.* Case study of the morphologic variation of circulating tumor cells. *Human Pathology* **38**, 514–519 (2007).
79. Garg, N. *et al.* Whole-blood sorting, enrichment and *in situ* immunolabeling of cellular subsets using acoustic microstreaming. *Microsystems & Nanoengineering* **4**, 17085 (2018).
80. Haeberle, S. & Zengerle, R. Microfluidic platforms for lab-on-a-chip applications. *Lab Chip* **7**, 1094–1110 (2007).
81. Konry, T. *et al.* Particles and microfluidics merged: perspectives of highly sensitive diagnostic detection. *Microchim Acta* **176**, 251–269 (2012).
82. Sajeesh, P. & Sen, A. K. Particle separation and sorting in microfluidic devices: a review. *Microfluid Nanofluid* **17**, 1–52 (2014).
83. Boesch, M. *et al.* High prevalence of side population in human cancer cell lines. *Oncoscience* **3**, 85–87 (2016).
84. Challen, G. A. & Little, M. H. A Side Order of Stem Cells: The SP Phenotype. *STEM CELLS* **24**, 3–12 (2006).

85. Chiba, T. *et al.* Side population purified from hepatocellular carcinoma cells harbors cancer stem cell–like properties. *Hepatology* **44**, 240–251 (2006).
86. Boesch, M. *et al.* The side population of ovarian cancer cells defines a heterogeneous compartment exhibiting stem cell characteristics. *Oncotarget* **5**, 7027–7039 (2014).
87. Chambers, A. F., Groom, A. C. & MacDonald, I. C. Metastasis: Dissemination and growth of cancer cells in metastatic sites. *Nature Reviews Cancer* **2**, 563–572 (2002).
88. Moserle, L., Ghisi, M., Amadori, A. & Indraccolo, S. Side population and cancer stem cells: Therapeutic implications. *Cancer Letters* **288**, 1–9 (2010).
89. Gordon, S. & Taylor, P. R. Monocyte and macrophage heterogeneity. *Nature Reviews Immunology* **5**, 953–964 (2005).
90. Stansfield, B. K. & Ingram, D. A. Clinical significance of monocyte heterogeneity. *Clinical and Translational Medicine* **4**, 5 (2015).
91. Patil, P., Madhuprasad, Kumeria, T., Losic, D. & Kurkuri, M. Isolation of circulating tumour cells by physical means in a microfluidic device: a review. *RSC Adv.* **5**, 89745–89762 (2015).
92. Chen, Y. *et al.* Rare cell isolation and analysis in microfluidics. *Lab Chip* **14**, 626–645 (2014).
93. Stone, K. R., Mickey, D. D., Wunderli, H., Mickey, G. H. & Paulson, D. F. Isolation of a human prostate carcinoma cell line (DU 145). *International Journal of Cancer* **21**, 274–281 (1978).
94. Bokhoven, A. van *et al.* Molecular characterization of human prostate carcinoma cell lines. *The Prostate* **57**, 205–225 (2003).
95. Martel, J. M. & Toner, M. Inertial Focusing in Microfluidics. *Annu. Rev. Biomed. Eng.* **16**, 371–396 (2014).
96. Carlo, D. D., Irimia, D., Tompkins, R. G. & Toner, M. Continuous inertial focusing, ordering, and separation of particles in microchannels. *PNAS* **104**, 18892–18897 (2007).
97. Asmolov, E. S. The inertial lift on a spherical particle in a plane Poiseuille flow at large channel Reynolds number. *Journal of Fluid Mechanics* **381**, 63–87 (1999).

98. Bhagat, A. A. S., Kuntaegowdanahalli, S. S. & Papautsky, I. Enhanced particle filtration in straight microchannels using shear-modulated inertial migration. *Physics of Fluids* **20**, 101702 (2008).
99. Kuntaegowdanahalli, S. S., Bhagat, A. A. S., Kumar, G. & Papautsky, I. Inertial microfluidics for continuous particle separation in spiral microchannels. *Lab Chip* **9**, 2973–2980 (2009).
100. Warkiani, M. E. *et al.* An ultra-high-throughput spiral microfluidic biochip for the enrichment of circulating tumor cells. *Analyst* **139**, 3245–3255 (2014).
101. Guan, G. *et al.* Spiral microchannel with rectangular and trapezoidal cross-sections for size based particle separation. *Scientific Reports* **3**, 1475 (2013).
102. Qi, W. *et al.* Sorting and identification of side population cells in the human cervical cancer cell line HeLa. *Cancer Cell International* **14**, 3 (2014).
103. Xavier, M., Oreffo, R. O. C. & Morgan, H. Skeletal stem cell isolation: A review on the state-of-the-art microfluidic label-free sorting techniques. *Biotechnology Advances* **34**, 908–923 (2016).
104. Wang, S. Y., Mak, K. L., Chen, L. Y., Chou, M. P. & Ho, C. K. Heterogeneity of human blood monocyte: two subpopulations with different sizes, phenotypes and functions. *Immunology* **77**, 298–303 (1992).
105. Passlick, B., Flieger, D. & Ziegler-Heitbrock, H. W. Identification and characterization of a novel monocyte subpopulation in human peripheral blood. *Blood* **74**, 2527–2534 (1989).
106. Strauss-Ayali, D., Conrad, S. M. & Mosser, D. M. Monocyte subpopulations and their differentiation patterns during infection. *Journal of Leukocyte Biology* **82**, 244–252 (2007).
107. Wiklund, M. Acoustofluidics 12: Biocompatibility and cell viability in microfluidic acoustic resonators. *Lab Chip* **12**, 2018–2028 (2012).
108. UNAIDS DATA 2017. Available at: http://www.unaids.org/en/resources/documents/2017/2017_data_book. (Accessed: 2nd February 2018)

109. WHO | Herpes simplex virus. *WHO* Available at: http://www.who.int/mediacentre/factsheets/fs400/en/. (Accessed: 2nd February 2018)
110. WHO | 24 October 2014, vol. 89, 43 (pp. 465–492). *WHO* Available at: http://www.who.int/wer/2014/wer8943/en/. (Accessed: 2nd February 2018)
111. Ahdieh, L. *et al.* Prevalence, Incidence, and Type-Specific Persistence of Human Papillomavirus in Human Immunodeficiency Virus (HIV)-Positive and HIV-Negative Women. *J Infect Dis* **184**, 682–690 (2001).
112. Hysterectomy Among Women With HIV: Indications and Incidence. Available at: http://www.natap.org/2007/HIV/052207_11.htm. (Accessed: 5th April 2018)
113. Cornett, J. K. & Kirn, T. J. Laboratory Diagnosis of HIV in Adults: A Review of Current Methods. *Clin Infect Dis* **57**, 712–718 (2013).
114. Singh, A., Preiksaitis, J., Ferenczy, A. & Romanowski, B. The laboratory diagnosis of herpes simplex virus infections. *Can J Infect Dis Med Microbiol* **16**, 92–98 (2005).
115. Devegowda, D., Doddamani, P. & Vishwanath, P. Human papillomavirus screening: Time to add molecular methods with cytology. *International Journal of Health & Allied Sciences* **3**, 145 (2014).
116. Inan, H. *et al.* Isolation, Detection, and Quantification of Cancer Biomarkers in HPV-Associated Malignancies. *Scientific Reports* **7**, 3322 (2017).
117. Costantini, F. *et al.* Lab-on-chip system combining a microfluidic-ELISA with an array of amorphous silicon photosensors for the detection of celiac disease epitopes. *Sensing and Bio-Sensing Research* **6**, 51–58 (2015).
118. Shafiee, H. *et al.* Emerging Technologies for Point-of-Care Management of HIV Infection. *Annual Review of Medicine* **66**, 387–405 (2015).
119. Zhang, W., Guo, S., Carvalho, W. S. P., Jiang, Y. & Serpe, M. J. Portable point-of-care diagnostic devices. *Anal. Methods* **8**, 7847–7867 (2016).
120. Yeh, E.-C. *et al.* Self-powered integrated microfluidic point-of-care low-cost enabling (SIMPLE) chip. *Science Advances* **3**, e1501645 (2017).
121. Branavan, M. *et al.* Modular development of a prototype point of care molecular diagnostic platform for sexually transmitted infections. *Medical Engineering and Physics* **38**, 741–748 (2016).

122. Workman, S. *et al.* Rapid detection of HIV-1 p24 antigen using magnetic immuno-chromatography (MICT). *Journal of Virological Methods* **160**, 14–21 (2009).
123. Grant, B. D., Smith, C. A., Castle, P. E., Scheurer, M. E. & Richards-Kortum, R. A paper-based immunoassay to determine HPV vaccination status at the point-of-care. *Vaccine* **34**, 5656–5663 (2016).
124. Chin, C. D., Linder, V. & Sia, S. K. Commercialization of microfluidic point-of-care diagnostic devices. *Lab Chip* **12**, 2118–2134 (2012).
125. Kim, Y.-G., Moon, S., Kuritzkes, D. R. & Demirci, U. Quantum dot-based HIV capture and imaging in a microfluidic channel. *Biosens Bioelectron* **25**, 253–258 (2009).
126. Shafiee, H. *et al.* Acute On-Chip HIV Detection Through Label-Free Electrical Sensing of Viral Nano-Lysate. *Small* **9**, 2553–2563 (2013).
127. Inci, F. *et al.* Nanoplasmonic Quantitative Detection of Intact Viruses from Unprocessed Whole Blood. *ACS Nano* **7**, 4733–4745 (2013).
128. García-Sierra, N. *et al.* Evaluation of an Array-Based Method for Human Papillomavirus Detection and Genotyping in Comparison with Conventional Methods Used in Cervical Cancer Screening. *J Clin Microbiol* **47**, 2165–2169 (2009).
129. Alonso, R., Roa, P. L., Suárez, M. & Bouza, E. New Automated Chemiluminescence Immunoassay for Simultaneous but Separate Detection of Human Immunodeficiency Virus Antigens and Antibodies. *J. Clin. Microbiol.* **52**, 1467–1470 (2014).
130. Vaculovicova, M., Michalek, P., Krizkova, S., Macka, M. & Adam, V. Nanotechnology-based analytical approaches for detection of viruses. *Analytical Methods* **9**, 2375–2391 (2017).
131. de la Rica, R. & Stevens, M. M. Plasmonic ELISA for the ultrasensitive detection of disease biomarkers with the naked eye. *Nature Nanotechnology* **7**, 821–824 (2012).
132. Ng, A. H. C., Uddayasankar, U. & Wheeler, A. R. Immunoassays in microfluidic systems. *Anal Bioanal Chem* **397**, 991–1007 (2010).
133. Chin, C. D. *et al.* Microfluidics-based diagnostics of infectious diseases in the developing world. *Nature Medicine* **17**, 1015–1019 (2011).
134. Guo, T., Patnaik, R., Kuhlmann, K., Rai, A. J. & Sia, S. K. Smartphone dongle for simultaneous measurement of hemoglobin concentration and detection of HIV antibodies. *Lab Chip* **15**, 3514–3520 (2015).

135. Laksanasopin, T. *et al.* A smartphone dongle for diagnosis of infectious diseases at the point of care. *Science Translational Medicine* **7**, 273re1-273re1 (2015).
136. Luevano, M. *et al.* High-throughput profiling of the humoral immune responses against thirteen human papillomavirus types by proteome microarrays. *Virology* **405**, 31–40 (2010).
137. Dasgupta, G. *et al.* Immunodominant "Asymptomatic" Herpes Simplex Virus 1 and 2 Protein Antigens Identified by Probing Whole-ORFome Microarrays with Serum Antibodies from Seropositive Asymptomatic versus Symptomatic Individuals. *J Virol* **86**, 4358–4369 (2012).
138. Okabe, Y., Chen, Y., Purohit, R., Corn, R. M. & Lee, A. P. Piezoelectrically driven vertical cavity acoustic transducers for the convective transport and rapid detection of DNA and protein binding to DNA microarrays with SPR imaging—A parametric study. *Biosensors and Bioelectronics* **35**, 37–43 (2012).
139. Liao, U., Tovar, A., Felgner, P. & Lee, A. P. A Microfluidic Approach and Enhancement Towards a Colorimetric Enzyme-Linked-Immunosorbant-Assay for Diagnostic Detection of Infectious Diseases. 71–72 (2007). doi:10.1115/BioMed2007-38105
140. Garg, N. *et al.* Integrated On-Chip Microfluidic Immunoassay for Rapid Biomarker Detection. *Procedia Engineering* **159**, 53–57 (2016).
141. Mok, J., Mindrinos, M. N., Davis, R. W. & Javanmard, M. Digital microfluidic assay for protein detection. *PNAS* **111**, 2110–2115 (2014).
142. Pant Pai, N. & Daher, J. Multiplexed testing for HIV and related bacterial and viral co-infections at the point-of-care: quo vadis? *Expert Rev. Mol. Diagn.* **15**, 463–469 (2015).
143. Wylie, K. M. *et al.* Detection of Viruses in Clinical Samples Using Metagenomic Sequencing and Targeted Sequence Capture. *Journal of Clinical Microbiology* **56**, JCM.01123-18 (2018).
144. Di Bonito, P. *et al.* Detection of oncogenic viruses in water environments by a Luminex-based multiplex platform for high throughput screening of infectious agents. *Water Research* **123**, 549–555 (2017).
145. Cao, B. *et al.* DNA Microarray Characterization of Pathogens Associated with Sexually Transmitted Diseases. *PLOS ONE* **10**, e0133927 (2015).

146. Sexually Transmitted Viral Infections in Women: HIV, HSV, and HPV | Patient Care. Available at: http://www.patientcareonline.com/infections-medicine-journal/sexually-transmitted-viral-infections-women-hiv-hsv-and-hpv. (Accessed: 2nd February 2018)
147. Methods And Compositions of Protein Antigens For The Diagnosis And Treatment of Herpes Simplex Viruses Type 1 And 2. (2016).
148. Malamud, D. & Rodriguez-Chavez, I. R. Saliva as a Diagnostic Fluid. *Dent Clin North Am* **55**, 159–178 (2011).
149. Garg, N. *et al.* Rapid immunodiagnostics of multiple viral infections in an acoustic microstreaming device with serum and saliva samples. *Lab Chip* (2019). doi:10.1039/C8LC01303A
150. St John, A. & Price, C. P. Existing and Emerging Technologies for Point-of-Care Testing. *Clin Biochem Rev* **35**, 155–167 (2014).
151. Hou, H. W. *et al.* Microfluidic Devices for Blood Fractionation. *Micromachines* **2**, 319–343 (2011).
152. Wong, A. P., Gupta, M., Shevkoplyas, S. S. & Whitesides, G. M. Egg beater as centrifuge: isolating human blood plasma from whole blood in resource-poor settings. *Lab Chip* **8**, 2032–2037 (2008).
153. Gong, M. M., MacDonald, B. D., Vu Nguyen, T., Van Nguyen, K. & Sinton, D. Field tested milliliter-scale blood filtration device for point-of-care applications. *Biomicrofluidics* **7**, (2013).
154. Liu, C. *et al.* Membrane-Based, Sedimentation-Assisted Plasma Separator for Point-of-Care Applications. *Anal. Chem.* **85**, 10463–10470 (2013).
155. Crowley, T. A. & Pizziconi, V. Isolation of plasma from whole blood using planar microfilters for lab-on-a-chip applications. *Lab Chip* **5**, 922–929 (2005).
156. Son, J. H. *et al.* Hemolysis-free blood plasma separation. *Lab Chip* **14**, 2287–2292 (2014).
157. Zhang, X.-B. *et al.* Gravitational Sedimentation Induced Blood Delamination for Continuous Plasma Separation on a Microfluidics Chip. *Anal. Chem.* **84**, 3780–3786 (2012).
158. Yang, S., Ündar, A. & Zahn, J. D. A microfluidic device for continuous, real time blood plasma separation. *Lab Chip* **6**, 871–880 (2006).

159. Xia, Y. & Whitesides, G. M. Soft Lithography. *Annual Review of Materials Science* **28**, 153–184 (1998).
160. Mark, D., Haeberle, S., Roth, G., Stetten, F. von & Zengerle, R. Microfluidic lab-on-a-chip platforms: requirements, characteristics and applications. *Chem. Soc. Rev.* **39**, 1153–1182 (2010).
161. Fredrik Carlborg, C., Haraldsson, T., Öberg, K., Malkoch, M. & Wijngaart, W. van der. Beyond PDMS: off-stoichiometry thiol –ene (OSTE) based soft lithography for rapid prototyping of microfluidic devices. *Lab on a Chip* **11**, 3136–3147 (2011).
162. Hoyle, C. E. & Bowman, C. N. Thiol–Ene Click Chemistry. *Angewandte Chemie International Edition* **49**, 1540–1573 (2010).

Appendix

Cover Image 1

Volume 142 | Number 14 | 21 July 2017 | Pages 2509–2680

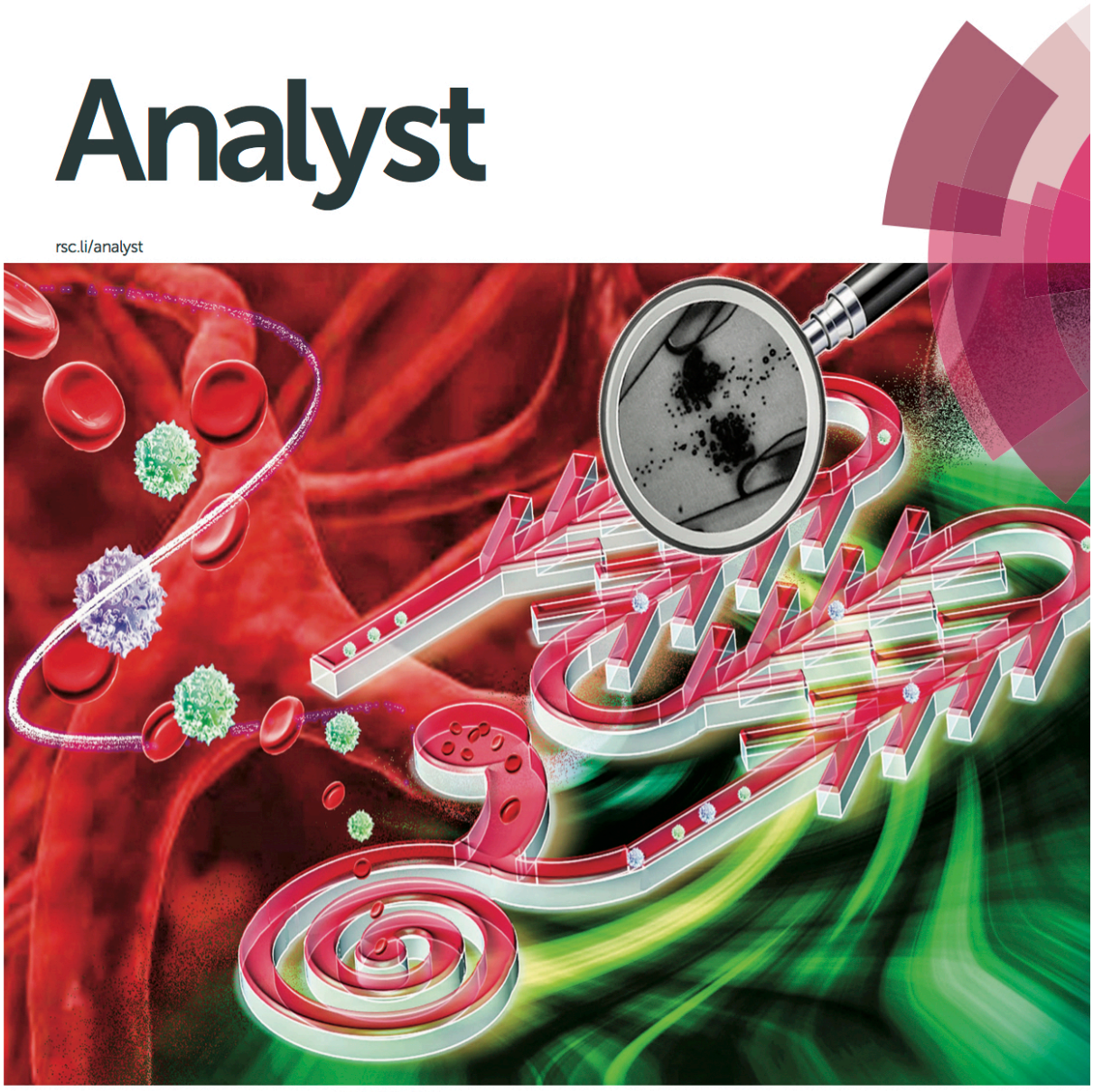

ISSN 0003-2654

ROYAL SOCIETY OF CHEMISTRY

PAPER
Ian Papautsky, Abe Lee *et al.*
A high throughput microfluidic platform for size-selective enrichment of cell populations in tissue and blood samples

Cover Image 2

Volume 19 | Number 9 | 7 May 2019 | Pages 1515–1696

Lab on a Chip

Devices and applications at the micro- and nanoscale

rsc.li/loc

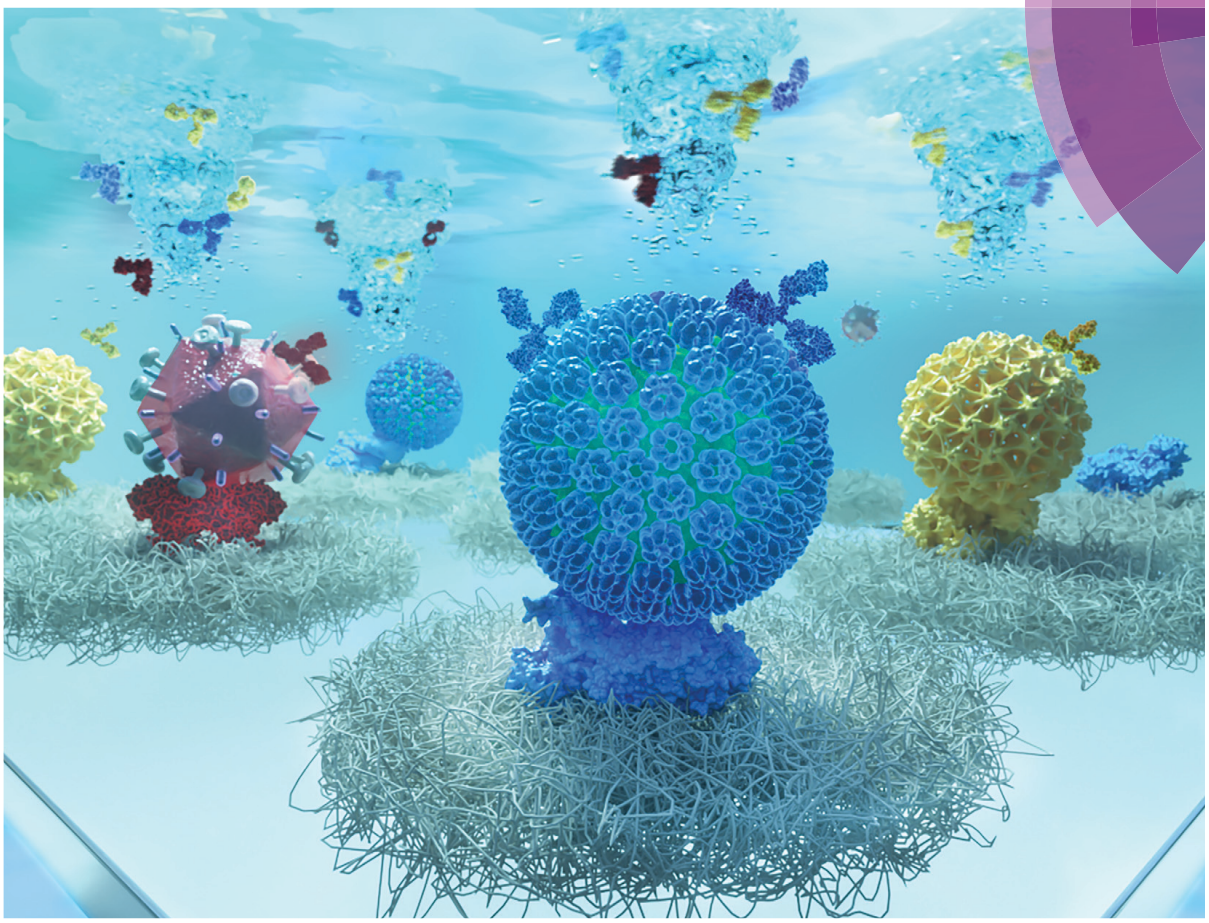

ISSN 1473-0197

ROYAL SOCIETY OF CHEMISTRY | Celebrating IYPT 2019

PAPER
Abraham P. Lee *et al.*
Rapid immunodiagnostics of multiple viral infections in an acoustic microstreaming device with serum and saliva samples